A Diffeomorphic 3D-to-3D Registration Algorithm for the Segmentation of the Left Ventricle in Ultrasound Sequences

by

Deepa Krishnaswamy

A thesis submitted in partial fulfillment of the requirements for the degree of

Doctor of Philosophy

Medical Sciences - Radiology and Diagnostic Imaging
University of Alberta

Abstract

Heart disease is the second leading cause of death in Canada, where it affects the lives of over two million people. One modality used to detect and diagnose heart disease and other abnormalities is echocardiography or ultrasound imaging of the heart. Ultrasound imaging, compared to other modalities has several advantages; it is non-ionizing, portable, and cost-effective, and provides good spatial and temporal resolution. It is crucial that the left ventricle must be analyzed in the case of cardiac diseases. Metrics derived from analysis of the left ventricle provide an indication to the clinician about the performance of the heart. However, the current clinical software and methods available in the literature to analyze the left ventricle suffer from several potential drawbacks. Geometrical assumptions may be made about the chamber, or a large amount of manual interaction is required. In the case of supervised deep learning neural networks, a training dataset may be required, which may be difficult to obtain.

Therefore the goal of this thesis was to focus on the development of semi-automated methods to delineate the endocardium of the left ventricle based on registration. The methods developed do not require the use of training data, geometrical assumptions, or prior knowledge about the image characteristics. The thesis focuses mainly on the application to ultrasound sequences, with additional testing on MR sequences. In particular, a semi-automated method has been developed with the use of a diffeomorphic registration algorithm to delineate the endocardial borders at end-diastole and end-systole. This method was expanded to provide a segmentation over the full temporal sequence of ultrasound images. Lastly, a 3D-to-3D diffeomorphic registration

method was developed for segmentation, where the algorithm was able to capture the full dynamics of the motion of the left ventricle over the cardiac cycle.

We have compared the proposed methods to other common registration packages in terms of standard distance and clinical metrics. The results demonstrate the benefit of using a diffeomorphic registration method for the segmentation of the left ventricle.

Preface

This thesis was submitted as partial fulfillment of the degree Doctor of Philosophy (Ph.D.) in Radiology and Diagnostic Imaging at the University of Alberta. The thesis is an original work by Deepa Krishnaswamy and the presented work was accomplished between September 2016 and August 2021. The research project, of which this thesis is a part, received research ethics approval from the University of Alberta Research Ethics Board.

Material for this thesis is based on the following papers:

Chapter 3:

Krishnaswamy D, Hareendranathan AR, Suwatanaviroj T, Becher H, Noga M, Punithakumar K. A semi-automated method for measurement of left ventricular volumes in 3D echocardiography. IEEE Access. 2018 Mar 15;6:16336-44.

Chapter 4:

Krishnaswamy D, Hareendranathan AR, Suwatanaviroj T, Boulanger P, Becher H, Noga M, Punithakumar K. A New Semi-automated Algorithm for Volumetric Segmentation of the Left Ventricle in Temporal 3D Echocardiography Sequences. Cardiovascular Engineering and Technology. 2021 May 27:1-14.

Krishnaswamy D, Hareendranathan AR, Suwatanaviroj T, Boulanger P, Becher H, Noga M, Punithakumar K. A novel 4D semi-automated algorithm for volumetric segmentation in echocardiography. In 2018 40th Annual International Conference of the IEEE Engineering in Medicine and Biology Society (EMBC) 2018 Jul 18 (pp. 1119-1122). IEEE.

Deepa Krishnaswamy was responsible for the development of the algorithms, the

validation of the approaches, and the writing of the manuscripts. Dr. Hareendranathan, Dr. Noga and Dr. Punithakumar were responsible for assisting in the formulation of the algorithms and editing of the manuscripts. Dr. Suwatanaviroj and Dr. Becher were responsible for providing the data and the associated ground truth reference. Additional papers will be submitted related to Chapter 5, which involves the development of a 3D-to-3D diffeomorphic registration algorithm.

Acknowledgements

I would like to thank my supervisors Dr. Kumaradevan Punithakumar and Dr. Michelle Noga for giving me the opportunity to pursue a Ph.D. in the Servier lab. From the first day, I felt extremely welcome working in their lab. They have provided me with so much technical and clinical guidance over the years and were always readily available for meetings and discussions. It has been very enjoyable working in their lab over these past few years. The Servier lab would not be the same without its many members, and I would like to acknowledge my former and present colleagues that have made my Ph.D. experience pleasant. To Andrew, Jiali, Haki, Atefeh, Fatemeh, Ahmed, Dat, Bernal, and Sharanya, it was wonderful working with and getting to know each of them. I would like to especially thank Abhilash and Ameneh who have provided me with so much guidance over the years and many interesting non-lab-related discussions. I will miss the lab lunches all of us shared together and the many Tim Hortons coffee breaks. I would also like to thank Dr. Harald Becher and Dr. Tan Suwatanaviroj from the Mazankowski Alberta Heart Institute, who have graciously provided me with echocardiography data and the ground truth segmentations. My work would not be possible without their contributions. Dr. Pierre Boulanger was also very helpful in providing me with feedback and new research ideas.

There are so many friends that made me feel like I was part of their family, from long nights of Settler's of Catan and eating their home-cooked food with Atreya, Pai, and Naresh, to making music with Dhanvini and exploring Edmonton with Anjana and Shruthi, I couldn't have asked for better friends to be surrounded by. The Carrot Community Arts Coffeehouse was integral in keeping me well-caffeinated, and it was

a joy working as a barista with Chris, Elsa and Andrew, and creating music with the many local musicians during the open-mic nights. I would also like to thank my former and current roommates: Shahnaz and Navid, it was wonderful living with them and experiencing a bit of Persian culture. To Martin (and Bella), who made me feel like part of their family. To Serge, who put up with me during these last crucial months and provided me with entertainment and Lebanese food during the pandemic. Lastly, I'd like to thank my parents and my sister for their constant support, who at first didn't know where Edmonton was, but now hopefully they do.

Table of Contents

1 Introduction **1**

1.1 Clinical overview and motivation 1

1.1.1 Heart anatomy and function 1

1.1.2 Ultrasound imaging 3

1.1.3 Evaluating cardiac function using ultrasound imaging 5

1.2 Thesis contributions 11

1.3 Thesis overview 12

2 Background **14**

2.1 Image registration overview and methods in literature 14

2.1.1 Basics of image registration 14

2.1.2 Cardiac ultrasound image registration in literature 16

2.2 3D segmentation methods in literature 19

2.2.1 Traditional methods 19

2.2.2 Atlas based segmentation methods 24

2.2.3 Deep learning-based segmentation methods 25

2.3 3D+t segmentation methods in literature 26

2.3.1 Traditional methods for image sequence segmentation 26

2.3.2 Machine learning methods 30

3 3D Spatial Segmentation in US Volumes **31**

3.1 Overview 31

3.2 Algorithm . . . 33
3.2.1 Creation of angular slices . . . 33
3.2.2 Creation of initial manual contours . . . 35
3.2.3 Automatic contour generation with diffeomorphic image registration . . . 36
3.2.4 Mesh generation . . . 37
3.3 Results . . . 38
3.3.1 Dataset - CETUS . . . 38
3.3.2 Quantitative distance metrics . . . 41
3.3.3 Quantitative distance metrics results . . . 42
3.3.4 Quantitative clinical metrics results . . . 45
3.4 Conclusion . . . 46

4 3D Temporal Segmentation in US Sequences 52

4.1 Overview . . . 52
4.2 Dataset . . . 54
4.3 Algorithm . . . 54
4.3.1 Temporal implementation of 3D segmentation . . . 54
4.4 Results for 3D spatial segmentation . . . 55
4.4.1 Quantitative distance metrics for ED and ES . . . 55
4.4.2 Quantitative clinical metrics for ED and ES . . . 55
4.5 Additional experiments . . . 56
4.5.1 Varying angular spacing for 3D spatial segmentation . . . 58
4.5.2 Effect of initial axis for 3D segmentation . . . 61
4.5.3 Effect of initial contours . . . 61
4.5.4 Comparison to a geometrical model . . . 67
4.6 Results for 3D+t temporal segmentation . . . 70

4.6.1 Quantitative performance evaluation against other registration methods . . . 70
4.6.2 Visual inspection . . . 71
4.7 Conclusion . . . 72

5 3D-to-3D Diffeomorphic Registration Algorithm 77
5.1 Overview . . . 77
5.2 Algorithm . . . 78
5.2.1 Theoretical overview . . . 78
5.2.2 Numerical implementation . . . 81
5.3 Results . . . 85
5.3.1 Registration software packages . . . 87
5.3.2 Datasets used . . . 88
5.3.3 Metrics . . . 90
5.3.4 MRI results . . . 91
5.3.5 Ultrasound results . . . 98
5.4 Additional experiments . . . 104
5.4.1 Diffeomorphic constraints experiment . . . 104
5.5 Conclusion . . . 106

6 Conclusions & Future Work 108
6.1 Overview . . . 108
6.1.1 Accomplishments . . . 109
6.2 Limitations and future work . . . 110
6.2.1 Manual interaction . . . 110
6.2.2 Clinical measures . . . 111
6.2.3 Creation of the ground truth . . . 112
6.2.4 Comparison to other registration methods . . . 113
6.2.5 Improvements to the 3D-to-3D registration algorithm . . . 113

Bibliography **115**

List of Tables

3.1 Distance and overlap metrics for end-diastole: The mean absolute distance d_m, Hausdorff distance d_H and modified Dice score D^* values for quantitative evaluation of the accuracy of segmentation results by semi and fully automated methods in comparison to the ground truth segmentation by experts. The lower the value of d_m, d_H or D^* the better the performance of the approach. Inter-observer values indicate differences within the ground truth segmentation by three different experts. Standard deviation values are provided in parentheses. 43

3.2 Distance and overlap metrics for end-systole: The mean absolute distance d_m, Hausdorff distance d_H and modified Dice score D^* values for quantitative evaluation of the accuracy of segmentation results by semi and fully automated methods in comparison to the ground truth segmentation by experts. The lower the value of d_m, d_H or D^* the better the performance of the approach. Inter-observer values indicate differences within the ground truth segmentation by three different experts. Standard deviation values are provided in parentheses. 44

3.3 Clinical metrics: Agreements between EDV values computed using automated methods and ground truth segmentation by experts. The inter-observer variability values indicate the reproducibility of EDV calculated using manual segmentation. 47

3.4 Clinical metrics: Agreements between ESV values computed using automated methods and ground truth segmentation by experts. The inter-observer variability values indicate the reproducibility of ESV calculated using manual segmentation. 48

3.5 Clinical metrics: Agreements between ejection fraction values computed using automated methods and ground truth segmentation in terms of correlation and Bland-Altman analysis. The inter-observer variability values indicate the reproducibility of ejection fraction calculated using manual segmentation. 49

4.1 Quantitative evaluation results for end diastole and end systole: The mean absolute distance d_m in mm, Hausdorff distance d_H in mm, and the Dice score *Dice* for evaluation of the proposed method and the ground truth segmentation for all subjects. Standard deviation values are provided in parentheses. 56

4.2 Clinical metrics for end diastole, end systole and ejection fraction: The mean difference between the proposed method and ground truth segmentations. Standard deviation values are provided in parentheses. . 56

4.3 Varying angular spacing: Comparing the end diastolic and end systolic segmentations from the proposed method to the ground truth for angular spacing values of 1, 5, 10, and 15 degrees. The following three distance and overlap metrics are used: mean absolute distance (d_m), Hausdorff distance (d_H) and the Dice score (*Dice*). 59

4.4 Kruskal-Wallis H significance tests were formed for the end diastolic and end systolic volumes for the following three distance and overlap metrics: mean absolute distance (d_m, Hausdorff distance (d_H) and the Dice score (*Dice*). 59

4.5 Effect of initial axis: Comparing the end diastolic and end systolic segmentations from the proposed method to the ground truth for x-, x+, y-, y+, z-, and z+ rotations. The following three distance and overlap metrics are used: mean absolute distance (d_m), Hausdorff distance (d_H) and the Dice score ($Dice$), along with the volume in mL. 62

4.6 Kruskal-Wallis H significance tests were performed for the axis delineation test using the following four metrics: mean absolute distance (d_m), Hausdorff distance (d_H) and the Dice score ($Dice$), and the volume in mL. 62

4.7 Effect of initial contour: Comparing the end diastolic and end systolic segmentations from the proposed method to the ground truth for dilation and erosion of the initial contour. The following three distance and overlap metrics are used: mean absolute distance (d_m), Hausdorff distance (d_H) and the Dice score ($Dice$) along with the volume in mL. 64

4.8 Kruskal-Wallis H significance tests were performed for the initial contours tests. Four metrics were used for the comparison, the mean absolute distance (d_m), Hausdorff distance (d_H) and the Dice score ($Dice$), as well as the computation of the volume in mL. 64

4.9 Effect of fitting an ellipsoid: Comparing the end diastolic and end systolic segmentations from the proposed method to the ground truth for angular spacing values of 1, 5, 10, and 15 degrees. The following three distance and overlap metrics are used: mean absolute distance (d_m), Hausdorff distance (d_H) and the Dice score ($Dice$). 68

4.10 To determine if there were significant differences between the ellipsoid model and the ground truth, Kruskal-Wallis H significance tests were performed for the following metrics: mean absolute distance (d_m, Hausdorff distance (d_H) and the Dice score ($Dice$), as well as the computation of the *volume* 68

4.11 The proposed 3D+t segmentation method was compared to four publicly available registration methods in terms of the following distance, overlap and clinical metrics: the mean absolute distance d_m in mm, Hausdorff distance d_H in mm, the Dice score $Dice$, and the correlation coefficient of the volumes in mL compared to the ground truth. The average time required for the registration between a pair of frames is also provided. The metrics reported are averaged over all subjects over the full cardiac cycle. The standard deviation values are provided in parentheses. 72

5.1 Quantitative evaluation results for the MRI dataset: The proposed algorithm was compared to the ground truth and six other registration algorithms, symmetric normalization from the Dipy package, two versions of the Demons algorithm (classical and fast symmetric forces) from ITK, RealTiTracker (L_2L_1 and L_2L_2) and Elastix. The following metrics are reported for each method: mean absolute distance d_m in mm, Hausdorff distance d_H in mm, Dice score $Dice$, and the percentage of voxels of the Jacobian determinant that are less than zero $J_{<0}\%$. Results are evaluated over 20 subjects using MRI temporal sequences from the ACDC dataset. Smaller values of d_m, d_H and larger values of $Dice$ indicate more accurate segmentation results. As the determinant of Jacobian value less than zero indicates mesh folding, a number greater than zero for $J_{<0}\%$ indicates mesh folding occurred. In order to determine if a significant difference exists for the d_m, d_H and the $Dice$ metrics among the set of registration methods, Kruskal-Wallis H significance tests were performed. The average time to perform for a single 3D-3D frame is provided in seconds. The standard deviation values for all of the metrics are given in parentheses. Values that are highlighted in bold indicate the metric that gave the highest performance compared to the other algorithms. 93

5.2 Bland Altman bias and limits of agreement (LOA) values for each of the registration methods compared to the ground truth volumes. . . . 94

5.3 Quantitative evaluation results for the US dataset: The proposed algorithm was compared to the ground truth and six other registration algorithms, symmetric normalization from the Dipy package, two versions of the Demons algorithm (classical and fast symmetric forces) from ITK, RealTiTracker (L_2L_1 and L_2L_2) and Elastix. The following metrics are reported for each method: mean absolute distance d_m in mm, Hausdorff distance d_H in mm, Dice score $Dice$, and the percentage of voxels of the Jacobian determinant that are less than zero $J_{<0}\%$. Results are evaluated over 10 subjects using US temporal sequences from the Mazankowski Alberta Heart Institute. Smaller values of d_m, d_H and larger values of $Dice$ indicate more accurate segmentation results. As a determinant of Jacobian value less than zero indicates mesh folding, a number greater than zero for $J_{<0}\%$ indicates mesh folding occurred. In order to determine if a significant difference exists for the d_m, d_H and the $Dice$ metrics among the set of registration methods, Kruskal-Wallis H significance tests were performed. The average time to perform for a single 3D-3D frame is provided in seconds. The standard deviation values for all of the metrics are given in parentheses. Values that are highlighted in bold indicate the metric that gave the highest performance compared to the other algorithms. 99

5.4 Bland Altman bias and limits of agreement (LOA) values for each of the registration methods compared to the ground truth volumes. . . . 99

5.5 Diffeomorphic constraint experiment results: The diffeomorphic constraints were removed in order to understand the effect on the determinant of the Jacobian metric. The percentage of voxels with a determinant of the Jacobian less than zero is given by $J_{<0}\%$, indicating mesh folding. The mean absolute difference d_m in mm, Hausdorff distance d_H in mm, Dice score $Dice$ are also provided for comparison. 104

List of Figures

1.1 Basic anatomy of the heart [2]. 2

1.2 An example of an ECG wave [4]. 3

1.3 An example of foreshortening in the 4-chamber view that can occur with use of a 2DUS probe [7]. The blue plane is capturing the true apex, while the yellow plane is foreshortened. 4

1.4 An example of a volume curve from the TomTec clinical software, obtained using 3D speckle tracking over the cardiac cycle [15]. 7

1.5 Automated delineation of the LV with ellipsoidal discs generated between the apex and base. These discs are summed to obtain the volume of the chamber [15]. 8

1.6 The ellipsoid discs created between the apex and the base of the LV [15]. 8

1.7 The process for semi-automated delineation of the LV endocardium across the cardiac cycle using the TomTec Arena software [15]. 9

1.8 Dynamic HeartModel developed by Philips [16]. 10

1.9 Clinical workflow using Dynamic HeartModel from Philips [16]. . . . 11

3.1 Flowchart of the proposed approach for the 3D semi-automated segmentation of the left ventricle at end-diastole and end-systole. 32

3.2 User-defined axis for the left ventricle at end-diastole. 33

3.3 A demonstration of the two initial contours delineated on orthogonal planes by an expert clinician at the (a) θ_0 and (b) θ_{90} angular slices . 35

3.4 Flowchart of the 2D registration process. 37

3.5 An example of a subset of the angular slices sequence every 15 degrees 38
3.6 Delineation of the endocardium of the left ventricle at end-diastole using the proposed methodology. 39
3.7 A representation of the formation of the dense mesh, where i, $i+1$, $i+2$ represent three contours. 39
3.8 Example mean absolute distance d_m meshes for a single patient at (a) end diastole and (b) end systole. Red represents the larger distance from the ground truth, and blue represents a small distance in mm. . 45
3.9 Bland-Altman plots comparing the proposed method to the reference segmentations for (A) End-diastolic volume (B) End-systolic volume (C) Ejection fraction 51

4.1 Flowchart of the 3D+time segmentation process. 53
4.2 Bland-Altman plots for the (a) EDV (b) ESV and (c) EF. The zero reference line is displayed in black, while the bias line is shown in red. The two blue lines indicate the limits of agreement at two standard deviations away from the mean. 57
4.3 Boxplots displaying the results of varying the angular spacing for 3D spatial segmentation at (a) end diastole and (b) end systole for 1, 5, 10 and 15 degrees, for the following distance and overlap metrics: d_m, d_H and $Dice$. 60
4.4 Boxplots displaying the rotations in x-, x+, y-, y+, z-, and z+ directions for the following metrics: mean absolute distance (d_m, Hausdorff distance (d_H) and the Dice score ($Dice$), along with the volume in mL for (a) End diastole and (b) End systole 63

4.5 Boxplots displaying the operations dilate and erode for the following metrics: mean absolute distance (d_m, Hausdorff distance (d_H) and the Dice score ($Dice$), along with the volume in mL for (a) End diastole and (b) End systole 65

4.6 Figures displaying the an example of the original contour in green, dilated contour in red and eroded contour in yellow for four cases: (a) End diastole θ_0 (b) End diastole θ_{90} (c) End systole θ_0 (d) End systole θ_{90} 66

4.7 Boxplots displaying the fit ellipsoid results for the following metrics: mean absolute distance (d_m, Hausdorff distance (d_H) and the Dice score ($Dice$), along with the volume in mL for (a) End diastole and (b) End systole 69

4.8 Example of fitting a truncated ellipsoid to the 0 degree and 90 degree contours. 70

4.9 Comparison of the ground truth mesh in gray and the proposed method by use of the d_m metric for four cases: (a) end diastole (b) end systole (c) in the systolic phase (d) in the diastolic phase. The color bars indicate the distance from the ground truth in mm, where blue indicates a small difference and red indicates a larger difference. 73

4.10 Volume curve representation of two example patients. The green line represents the ground truth obtained from the clinical software TomTec Arena and the red line represents the volumes obtained from the proposed method. The volume is provided in mL. Results demonstrate high agreement with the ground truth. 74

5.1 Flowchart for the proposed 3D-to-3D diffeomorphic registration algorithm 78

5.2 Code snippets to perform the computation of the contours using the forward and reverse displacement fields as well as the ED and ES input contours. 86
5.3 The Bland-Altman plot for the ground truth volumes versus the volumes resulting from the proposed method. The bias is indicated by a red line, and the limits of agreement by two yellow lines. The reference line is indicated in black. 94
5.4 Example volume curves from one patient from the ACDC MRI dataset. The ground truth is displayed in red filled circles, and the proposed method is displayed in neon green squares. The other registration methods are shown in dotted lines without markers. 95
5.5 Difference in the mesh between the ground truth and the proposed method in the ACDC dataset for a frame in the systolic phase: (a) Proposed method (b) Dipy (c) Demons (d) Demons fast symmetric forces (e) RealTiTracker - L_2L_2 (f) RealTiTracker - L_2L_1 (g) Elastix (h) Colorbar 96
5.6 Difference in the mesh between the ground truth and the proposed method in the ACDC dataset for a frame in the diastolic phase: (a) Proposed method (b) Dipy (c) Demons (d) Demons fast symmetric forces (e) RealTiTracker - L_2L_2 (f) RealTiTracker - L_2L_1 (g) Elastix (h) Colorbar 97
5.7 Example trajectory plots from a patient from the ACDC MRI dataset, where the figure on the left displays the (a) ground truth and the figure on the right displays the (b) proposed method. 97
5.8 The Bland-Altman plot for the ground truth volumes versus the volumes resulting from the proposed method. The bias is indicated by a red line, and the limits of agreement by two yellow lines. The reference line is indicated in black. 100

5.9 Example volume curves from one patient from the Mazankowski ultrasound dataset. The ground truth is displayed in red filled circles, and the proposed method is displayed in neon green squares. The other registration methods are shown in dotted lines without markers. . . . 101

5.10 Difference in the mesh between the ground truth and the proposed method in the Maz dataset for a frame in the systolic phase: (a) Proposed method (b) Dipy (c) Demons (d) Demons fast symmetric forces (e) RealTiTracker - L_2L_2 (f) RealTiTracker - L_2L_1 (g) Elastix (h) Colorbar 102

5.11 Difference in the mesh between the ground truth and the proposed method in the Maz dataset for a frame in the diastolic phase: (a) Proposed method (b) Dipy (c) Demons (d) Demons fast symmetric forces (e) RealTiTracker - L_2L_2 (f) RealTiTracker - L_2L_1 (g) Elastix (h) Colorbar 103

5.12 Example trajectory plots from a patient from the Mazankowski US dataset, where the figure on the left displays the (a) ground truth and the figure on the right displays the (b) proposed method. 103

5.13 Examples from a patient from the MRI dataset (first row) and a patient from the US data (second row). The first column shows the warped image, the second column displays the determinant of the Jacobian map from using the diffeomorphic constraints, and the third column displays the determinant of the Jacobian map without using the constraints. The regions of interest inside the circle are indicated by an arrow, where mesh folding has occurred for the case where no diffeomorphic constraints are applied. 105

Abbreviations

2DUS Two-dimensional ultrasound imaging.

3DUS Three-dimensional ultrasound imaging.

AAM active appearance model.

ASM active shape models.

BA Bland-Altman.

ECG electrocardiogram.

ED end diastolic.

EDV end diastolic volume.

EF ejection fraction.

ES end systolic.

FFT Fast Fourier Transform.

HD Hausdorff distance.

LOA limits of agreement.

LV left ventricle.

MAD mean absolute distance.

MRI magnetic resonance imaging.

ROI region of interest.

SV stroke volume.

US ultrasound.

Chapter 1

Introduction

1.1 Clinical overview and motivation

In this chapter, an overview is provided concerning the basic cardiac anatomy and function. The basics of ultrasound (US) imaging are then touched upon, with a focus on three-dimensional (3D) US imaging. This thesis then describes the use of the US in evaluating and diagnosing cardiac function. Definitions of common clinical metrics are provided, and an overview of software programs and methods employed for diagnosis. The current challenges in cardiac image analysis are highlighted, and the disadvantages of using 3DUS imaging, and issues in using clinical software packages.

1.1.1 Heart anatomy and function

Heart anatomy

The heart is the central part of the circulatory system and is a powerful muscle designed to receive and pump blood throughout the body through various vessels. The right side is responsible for receiving deoxygenated blood from the entire body, and sending it to the lungs. The lungs oxygenate the blood and it returns to the left side of the heart. The left portion of the heart is responsible for pumping the oxygenated blood to the rest of the body [1].

The image in Figure 1.1 [2] displays the basic anatomy of the heart. Each side of the heart consists of two chambers, the upper chambers known as the atria, and

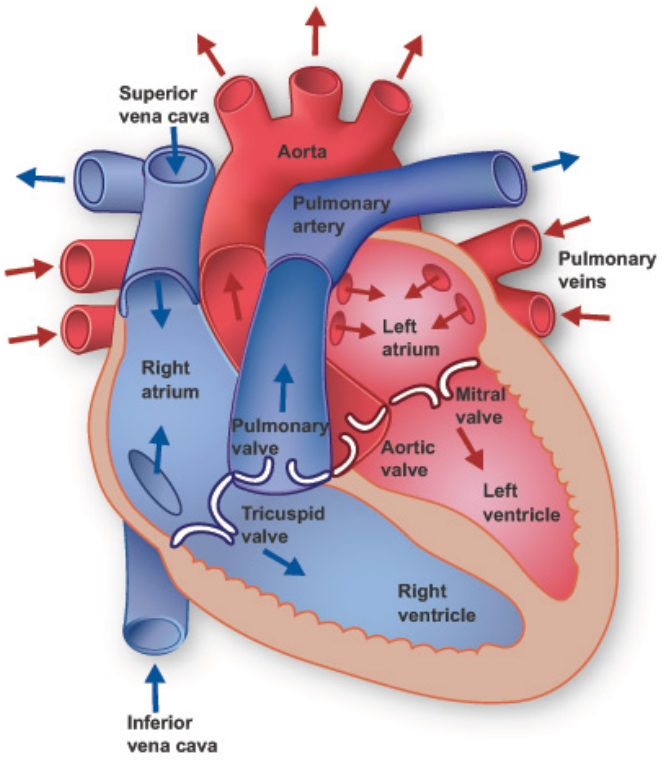

Figure 1.1: Basic anatomy of the heart [2].

the lower chambers, the ventricles. The deoxygenated blood is received from the body through the inferior vena cava and the superior vena cava. Blood then flows through the right atrium into the right ventricle which pumps blood to the lungs. The lungs oxygenate the blood, and the oxygenated blood enters the heart through the pulmonary veins, where it passes through the left atrium and mitral valve. The left ventricle (LV) receives the oxygenated blood and pumps it through the aortic valve and the aorta to the rest of the body [1].

The heart itself is comprised of three layers of tissue. The outermost layer is the epicardium, the middle is the myocardium and the innermost layer is the endocardium. The myocardium is the thickest muscular layer, responsible for pumping the blood.

Cardiac function and cycle

An electrocardiogram (ECG) is used to monitor and assess the heart's electrical activity over a specific amount of time. The use of the ECG offers a quick, non-invasive

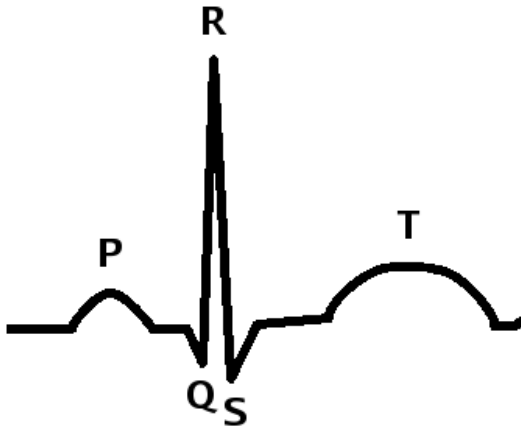

Figure 1.2: An example of an ECG wave [4].

method of determining the heart's rhythm. It is especially useful in aiding in the detection and diagnosis of a heart attack [3, 4]. The ECG can observe the small changes in electrical activity.

1.1.2 Ultrasound imaging

Echocardiography or US imaging is a non-invasive modality often used for the assessment of cardiac function. US imaging offers multiple advantages compared to other available modalities. One of the significant advantages is that there is no use of ionizing radiation, a disadvantage of cardiac catheterization or computed tomography (CT), which allows for repeated scans during a short time interval. Secondly, the US machine is extremely portable, and can be used in any area of a hospital, and also in outpatient and remote settings. Along with portability, echocardiography is also a cost-effective modality [5].

US imaging of the heart consists of both two-dimensional (2D) imaging and 3D imaging over time. There are several advantages of using the 3D modality compared to the traditional 2D approach. One vital difference is that with 3D imaging, foreshortening does not occur, which is when the plane of the US probe does not pass directly through the actual apex of the heart [6]. The presence of foreshortening could cause an underestimation of the LV volume, as the distance from the perceived

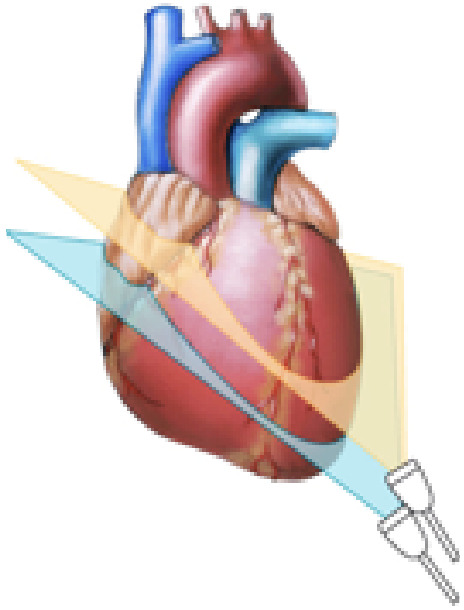

Figure 1.3: An example of foreshortening in the 4-chamber view that can occur with use of a 2DUS probe [7]. The blue plane is capturing the true apex, while the yellow plane is foreshortened.

apex to the base is smaller. Figure 1.3 displays an example of foreshortening in a 4-chamber view, where the blue plane is capturing the actual apex of the heart, and the yellow plane is causing foreshortening.

Another significant advantage of employing 3DUS is that the modality does not employ assumptions about the shape and geometry of the LV unlike with 2D imaging [6, 8]. Many analysis methods that rely on 2DUS imaging require a geometrical model for the LV, which may not be appropriate in representing the anatomy of all patients.

Regional wall motion analysis and inspecting the wall thickness are crucial parts of diagnosing disease in a patient. It can provide insight into specific areas of the heart that are functionally abnormally. With 2D imaging, the sonographer may have to modify the orientation of the transducer to observe a particular segment of the myocardium. The use of 3DUS allows for a much larger volume to be captured [8]. Apart from regional analysis, 3DUS enables the ability for valves to be analyzed and characterized [8].

There are a few disadvantages of using 3DUS compared to 2D. One is the slightly lower temporal and spatial resolution [8–10]. Another disadvantage is the presence of artifacts, which also occur in 2D conventional imaging [11]. These artifacts include speckle noise, which is a type of noise due to the nature of US imaging. It is caused by the fact that the echoes from the transmitted waveform interact with each other [12]. Depending on the method used for capturing the ultrasound data, stitching artifacts may also be present [9, 10]. Another disadvantage is the inability to capture the entire cardiac structure in one imaging plane or volume. One way to remedy this is to use a wide sector angle or to employ fusion techniques to combine information from multiple US volumes [13].

The benefits and advantages of the use of 3DUS outweigh the few drawbacks for performing LV global and regional analysis. 3DUS allows for the complete motion analysis of the LV without using geometric assumptions concerning the shape. 3DUS also ensures that the entire LV is captured without the possibility of foreshortening.

1.1.3 Evaluating cardiac function using ultrasound imaging

US imaging allows for the diagnosis and detection of cardiac-related diseases and abnormalities. With specialized clinical software, a cardiologist can obtain specific metrics derived from the volume sequence.

Clinical metrics

Several standard clinical metrics are employed for the diagnosis of various cardiac diseases. The end-diastolic volume (EDV) is the volume of blood inside the LV when it is the largest (at the end of the diastolic phase), and the end-systolic volume (ESV) is the volume of the LV when it is contracted (at the end of the systolic phase). Two metrics can be calculated from these values, the stroke volume (SV) and the ejection fraction (EF).

At the end of the systolic phase of the cardiac cycle, the blood present has been

ejected into the aorta from the LV. From there, the blood will leave the aorta to supply the body with oxygenated blood. The SV is the difference between the EDV and the ESV [14] as expressed by (1.1):

$$\text{SV} = EDV - ESV \tag{1.1}$$

The cardiac output can be calculated by multiplying the SV with the heart rate, where a low value indicating that the heart is failing to pump enough blood each time it beats.

One method used to measure the efficiency of the heart at pumping blood is to report the EF. The difference between the EDV and the ESV is first calculated and then divided by the EDV by (1.2):

$$\text{EF} = \frac{EDV - ESV}{EDV} \times 100\% \tag{1.2}$$

The result is reported as a percentage that indicates how much blood the LV pumps out with each beat. A low EF would indicate that the heart is unable to pump out enough blood, indicating a potential problem with the LV.

Measuring the volume of the LV for each frame in the cardiac cycle can also be performed. The general shape of the volume curve in systole and diastole can aid the clinician in identifying potential diseases. Figure 1.4 gives an example of a volume curve obtained from a patient that was analyzed by a cardiologist using the TomTec Arena software (TomTec Imaging Systems, Unterschleissheim, Germany).

Clinical software overview

Cardiologists and other clinicians use several clinical software packages to aid in the diagnosis of the LV. I will focus on three algorithms from different software packages. One performs an implementation of Simpson's biplane method, a commonly used approach for obtaining a segmentation for the ED and ES phases. Another method uses a traditional speckle-tracking approach to perform segmentation over the complete

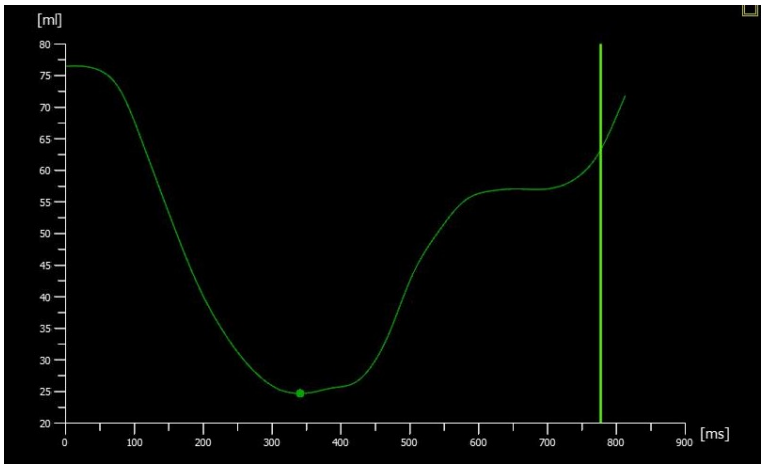

Figure 1.4: An example of a volume curve from the TomTec clinical software, obtained using 3D speckle tracking over the cardiac cycle [15].

cardiac cycle. The last method utilizes a model of the heart along with artificial intelligence to analyze the LV.

Simpson's biplane method One standard clinical software is TomTec Arena (TomTec Imaging Systems, Unterschleissheim, Germany), in which Simpson's biplane method is implemented as part of the AutoLV software. In the original Simpson's biplane algorithm, the user manually traces the endocardial borders in two orthogonal slices. The two orthogonal slices can be obtained from 2D echocardiography or 2D slices obtained from a 3D dataset. These orthogonal slices are the apical 2-chamber the 4-chamber view. Once the borders are traced, ellipsoidal discs are automatically created from the apex to the base, and the volume of each is computed and summed. The AutoLV software automatically delineates the endocardial borders instead of relying on manual segmentations as demonstrated in Figures 1.5 and 1.6. This process is repeated for the ES volume, and the final measurements of this algorithm include the EDV, ESV, and EF.

Speckle tracking method TomTec Arena also implements a method for obtaining a delineation of the LV over the full cardiac cycle using speckle tracking, a method that examines the tissue motion by analyzing speckle patterns. The individual steps

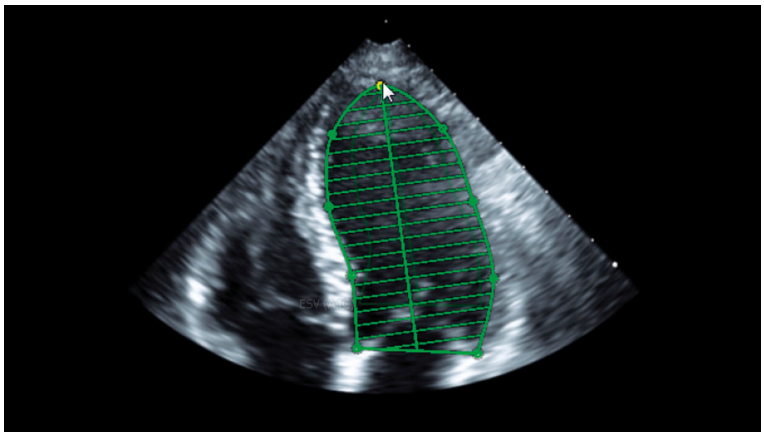

Figure 1.5: Automated delineation of the LV with ellipsoidal discs generated between the apex and base. These discs are summed to obtain the volume of the chamber [15].

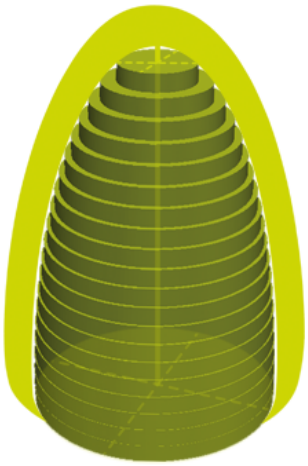

Figure 1.6: The ellipsoid discs created between the apex and the base of the LV [15].

are displayed in Figure 1.7. The clinician first identifies the apex and the mitral valve, and the LV is aligned vertically according to these two points. A rough estimation of the endocardial borders is automatically produced for the ED and ES frames, where the clinician has the opportunity to adjust them. Tracking (using a speckle tracking method) is then initiated and revised if necessary. The final results include volumetric measurements, regional analysis, and metrics concerning the strain [15].

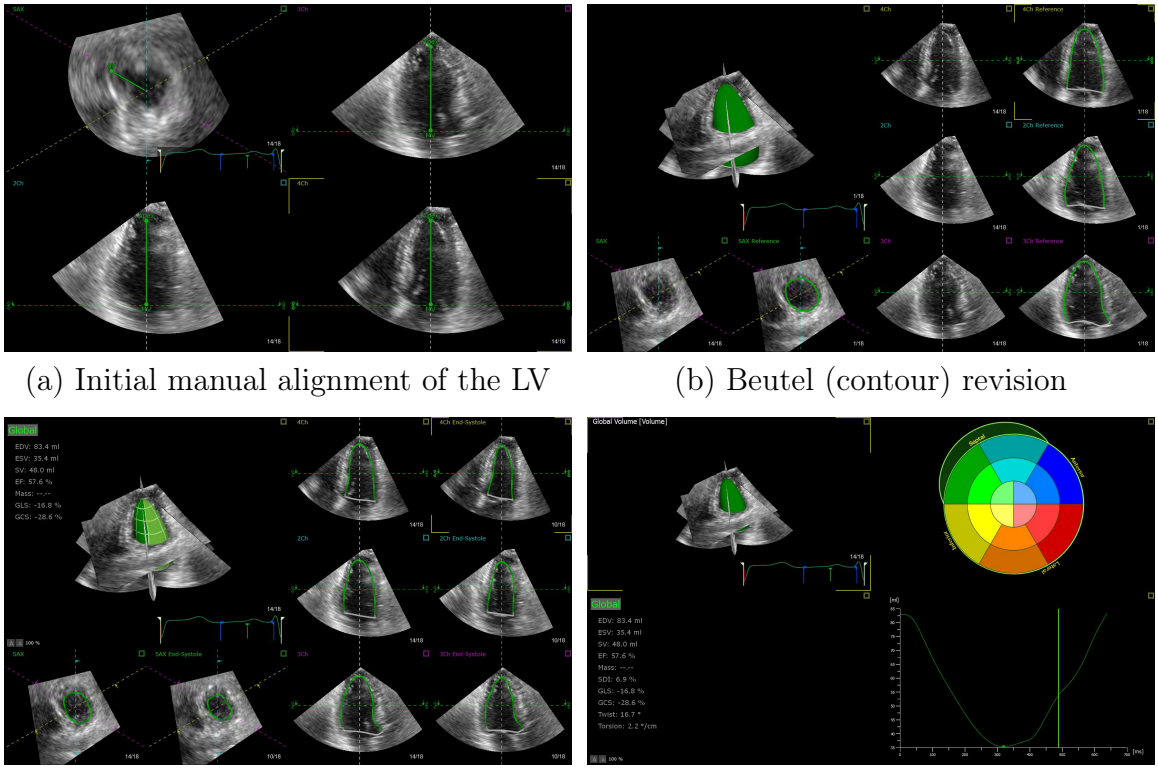

(a) Initial manual alignment of the LV

(b) Beutel (contour) revision

(c) Tracking revision

(d) Final results produced

Figure 1.7: The process for semi-automated delineation of the LV endocardium across the cardiac cycle using the TomTec Arena software [15].

Philips Dynamic HeartModel Philips has developed a set of algorithms based on artificial intelligence [16], to perform a thorough cardiac assessment. The heart model developed by Philips to inform the segmentation process on a new patient is displayed in Figure 1.8. The model was trained and developed using 1,000 echocardiography images from a dataset with a variety of factors including differences in image quality, the shape of the heart, and the size. It can be seen that all chambers are analyzed

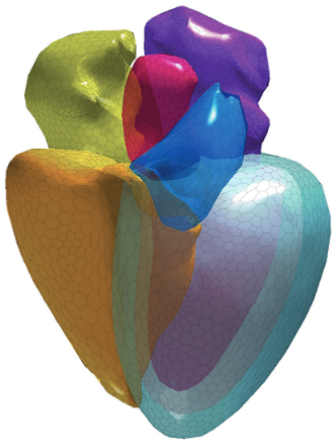

Figure 1.8: Dynamic HeartModel developed by Philips [16].

within this model of the heart. The clinical workflow consists of a series of steps to perform the full cardiac assessment, as demonstrated in Figure 1.9. Within a 3D volume, a standard apical 2-chamber and 4-chamber view are automatically detected to localize the heart. Chamber alignment is then performed on a finer scale to obtain a more accurate orientation and position of the particular chamber's model. On the following finer scale, regional alignment is performed where the borders of the model and adjusted to align closely with the underlying image.

Disadvantages of methods in current clinical software One drawback of Simpson's biplane method from TomTec Arena is the assumption that is made about the shape of the LV. Ellipsoidal discs are created between the delineations of two orthogonal contours. For patients with severe abnormalities or other cardiac-related issues, the ellipsoidal discs may not capture the true geometry of the LV. Speckle tracking faces several challenges [17], such as the need for a good acoustic window is necessary, as well as datasets of high image quality. For artificial intelligence methods, it is vital to employ the use of a dataset that is comprehensive and varied, in order to adapt to a wide variety of patients. With the Dynamic HeartModel model-based segmentation method, it may not adapt to a patient's heart that contains substantial structural differences. This may be an issue for patients that suffer from congenital

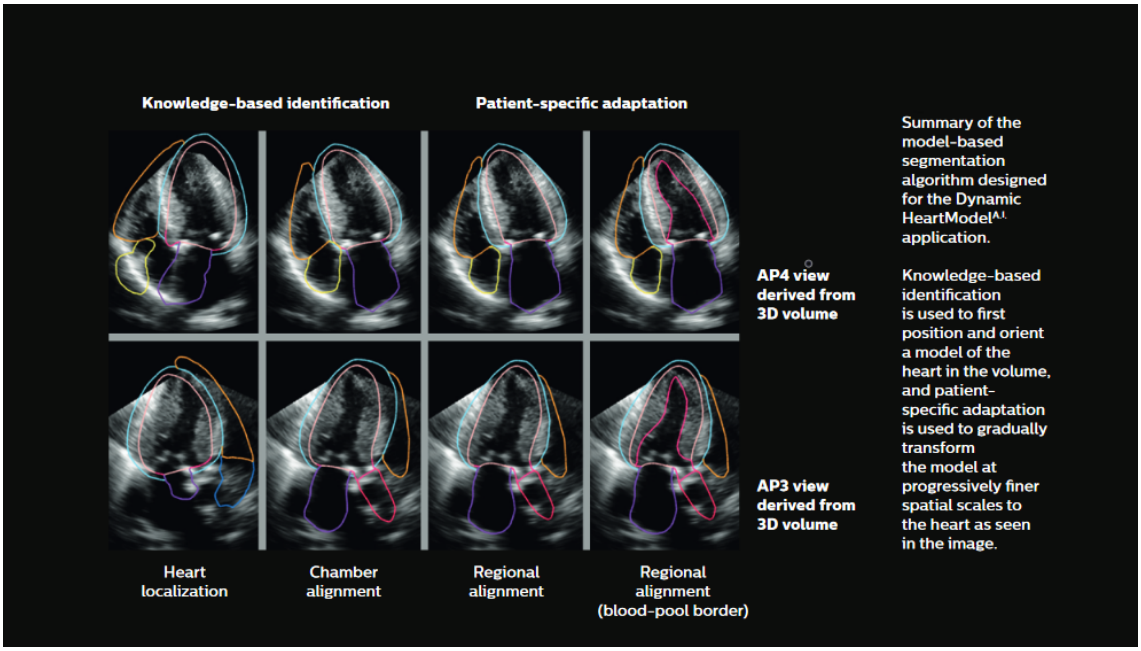

Figure 1.9: Clinical workflow using Dynamic HeartModel from Philips [16].

heart diseases.

1.2 Thesis contributions

An overview is provided of the contributions in this thesis within the field of medical image segmentation and registration for cardiac image analysis.

3D spatial segmentation in ultrasound volumes

This thesis proposes a 3D segmentation algorithm to be used for semi-automated delineation of the endocardium of the left ventricle in ultrasound volumes. A 2D diffeomorphic algorithm is used to perform spatial registration on a set of angular slices that pass through the axis of the chamber. Providing an initial set of two contours allows the algorithm to generate a dense set of contours that capture the various patients' cardiac anatomy.

3D temporal segmentation in ultrasound volumes

Further development to the 3D spatial segmentation algorithm was performed by applying it to the left ventricle segmentation for the entire cardiac cycle. The delin-

eation of the chamber over the complete cardiac cycle enables cardiologists and other clinicians to perform a full diagnosis of a patient.

3D-to-3D diffeomorphic registration algorithm

I propose a 3D-to-3D diffeomorphic registration algorithm that can be used to capture the actual cardiac motion across the complete cycle. Starting with a delineation of the end-diastolic and end-systolic frames, the method can automatically generate a segmentation of the rest of the frames in the cardiac cycle. The method allows for setting constraints that control the amount of deformation, resulting in plausible displacements for cardiac tissue.

1.3 Thesis overview

For the subsequent chapter, previous works in the literature are presented in areas of cardiac image registration, as well as segmentation for the end-diastolic and end-systolic frames and over the complete cardiac cycle. The focus is on traditional methods as well as newer machine learning (deep learning) approaches. Chapter 3 presents a 3D spatial segmentation algorithm that is used to segment the left ventricle at end-diastole and end-systole. A 2D diffeomorphic registration algorithm is used to perform semi-automated segmentation of the endocardium of the left ventricle. I evaluate the approach on a public set of ultrasound scans at end-diastole and end-systole against nine other segmentation methods. Chapter 4 presents a 3D temporal segmentation algorithm that extends the previous formulation. The method was evaluated on patients from the local hospital against publicly available software packages for registration. Chapter 5 presents a 3D-to-3D registration method that can capture the true cardiac motion over a complete cycle. The proposed method is compared against publicly available software packages for registration methods for both magnetic resonance imaging (MRI) and ultrasound sequences. In the last chapter, the work performed for this thesis is summarized, and future work and limitations are

discussed.

Chapter 2

Background

2.1 Image registration overview and methods in literature

2.1.1 Basics of image registration

Image registration is the process of aligning two or more images or volumes to each other, where it is used in a wide variety of medical imaging applications. For instance, in radiotherapy applications, multi-modality registration is often used, where CT is used as the primary modality to obtain the necessary information for dose calculation and must be registered to an MRI scan which is used for the delineation of the anatomical substructures [18]. In brain imaging, regions of interest (ROIs) are often created by clinicians to delineate white and gray matter substructures. The process can be time-consuming, and therefore atlases are created to represent the average brain, which is then registered to the patient's brain and the deformation fields applied to the substructures to obtain the patient ROIs [19]. Image registration can also be used in the temporal domain, where patients are registered to detect anatomical differences and changes over time.

The examples provided demonstrate the usefulness of medical image registration for a wide variety of problems. Image registration itself can be used to optimize for several different types of transforms using a minimization process of a dissimilarity metric between the two images or volumes. One type of transform that can be solved

for is a rigid transform, consisting of scale and rotation parameters. This can be extended to affine transforms, which can represent scale, rotation, similarity, shear, and translation.

When capturing cardiac motion over the cycle, it is crucial to use a specific class of transforms known as deformable transforms [20]. The heart is a highly dynamic structure whose anatomy varies across patients and can suffer from significant structural changes. Therefore, it's crucial to use deformable transforms, capturing the non-linear changes in the images. Methods for cardiac image registration that use deformable techniques are discussed in the following section.

There are several specific reasons as to why cardiac image registration is performed [21]. One of the most important reasons is for image segmentation, where many of the typically used cardiac indices require the delineation of the endocardium, myocardium, or epicardium. This delineation process is time-consuming for clinicians to perform. Therefore image registration is used to extract these segmentations in a faster and more time-effective manner. Often image registration is performed to align the volumes, and the deformation fields are applied to an initial set of contours from a single frame.

During cardiac image acquisition, respiration causes the patient's body to move. Gating or synchronization to the heartbeat and/or respiration cycle is often used to obtain a set of volumes. Unfortunately, misalignment of the volumes may still occur. Motion artifacts may also occur because of unwanted patient movement. To perform an accurate analysis of the patient over time, the volumes must be aligned to a common reference frame. Therefore image registration is used to perform this alignment.

Image fusion is the process of combining information from multiple scans to increase the field of view (FOV) of the heart. This is often performed as the entire heart may not visible within the obtained scan. To align the multiple volumes and observe the relevant structures, image registration is often employed.

2.1.2 Cardiac ultrasound image registration in literature

Several approaches have been developed for computing the deformation fields that capture the motion of the LV in echocardiography sequences. A large portion of these methods performs registration to capture 3D strain information, providing insight into the regional myocardial function. Other approaches focus on applying the deformation fields delineate the LV over time, where the segmentation can be used to obtain volumetric information.

In the past, tagged MR sequences were used for strain analysis [22]. US is now preferred as the spatio-temporal resolution is higher and the cost is lower. Therefore 3DUS has been adopted to perform strain analysis.

We divide the methods for US registration of the LV into three main areas [23]. The first is intensity-based, where methods such as elastic registration are discussed. The second registration area includes regularization model-based methods, where free-form deformation approaches and extensions are applied. Lastly, current deep learning methods for capturing the LV motion are discussed.

Intensity-based methods

One of the early methods relies on intensity-based spatio-temporal registration using an elastic approach to measure the strain [22]. In particular, a B-spline transformation model is employed, and mutual information is used as the similarity metric. A multi-resolution approach was used, along with regularization to enforce the smoothness of the deformation field.

In another study, a non-rigid registration technique using the spherical coordinate system was proposed [24]. The authors developed a new similarity metric based on a derivation from the maximum likelihood formulation, where the new metric incorporates the actual physical properties of the US volume. The measure assumes that the speckle noise is blurred and that the Rayleigh noise in the two images being registered is correlated. Instead of using the US images that clinicians use for diagnosis, the

data from the previous step of image formation, the envelope-detected image in the spherical coordinate system was used. One advantage of using the envelope-detected image is that there is less information loss which comes from converting the data to Cartesian coordinates and avoiding interpolation.

Regularization model based methods

A registration technique using an anatomical free-form deformation model has been developed [25]. One disadvantage of using the B-spline transformation model is that the control points for the B-spline are defined in Cartesian space on a rectangular grid [22]. This formulation may not be optimal as the spatial smoothness criteria are not enforced in directions (e.g. radial) appropriate for cardiac images. Therefore the proposed method incorporates the use of basis functions that are aligned in the radial, longitudinal and circumferential directions with respect to the endocardium. This formulation more closely follows the actual motion of the heart.

An extension was proposed in [26] based upon [25], which incorporates the use of volume conservation in addition to the already established anatomical free-form deformation model. The myocardium has been shown to be close to incompressible, a property that can be exploited when modeling the deformation fields. One method of enforcing volume preservation is to observe the Jacobian determinant, where compression occurs if the determinant is less than 1, and expansion occurs if the value is greater than 1. For the myocardium, the value of the Jacobian determinant should be equal to 1 for volume preservation to hold.

A temporal diffeomorphic free-form deformation algorithm was proposed to assess both the motion and strain of the LV [27]. B-spline kernels are employed in both a spatial and temporal manner to represent the velocity in 3D+time data. The objective function that is minimized is comprised of both an image similarity term as well as a regularization term, where the sum of squared differences is used as the image similarity. For the regularization, a term representing the constraint on the

incompressibility of the myocardium is employed.

The diffeomorphic free-form deformation methods [27] was extended by [28]. A new similarity metric that incorporates the underlying physics of the US volumes was proposed. The similarity metric used previously in [27] was the sum of squared differences, which was used to compare the first frame to the subsequent frames. In the proposed method, this was then combined with another metric computed for adjacent frames that are based on the property that speckle noise is correlated [29].

A temporal sparse free deformation method was proposed using concepts of compressed sensing to employ the use of a sparse representation [30]. Sparsity is included in the formulation of the deformation field as part of the L1 regularization process. One current issue with using the classic free-form deformation method is that it may be unable to capture deformations that occur locally that are discontinuous. This is because of the control points and spacing used in the formulation, where a coarse spacing likely cannot capture these particular deformations. However, using a finer grid spacing increases the complexity of the optimization problem. Therefore, the benefit of using a sparse representation is that local and global deformation can be modeled without compromising on accuracy and robustness. This methodology was extended to perform temporal sparse free-form deformations.

Another method for registration involves the use of a diffeomorphic motion estimation approach applied temporally [31]. The significant difference between this method and others is that the velocity field is optimized instead of optimizing the displacement field. A new similarity function was developed known as the intensity consistency error, where multiple time points are used instead of only evaluating the deformation field between a pair of frames. The pairwise frame comparison using both adjacent frames and the reference to subsequent frames are combined. Since multiple successive frames are used to estimate the velocity field, there is increased smoothness in the temporal direction.

Deep learning-based image registration methods

One method that is often used for motion estimation in an echocardiography sequence is speckle tracking. Unfortunately, this method may result in poor tracking of the LV because of image artifacts or issues inherent to US imaging. Therefore many methods have been developed to overcome the issues of speckle tracking by the inclusion of regularization. A method to perform jointly spatial and temporal regularization by representing the motion field in terms of dictionaries was proposed [32]. In particular, sparse dictionaries were employed. This method was then extended by [23] to use deep learning techniques for strain analysis. A feed-forward neural network was used in order to perform regularization jointly in the spatial and temporal domain. Specifically, a multi-layer perceptron was used to learn this particular regularization function.

2.2 3D segmentation methods in literature

Several approaches exist in the literature for performing 3D segmentation of the LV in 3D echocardiography volumes. These methods can be divided into three main areas, the traditional methods, machine learning methods (non-deep learning-based) and those based on deep learning.

2.2.1 Traditional methods

Graph cuts, level sets, and other variational methods

A semi-automated graph cuts-based method to perform the 3D segmentation of the endocardium of the LV was proposed [33]. The first step is to convert the image volume from the Euclidean space to the spherical-cylindrical space, by selecting the base, the apex, and the hinge points of the mitral valve. This enforces the U-shaped prior necessary for the segmentation. Next, the graph cuts algorithm is employed to perform the endocardial wall segmentation, where a data term and a smoothness

term are used. The goal of the data term is to ensure that the endocardial center line previously defined by the user is on voxels that have a large gradient value (at the apex and base). The smoothness term ensures the surface that is formed is smooth and that there are no significant discontinuities. After graph cuts are employed, the segmentation is converted back to the Euclidean space.

A graph cuts-based approach along with a radial symmetry transform was employed to delineate the LV [34]. The radial symmetry transform was first used to transform the dataset into the cylindrical coordinate space. The method presented is fully automatic and does not require any user input or initial models, such as in the case of active shape models (ASM). The Fast radial symmetry transform is first employed for the z slices for the apex and the base. The local maxima of the transform is then determined for these two slices after removing maxima outliers, resulting in a central axis for the ventricle. Each z plane or short axis slice is then converted to the polar coordinates, where the final volume is in cylindrical coordinates. The graph cuts algorithm is then used in the cylindrical coordinate system, and the final segmentation result is converted to the Euclidean coordinate system for comparison to the ground truth.

Random forest-based methods

A method using Hough-forests with the inclusion of appearance and shape information was proposed for LV segmentation [35]. An advantage of using Hough-forests is that, unlike statistical shape models (SSM), they do not require complex construction, and initialization is also unnecessary. For preprocessing, the intensity histograms are equalized, and two regions are defined: the foreground is set to be a band around the ground truth, and the rest is considered to be the background. Random forests are generally used for classification, while the Hough-forest uses a voting technique to localize an instance of an object. Therefore, the use of segmentation and intensity patches was included, enabling the Hough-forest to produce a segmentation contour.

For training, each data point has associated features, as well as a segmentation patch and an intensity patch, and a vector that gives information about the direction towards the center of the LV. Each tree is then trained, which is split until leaf nodes are created, and a termination criterion is fulfilled. For testing, the same features are taken from the test volume and the forest is traversed until a leaf is reached.

Random forests have also been used employed to perform segmentation of the LV [36]. Instead of using only two classes, the LV and the background, the proposed method includes the myocardium and the mitral valve as additional classes. The approach uses random forest classifiers with the auto context method [37]. The idea of the auto context method is that first, a classifier can be learned on a set of training image patches and their associated label maps. The class confidence maps produced by the first classifier are used in conjunction with the original image patches to train a secondary classifier. This is performed iteratively until it approaches the ground truth.

Lastly, a semi-automated method based on structured random forests has been developed for segmentation involving two steps [38]. The first step consists of generating possible boundary candidates to define the endocardial border of the LV. A structured random forest (SRF) is used for each short-axis slice, where it detects potential boundary candidates for the endocardium. The crucial difference between an SRF and a random forest (RF) is that the SRF allows for a patch-by-patch approach for prediction instead of pixel-by-pixel. Once the SRF is trained for each short-axis slice for ED and ES, the second step involves the deformation of the surface model deformation to a portion of the boundary candidates for each patient's volumes.

Model based segmentation methods

The use of active appearance models (AAM) has been investigated for endocardial segmentation [39]. AAMs often use principal component analysis (PCA) on training data to generate an organ's mean appearance and represent the shape and texture.

They are particularly useful, especially for US data, as they can capture variations that are often seen in the LV. AAMs often require a large amount of training data to create the model, which may not be feasible. One method of addressing this is to use a Jacobian-tuning method [40] which updates the Jacobian instead of keeping it fixed throughout the iterations of forming the AAM. The approach of [39] was extended in [41], where an AAM was also employed for segmentation. In another method, separate models were created by the authors for the ED and ES frames, by using a combination of the CETUS public dataset and a secondary dataset comprised of previously acquired US volumes [41]. Experiments were performed to test the effect of various initialization strategies by varying the center and the mean.

Shape models have been employed to detect both the endocardium and epicardium boundaries [42]. A boundary fragments model (BFM) was used, which can represent a particular object solely based on portions of the boundary. In contrast to other methods, the purpose of the BFM is to model parts of the edges of the object, which are then used for generating features for detection. The BFM finds the center and the scale of the object of interest given a candidate edge map, performed by using a boosted classifier.

A method known as the probabilistic data association filter was developed for LV segmentation [43]. The user first provides an initialization of the LV in three orthogonal planes, where a mesh is then formed using the technique of space carving. Feature detection is then performed, where first an edge detector is employed. Patches or middle-level features are then formed based on the initial detection. A model estimation technique based on an extension of the PDAF is then used to divide the points into whether or not they belong to the ventricle boundary.

A semi-automated method for delineation of the LV endocardial borders was developed [44]. A multi-scale quadrature filter is used to form a phase image of the US volumes as a preprocessing step. This type of filter combines a ridge-picking filter with an edge-picking filter, appropriate for highlighting the different areas of the LV

(myocardium and blood pool). Applying this to US volumes results in the myocardial region exhibiting a positive real value. In contrast, regions inside the blood pool have negative real values, enhancing the ventricular borders. A model-based level set method is then used to perform the endocardial segmentation. An SSM is used as input for the level-set algorithm, where the user is required to initialize the model.

A method based on the use of a mesh model created using mean value coordinates and then tracked using a Kalman filter was proposed [45]. A fully automated approach was developed using this method. To create the reference mesh, the LV mesh of the first subject at ED from the CETUS dataset was used. In order to perform the deformation of the mesh, the mean value coordinates system is used. To perform tracking, the state of the mesh is comprised of local and global parameters describing the transformation. A Kalman filter is used to perform the prediction of the state of the mesh.

Structured random forests along with an ASM have been used for endocardial segmentation [46]. One common set of errors when using structured random forests is that they may produce edge probability maps that are incorrect in some regions, such as signal dropout areas. In those cases, a shape prior using ASM can help correct implausible LV shapes. A structured random forest was trained on image patches from the US volumes, and contextual information for the hand-crafted features. For instance, features such as the gradient magnitude and the histogram of oriented gradients were employed for multiple scales. Once the edge probability maps have been formed, the ASM is employed for the segmentation.

Other methods have been developed for segmentation followed by tracking [47]. The first step involves the creation of an initial model of the chamber, in which the method of [48] is used. Once the model is created, the ED frame is automatically segmented using the B-spline explicit active surfaces (BEAS) method [49]. In this method, the edge of the object is represented by a function, where a coordinate of one point on the surface is described using the other coordinates. Additional

hyperparameter terms are included in the formulation in order to address the fact that the ground truth endocardial contours are not exactly at the interface of the blood and the myocardium. For tracking of the LV throughout the cardiac cycle, two steps are employed. First, an affine optical flow approach is used to generate a rough estimate of the global deformation. For a more precise deformation, the block-matching approach is used.

2.2.2 Atlas based segmentation methods

Atlas-based registration is a method that has been employed to perform the segmentation of anatomical structures. It has been applied widely in the area of brain imaging but has not been used as often in the area of cardiac imaging because of the difficulty of performing non-rigid registration for echocardiography images [50].

A multi-atlas segmentation approach has been proposed [51]. The algorithm begins by first preprocessing the volumes of the patients to reduce speckle noise, by using a sparse representation of learned dictionary atoms. A novel shape representation was developed by the authors and was extracted from patches of the echo data, where the representation can provide information about the local shape information. These representations are learned by mapping the manifold structure of these patches to a low-dimensional space. An atlas is created from a set of training data, and labels are propagated from a subset of these by using a combination of linear and deformable registration.

Another multi-atlas segmentation approach was proposed by [52]. A method was developed for the representation of the 3D boundary of the ventricle, termed the probabilistic edge map (PEM). The PEM denotes the boundaries of the objects by employing a structured decision forest (SDF) classifier. Global alignment is first performed between the target and the atlas PEMs by use of a block matching algorithm. The most similar atlases are then selected using an average local correlation coefficient metric. Since the PEMs have been aligned using an affine transform, free

form deformation is then used to perform the fine alignment. To perform the final segmentation, the labels from the atlases are fused and transformed to the patient.

A second method for atlas-based approaches has been proposed [50]. Features such as the image intensity, local phase, and local geometric information are extracted from a compounded 3D echo volume. The technique of [53] is used to perform the registration of the atlas to the patient, known as the locally affine registration method (LARM). The process consists of three steps, (1) detection of the heart is performed a rigid registration, (2) LARM is used for performing further initialization of the four anatomical structures, the four chambers, (3) free form deformation is then applied to perform a more precise registration.

2.2.3 Deep learning-based segmentation methods

Artificial intelligence methods have become popular within the last few years with deep learning techniques and computing power. Several methods have been proposed that use deep learning for echocardiography segmentation.

An approach termed anatomically constrained neural networks (ACNN) has been developed for LV segmentation [54]. The approach includes the use of priors and labels as input to the neural network, where it is helpful in cases where there may be missing boundaries or the input volume data is not sufficient. In particular, a convolutional autoencoder is employed to learn the variations in the shape of the LV.

Another approach uses deep learning along with a snake algorithm to perform segmentation of the chamber [55]. Convolutional neural networks (CNNs) are first employed to generate a region of interest. Using as input this ROI, a stacked autoencoder was trained to learn the initial shape of the LV. A gradient vector flow 3D snake algorithm was then employed to perform the segmentation of the endocardium. This method was used as a basis for [56], where the authors combined a fully CNN with a deformable model. A coarse to fine framework is employed, where a coarse segmentation is first performed with deep learning methods, and a fine segmentation

is performed using the 3D snake approach. Instead of a stacked autoencoder methodology previously used in [55], a new method is proposed based on feature fusion with the inclusion of residual connections.

VoxelAtlasGAN is another approach proposed [57], which tries to address the issue of limited annotated datasets available for 3D echocardiography segmentation. Therefore, the authors proposed an end-to-end deep learning framework incorporating an atlas to provide prior knowledge. The method uses conditional generative adversarial networks (cGAN) in a voxel-to-voxel manner. The use of the discrimination loss (used traditionally by a GAN) is combined along with a new consistent constraint. This consistent can provide consistency with regard to the segmentation and the intensity volume. The previous approach has been modified and improved in [58]. A new constraint is proposed called the couple adversarial consistency constraint (Couple-GAN). The constraint for the volume consistency was refined by employing a similarity measure that uses the phase. The authors also performed additional experiments to further prove the robustness of the method.

2.3 3D+t segmentation methods in literature

Several methods are available in the literature that performs 3D delineation of the LV for the entire cardiac cycle. These can be divided into two major areas, the traditional methods and the machine learning methods. The traditional methods are tracking methods, optical flow approaches, graph cuts, level set methods, model-based segmentation methods, and statistical shape modeling. The machine learning methods consist of deep learning approaches.

2.3.1 Traditional methods for image sequence segmentation

Tracking methods

One of the earlier approaches for tracking the LV border throughout a sequence of volumes was proposed by [59]. A contour deformation model was used, where the

inputs are a set of points from a template and a state vector, and the output is the set of the transformed points. For the deformation parameters, translation, scaling, rotation, and bending are employed. In order to initialize the tracking, a truncated ellipsoid is used first as a template for the contours, as this model provides a reasonable initialization of the chamber. In addition to the contour motion model, a kinematic model that considers the previous two state estimates and an edge model is employed.

This method was extended in [60]. One issue with the previous method of [59] was that the use of a truncated ellipsoid required the use of additional steps to form a proper closed surface of the LV. The proposed method uses subdivision surfaces, where meshes of a wider variety of topologies can be supported. In particular, Doo-Sabin surfaces are employed [61]. The deformable subdivision model describes the local deformations, which are then combined with a global transform, used to scale, translate, and rotate the model. An extended Kalman filter is again used to perform the tracking.

The method of [59] was also extended by [62]. One of the issues with the previous approach [59] is that local and global deformations were not separated, and therefore the authors proposed a method to separate these in [62]. The deformation, therefore, consists of terms that describe both the global shape and the local changes in shape. This method of modeling was then extended by [45], where an approach was developed using a combination of mean value coordinates and a Kalman filter. The idea of mean value coordinates is that a vertex can be expressed as a combination of the neighboring vertices. The proposed method is fully automatic, where a mesh model is created using the ED mesh from the first patient of the CETUS public dataset. The number of vertices is reduced to increase the speed of the computations.

A method combining the use of a global tracker and local optical flow tracker to track the chamber throughout the temporal sequence of volumes has been proposed [63]. One advantage of using a combination of both global and local trackers is that, for instance, in cases where the LV wall is not entirely visible, the global tracker can

be relied upon more, but if the wall is visible, then the local tracker can be used more. Within the tracking framework, previous knowledge of cardiac motion is provided by the use of statistical modeling. This information was extracted from actual patient data.

Other methods using optical flow have been developed, such as one termed localized anatomically constrained affine optical flow (AAOF) [64]. Methods were incorporated from [65], which uses global anatomical affine optical flow. The method of [65] is different from other optical flow methods in the fact that the estimation of the motion is performed strictly within an anatomical ROI. This ROI can be provided by manually delineating the ED frame. By constraining the optical flow to a region, the other tissues of the heart do not cause interference. The AAOF model derived from the global model is different because neighborhood regions are considered for each surface point.

Tracking methods based on Kalman filters have been used for the segmentation of the LV. In particular, one method first uses a graph cuts- based edge detection [66]. A model of the LV is manually formed and represented by a Doo-Sabin surface. One difficulty in delineating the endocardium is due to the presence of trabeculations. This anatomy can lead to characteristics of the edge that change over the cardiac cycle. Therefore the authors developed a graph cuts-based edge detection approach using a combination of max-flow min-cut and a step criteria edge detector. These were incorporated into a Kalman filter-based tracking framework.

There have been several model-based segmentation approaches for 3D temporal segmentation. One method employs ASMs in a real-time framework and an extended Kalman filter to perform the tracking [67]. A set of manually traced LVs, 496 ventricles from 31 patients, were used to train the ASM. An extended Kalman filter was then used to perform the prediction and updating of the ASM and is based on the work of [59]. This method incorporates a motion model where the state vector incorporates the use of the last two states.

Optical flow methods

A technique using a global affine optical flow method and block matching approach has been proposed [47]. Automatic segmentation of the LV at ED is performed using the authors' previous method [48, 49] as a basis. An initial model of the chamber at ED is produced using [48], and the segmentation is performed using the BEAS approach from [49]. Two steps are used to perform the tracking. Anatomical affine optical flow is first used to generate an estimation of the global deformation [65]. A block-matching approach is then employed to generate a more precise deformation. A recursive approach is employed to use patterns from images of previous frames to improve the tracking. A similar approach has been used in [68], where only optical flow is used for the tracking instead of the combination of optical flow and block matching as in [47]. An energy term in which the affine motion estimated by the Lucas-Kanade technique for global motion is penalized.

Model based segmentation methods

An approach using an AAM for segmentation and tracking was developed [69]. An AAM model was constructed using a set of publicly available segmentations and additional datasets from the author's center. A single model is created from both of the sets of segmentations from ED and ES. Tracking was then performed by employing the initialization of the subsequent frame by using the AAM parameters for the current frame.

Statistical shape modeling methods

In echocardiography data, there is a coherence between the spatial and temporal aspects. Information about the dynamics of the heart can provide ways to inform the detection of the endocardial border by use of constraints. A limitation of the traditional methods of using statistical shape/appearance models is that it is difficult to form a comprehensive database from normal and abnormal patients. It is

difficult to take into consideration all of the different anatomical variants. This can be resolved by using online learning and using data coherence from the individual. In one approach, a method was proposed for 2D+time segmentation using a sparse representation-based technique [70]. A new approach [71] based on [70] was developed that demonstrated the use of a 3D dynamical appearance model. This method uses information such as local appearance (in a multiscale manner), intensity, and shape. As frames are segmented sequentially, and the multiscale appearance dictionaries are updated dynamically. A MAP framework incorporates the dynamical shape prediction and intensity. This work is extended by [72] with in-depth details about the implementation.

2.3.2 Machine learning methods

Deep learning methods

There have been relatively few methods using deep learning for 3D+t segmentation of the LV in echocardiography volumes. One approach performs both segmentation and tracking, where the displacement fields, as well as the segmentation masks, are generated as output [73]. The first network, the motion network, is an unsupervised framework similar to VoxelMorph [74], where the input is a stack of the source and target frame, and the output is the displacement field between the two 3D input volumes. The loss is computed as the mean square difference between the target frame and the transformed source frame. The second network, the segmentation network, is weakly supervised and similar to the 3DUNet implementation [75]. The input is the 3D target frame and the output is the 3D segmentation. The networks are combined by optimizing each separately first, and an incompressibility constraint is used to generate anatomically plausible deformation fields.

Chapter 3

3D Spatial Segmentation in US Volumes

3.1 Overview

This chapter introduces a novel semi-automated approach to delineate the LV from 3DUS imaging. The proposed method relies on a diffeomorphic registration approach and contour propagation to perform segmentation in 3D space. Figure 3.1 displays a flowchart of the 3D semi-automated segmentation method. The user chooses an axis of the LV, and angular slices are automatically created that pass through this axis. The user then delineates the endocardium of the LV on two orthogonal slices. A 2D diffeomorphic registration method is then used to create the contours for the other angular slices automatically. A mesh is then formed from the contour points transformed to the original 3D space. The spatial segmentation method was performed on both ED and ES volumes from a set of patients from a publicly available database, where ground truth delineations were created from expert cardiologists. The algorithm was evaluated using a standard set of distance, overlap, and clinical metrics. The proposed method was evaluated against four other semi-automated methods and five fully automated methods as a form of comparison.

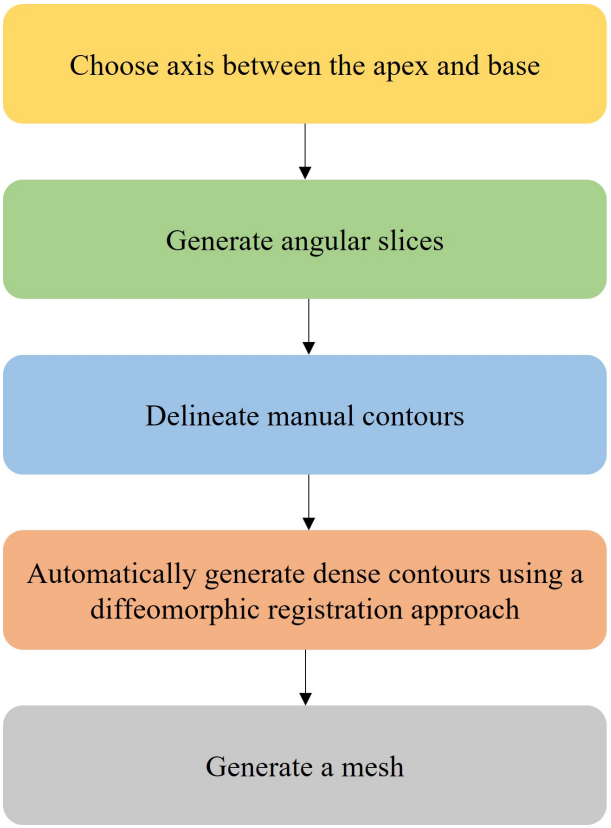

Figure 3.1: Flowchart of the proposed approach for the 3D semi-automated segmentation of the left ventricle at end-diastole and end-systole.

3.2 Algorithm

3.2.1 Creation of angular slices

The user is first required to delineate the axis of the LV, defined between the center of the mitral valve leaflets at the base and the apex of the chamber. Angular slices are then automatically generated with respect to the user-defined axis. Figure 3.2 demonstrates an example of the user-defined axis for a patient at ED.

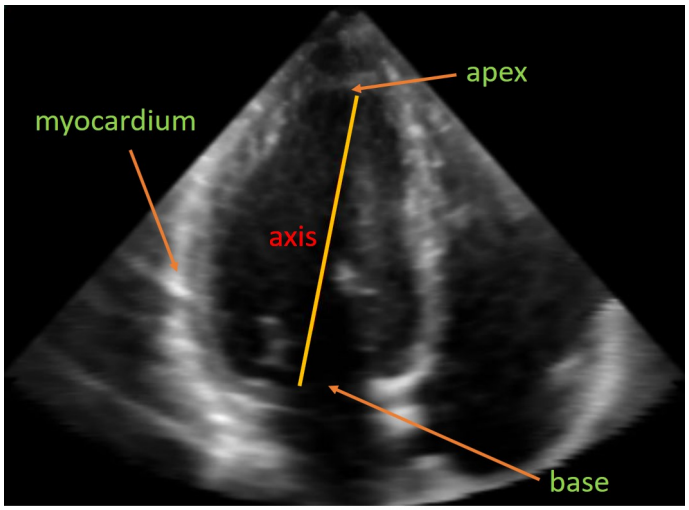

Figure 3.2: User-defined axis for the left ventricle at end-diastole.

A series of 3D geometrical transformations are used to create the set of angular slices that pass through the user-defined axis. The final geometrical transformation consists of the concatenation of the two transformation matrices. The first transformation is responsible for aligning the axis with the $\vec{u} = [1, 0, 0]'$ direction. We can define $p_1 \in \mathbb{R}^3$ and $p_2 \in \mathbb{R}^3$ to represent the user-defined points at center of the base and the center of the apex that represent the axis. The vector $\vec{v} = [v_x, v_y, v_z]'$ represents the unit vector between the two user-defined points p_1 and p_2. The angle ϕ can be defined to be between $\vec{u}$ and $\vec{v}$, and is equal to $\cos^{-1} v_x$. We also define $\vec{r}$ to be $\vec{u} \times \vec{v} = [0, -v_z, v_y]'$. The first transformation T_u responsible for aligning the LV axis to $\vec{u}$ equal to the rotation of the vector $\vec{r}$ by angle ϕ and is represented mathematically by:

$$T_u = \begin{bmatrix} T_{u11} & T_{u12} & T_{u13} & 0 \\ T_{u21} & T_{u22} & T_{u23} & 0 \\ T_{u31} & T_{u32} & T_{u33} & 0 \\ 0 & 0 & 0 & 1 \end{bmatrix} \tag{3.1}$$

where

$$\begin{aligned} T_{u11} &= \cos\phi \\ T_{u12} &= -v_y \sin\phi \\ T_{u13} &= -T_{u31} = -v_z \sin\phi \\ T_{u21} &= v_y \sin\phi - v_y v_z (1 - \cos\phi) \\ T_{u22} &= \cos\phi + v_z^2 (1 - \cos\phi) \\ T_{u23} &= T_{u32} = -v_y v_z (1 - \cos\phi) \\ T_{u33} &= \cos\phi + v_y^2 (1 - \cos\phi) \end{aligned}$$

The second required transformation is responsible for the reslicing of the US volume. An equal angular spacing over 180 degrees was set to one degree. As the data is repeated from 180 to 360 degrees, it is necessary to only use slices from 0 to 180 degrees. The transformation responsible for generating the 2D angular slices at the chosen degree θ_s ($\forall\, \theta_s \in [0, 1, \ldots, 179]$) is equal to is defined by:

$$T_{\theta_s} = \begin{bmatrix} 1 & 0 & 0 & 0 \\ 0 & \cos\theta_s & -\sin\theta_s & 0 \\ 0 & \sin\theta_s & \cos\theta_s & 0 \\ 0 & 0 & 0 & 1 \end{bmatrix} \tag{3.2}$$

The final geometrical transform T_F is formed by concatenating the previously defined transforms, the first consisting of aligning the LV axis to $\vec{u}$ and the second transform that performs the angular reslicing. The origin of the reslicing operator as a column vector is defined by $P_{org} \in \mathbb{R}^3$. The rotation matrix is:

$$T_F = \begin{bmatrix} I_3 & -P_{org} \\ 0 & 1 \end{bmatrix} \times T_{\theta_s} \times T_u \times \begin{bmatrix} I_3 & P_{org} \\ 0 & 1 \end{bmatrix} \tag{3.3}$$

where I_3 is the 3×3 identity matrix.

3.2.2 Creation of initial manual contours

The 3D segmentation algorithm requires the initialization of two contours. These two endocardial contours were drawn by an expert cardiologist using in-house annotation software. The manual contours were delineated on the two orthogonal slices θ_0 and θ_{90}. Figure 3.3 displays an example of the manual contours at ED annotated by the clinician.

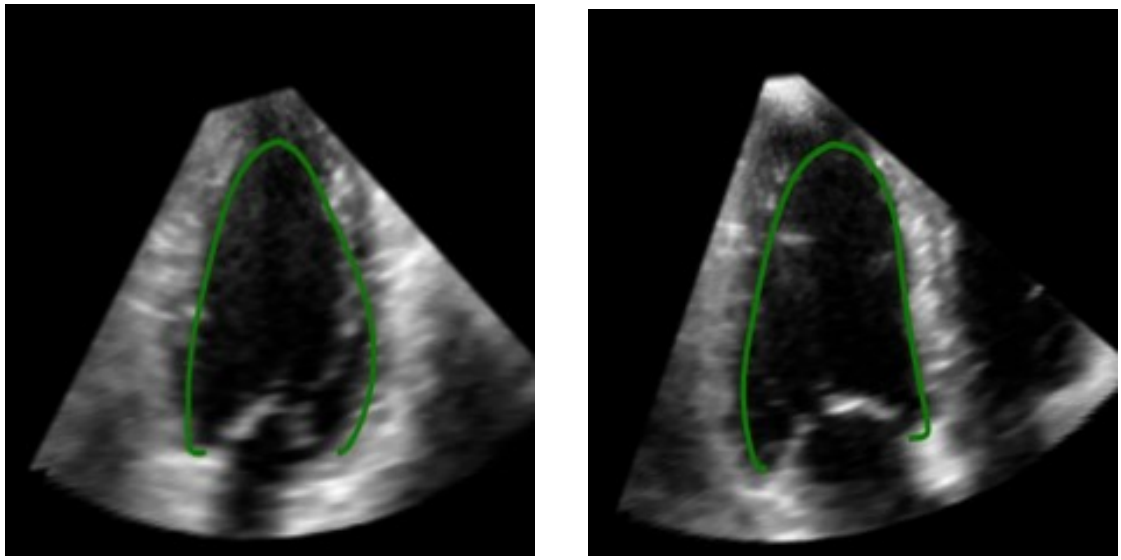

(a) Contour on the θ_0 angular slice (b) Contour on the θ_{90} angular slice

Figure 3.3: A demonstration of the two initial contours delineated on orthogonal planes by an expert clinician at the (a) θ_0 and (b) θ_{90} angular slices

A method was developed to assist the expert in delineating the endocardial contours by selecting the apex. The user can choose the apex from the 2D angular slice of their choice, and using the geometrical transformations the 3D location is automatically generated. The apex locations are then automatically visible throughout the sequence of angular slices, which assists the clinician in delineating the endocardial contours.

3.2.3 Automatic contour generation with diffeomorphic image registration

Given the contours on angular slices θ_0 and θ_{90}, the method of [76] was used to generate the automated contours at degree θ_s ($\forall\, \theta_s \in [1, 2, \ldots, 89, 91, \ldots, 179]$). The method [76] computes the point-to-point correspondences between all frames in a sequence, using a moving mesh approach as seen in Figure 3.4. The problem is described as an optimization problem where the similarity measure between two frames is defined by the squared L2 norm. The deformation field is optimized in terms of the radial and rotation components, making it an ideal approach for analyzing cardiac data. During the optimization process, these components are converted to traditional grid displacements. The original method was developed for segmentation of the LV in a temporal sequence of short-axis 2D images, given a manual contour at ED. The method was adapted for US 3D spatial registration. The method of [76] is performed across a sequence of temporal slices across a cardiac cycle, and therefore it was necessary to create the angular slice at the θ_{180} contour. This θ_{180} contour is set to be y flipped version of the angular slice at θ_0.

Figure 3.5 displays an example of a sequence of angular slices generated automatically. A subset of the slices is displayed from a total of 180 slices with an angular spacing of one degree. It can be seen that the contours (red) that are automatically generated closely follow the endocardium of the LV. The apex is displayed in green as a reference. The deformation grid produced by the algorithm is overlaid in green.

The registration process creates a sequence of automated contours as 2D points. To transform the 2D contour points to 3D, the inverse of the transformation matrix T_F in (3.3) is used. Figure 3.6 displays an example of the 3D contour points that were transformed and are now in the same US space for a patient at ED:

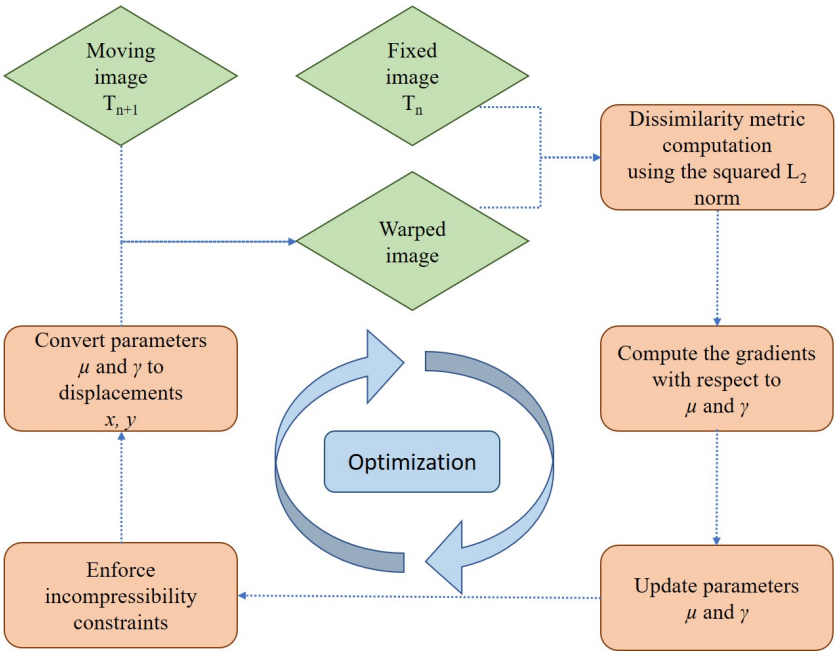

Figure 3.4: Flowchart of the 2D registration process.

3.2.4 Mesh generation

To compare the proposed segmentation method with the reference, a mesh was created from the set of the 3D contour points. There are methods available in the literature to form a mesh from a distinct set of 3D points. Algorithms include Delaunay triangulation [77] and alpha shapes [78]. These methods were deemed unsuitable as some portions of the mesh from the proposed method may be concave. A custom program was written where triangle faces were created between each pair of contours.

The input data consists of 180 contours with the angular spacing set to one degree. The method used to create the contours [76] automatically is a point-to-point correspondence method, therefore across the angular slices the points correspond with each other. The mesh faces are then created by using two adjacent points from $contour_i$, and a single corresponding point from the $contour_{i+1}$ and vice versa.

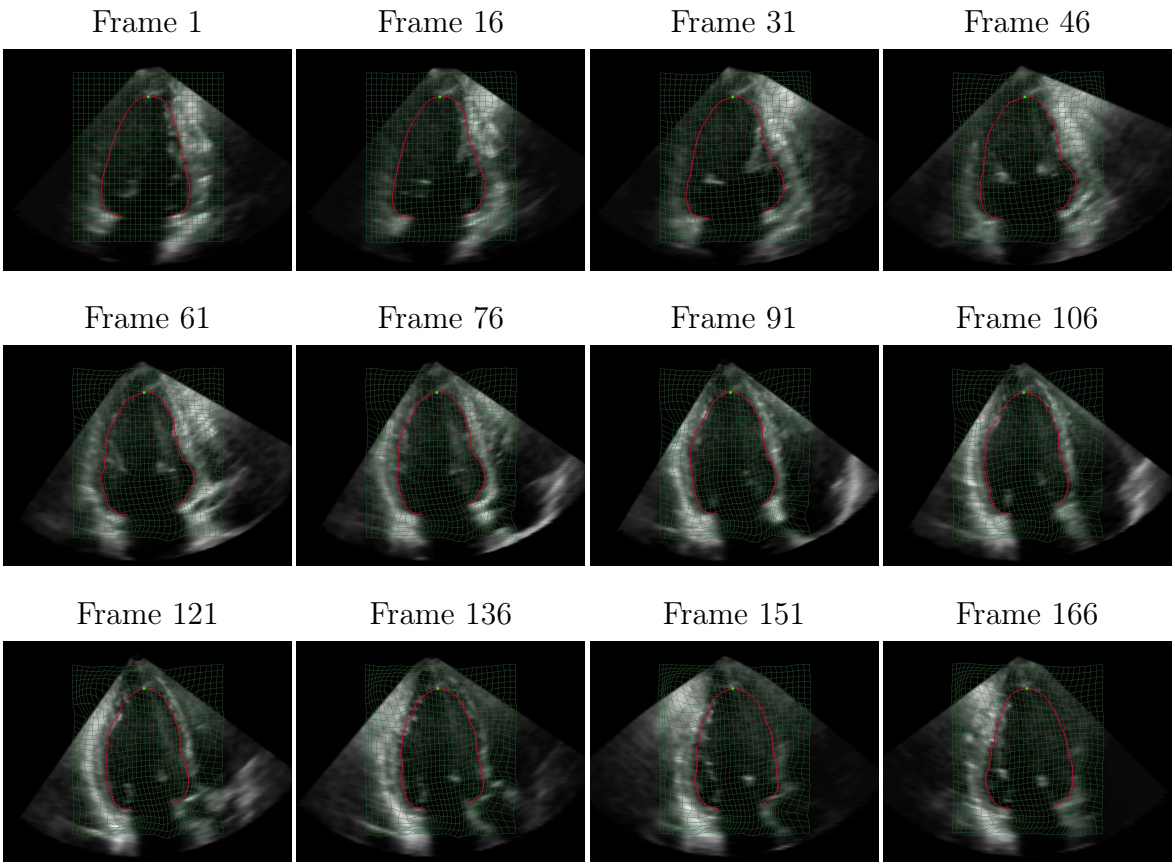

Figure 3.5: An example of a subset of the angular slices sequence every 15 degrees

3.3 Results

3.3.1 Dataset - CETUS

The dataset used to validate the proposed method consisted of 3D US data from 45 patients. This was comprised of a training set of 15 patients and two testing sets of 15 participants each. The testing datasets were made available for those approaches that required separate training and testing sets, such as for machine learning or atlas-based approaches. Since the proposed method does not rely on training data, the set of 30 testing patients was used for analysis. Patient data were acquired from three scanners from three hospitals: 1) GE Vivid E9 system with a 4V probe 2) Philips iE33 system with an X5-1 probe, and 3) Siemens SC2000 with a 4Z1c probe. The patients were divided into the following groups: 1) 15 healthy patients; 2) 15 patients that previously had a myocardial infarction (MI) (a minimum of three months after

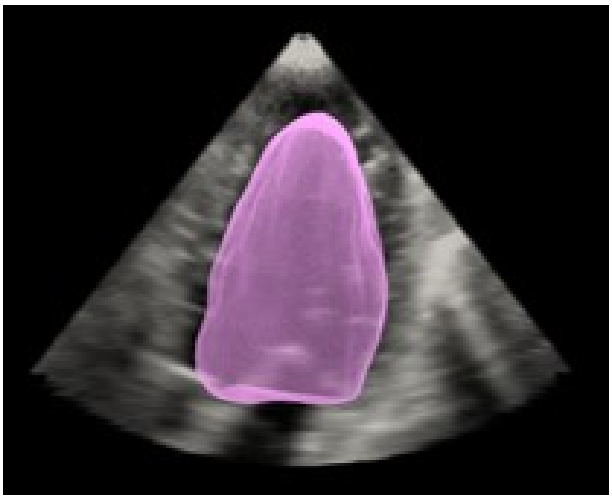

Figure 3.6: Delineation of the endocardium of the left ventricle at end-diastole using the proposed methodology.

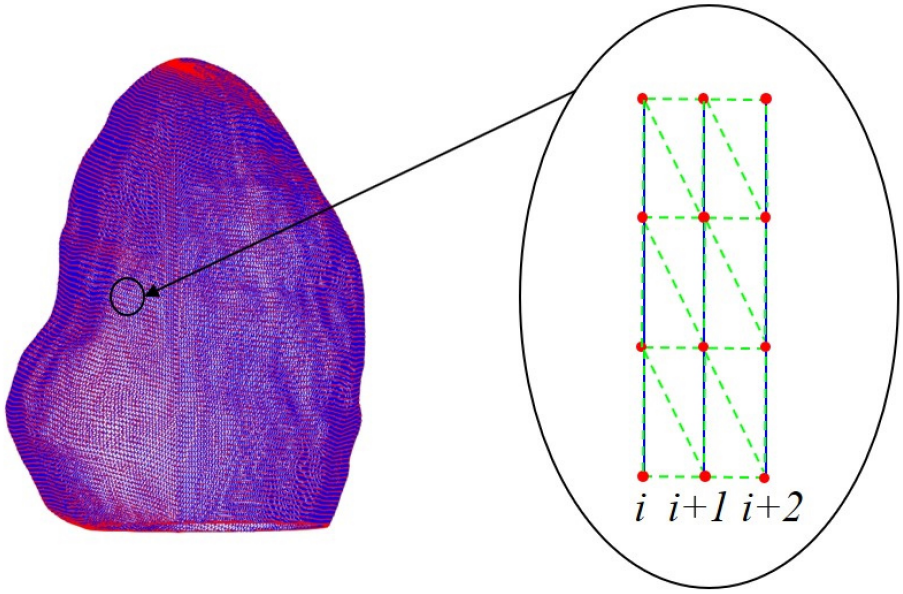

Figure 3.7: A representation of the formation of the dense mesh, where i, $i+1$, $i+2$ represent three contours.

the MI; 3) 15 patients that had dilated cardiomyopathy (DC). The information about each patient was not provided to the user.

The ground truth segmentation of the LV at ED and ES were provided by three expert cardiologists using the software package `Speqle_3D` (University of Leuven, Belgium). To keep the segmentations consistent, the cardiologists developed a set of rules to aim for consistency among the delineations. These included rules were derived for the LV wall, the mitral valve plane, and the decision to include trabeculations and papillary muscles, and the apex selection. Further information concerning the process of the manual contour creation can be found [79]. References meshes for the LV endocardium were formed once the expert cardiologists agreed upon each of the contours.

An online evaluation platform was available to compare the meshes from the proposed method to the reference meshes.[1] The distance metrics calculated included the following: mean absolute distance (d_m), Hausdorff distance (d_H), and the modified Dice score were computed. The clinical metrics available for comparison were the EDV, ESV, SV, and EF.

The proposed algorithm was compared against nine other methods that were evaluated using the same online platform [80]. The four semi-automated methods are as follows: Authors from [33] developed an interactive method based on graph cuts to perform endocardial segmentation. The user is required to select the apex, center of the LV, and the base, where then the axis between the three is used to transform the data to the spherical-cylindrical space. Graph cuts are then employed in this spherical-cylindrical space. Another set of authors [38] used the ground truth from the training data to strain a structured random forest. The 2D structured random forests were used on each short-axis slice in the 3D echocardiography volumes, creating boundary candidates that defined a surface model of the LV. This surface model was then deformed to fit the testing volumes. Another approach [51] created a

[1]The online platform is available at https://miccai.creatis.insa-lyon.fr/miccai/community/1

multi-atlas segmentation framework for endocardial border detection. Speckle noise was first decreased to improve the registration results, and the shapes were extracted from patches of the US images. Lastly, authors [44] used a model-based level set method for delineation of the endocardium, which was enhanced by the use of a multi-scale quadrature filter.

The five fully automated methods are as follows: Authors [47] developed a method for tracking the chamber in 3D+time sequences of US images. Automatic segmentation is performed at the ED frame, and tracking is performed using an optical flow-based method. Another set of authors [36] applied successive random forest classifiers. The authors included two additional classes apart from the LV and the background, which were the myocardium and the mitral valve, thereby increasing the contextual information for segmentation. Authors [35] used a cascade of Hough forests (derived from random forests) to perform both object detection and segmentation. Another set of authors [45] employed real-time tracking of the LV. A mesh model is first created, and a combination of Kalman filtering and edge detection is used for to track the mesh throughout the cardiac cycle. Lastly, [41] developed an approach using AAMs, where separate AAMs were created for the ED and ES frames.

3.3.2 Quantitative distance metrics

Mean absolute distance

The mean absolute distance (d_m) is computed by taking each point in the proposed approach mesh S, and locating the closest the point in the ground truth reference mesh R. The mean of these minimum distance values is then computed [81], where the result is given in mm:

$$d_m(S,R) = \frac{1}{N_s} \sum_{s \in S} \min_{r \in R}(dist(s,r)). \tag{3.4}$$

Hausdorff distance

The Hausdorff distance (d_H) is calculated by finding a measure of the maximum distance between the proposed mesh S and the ground truth reference mesh R [82]. The result is reported in mm. The d_H is calculated by the following equation, where the Euclidean distance used between the points:

$$d_H(S,R) = \max\left\{\sup_{s\in S}\inf_{r\in R}\mathrm{d}(s,r), \sup_{r\in R}\inf_{s\in S}\mathrm{d}(s,r)\right\}. \tag{3.5}$$

Modified Dice score

The modified Dice metric is a measure of the amount of overlap between the volume from the proposed approach V and the reference volume V_{ref}. A value of 0 indicates complete overlap and a value of 1 indicates no overlap between the two volumes [83].

$$\text{Modified Dice} = 1 - \frac{2(V \cap V_{ref})}{(V + V_{ref})}. \tag{3.6}$$

Ejection fraction (EF)

One method used to measure the efficiency of the heart at pumping blood is to report the EF. The difference between the EDV and the ESV is first calculated, and then divided by the EDV. The result is reported as a percentage.

$$\text{EF} = \frac{EDV - ESV}{EDV} \times 100\%. \tag{3.7}$$

3.3.3 Quantitative distance metrics results

Table 3.1 provides the comparison of the proposed method to four semi-automated methods and five fully automated methods [80] for ED, and Table 3.2 provides the comparison for ES. The inter-observer values among the expert cardiologists are provided in italics, while the results from the proposed method are given in bold. Standard deviation values are provided in parentheses, displayed for each metric and com-

puted from the results based on the online evaluation platform. Underlined values indicate the algorithm that gave the best performance for the particular algorithm. The proposed method was evaluated over 30 patient datasets at ED yielded the mean distance metrics as follows: (1) d_m of 2.36 mm, (2) d_H of 8.25 mm, and (3) modified Dice score of 0.113, and for ES the method yielded the following metrics: (1) d_m of 2.33 mm, (2) d_H of 8.95 mm, and (3) modified Dice score of 0.143.

Table 3.1: Distance and overlap metrics for end-diastole: The mean absolute distance d_m, Hausdorff distance d_H and modified Dice score D^* values for quantitative evaluation of the accuracy of segmentation results by semi and fully automated methods in comparison to the ground truth segmentation by experts. The lower the value of d_m, d_H or D^* the better the performance of the approach. Inter-observer values indicate differences within the ground truth segmentation by three different experts. Standard deviation values are provided in parentheses.

	End Diastole		
	d_m	d_H	D^*
Method	mean (mm)	mean (mm)	mean
Inter-observer	*1.39 (0.40)*	*4.70 (1.27)*	*0.069 (0.021)*
Our method	**2.36 (0.81)**	**8.25 (3.52)**	**0.113 (0.043)**
Semi-automated			
Bernier *et al.* [33]	2.37 (0.60)	9.41 (2.62)	0.118 (0.029)
Domingos *et al.* [38]	<u>2.09</u> (0.68)	9.31 (3.89)	<u>0.106</u> (0.038)
Oktay *et al.* [51]	2.18 (0.70)	<u>7.55</u> (1.77)	<u>0.106</u> (0.033)
Wang *et al.* [44]	2.54 (0.99)	9.04 (3.58)	0.125 (0.042)
Fully automated			
Barbosa *et al.* [47]	2.26 (0.73)	<u>8.10</u> (2.66)	<u>0.106</u> (0.041)
Keraudren *et al.* [36]	2.44 (0.95)	9.98 (3.09)	0.130 (0.048)
Milletari *et al.* [35]	<u>2.14</u> (0.68)	8.25 (3.87)	0.107 (0.031)
Smistad et al. [45]	2.62 (0.95)	8.26 (2.98)	0.115 (0.038)
van Stralen *et al.* [41]	2.44 (0.91)	8.45 (3.50)	0.121 (0.054)

Table 3.2: Distance and overlap metrics for end-systole: The mean absolute distance d_m, Hausdorff distance d_H and modified Dice score D^* values for quantitative evaluation of the accuracy of segmentation results by semi and fully automated methods in comparison to the ground truth segmentation by experts. The lower the value of d_m, d_H or D^* the better the performance of the approach. Inter-observer values indicate differences within the ground truth segmentation by three different experts. Standard deviation values are provided in parentheses.

	End Systole		
	d_m	d_H	D^*
Method	mean (mm)	mean (mm)	mean
Inter-observer	*1.34 (0.35)*	*4.70 (1.15)*	*0.080 (0.021)*
Our method	**2.33 (0.83)**	**8.95 (3.05)**	**0.143 (0.057)**
Semi-automated			
Bernier *et al.* [33]	2.64 (0.60)	9.34 (2.08)	0.163 (0.047)
Domingos *et al.* [38]	2.20 (0.72)	8.35 (2.67)	0.129 (0.050)
Oktay *et al.* [51]	2.47 (0.74)	8.57 (2.96)	0.151 (0.049)
Wang *et al.* [44]	2.68 (1.11)	9.14 (3.33)	0.159 (0.057)
Fully automated			
Barbosa *et al.* [47]	2.43 (0.91)	8.13 (3.08)	0.144 (0.057)
Keraudren *et al.* [36]	2.54 (0.75)	9.15 (3.24)	0.158 (0.057)
Milletari *et al.* [35]	2.91 (1.01)	8.53 (2.30)	0.162 (0.062)
Smistad et al. [45]	2.92 (0.93)	8.99 (2.98)	0.156 (0.050)
van Stralen *et al.* [41]	2.79 (1.24)	8.65 (2.85)	0.165 (0.079)

To perform a visual inspection of the 3D contour points, the difference between the proposed method mesh and the ground truth can be viewed in terms of the d_m. Figure 3.8 demonstrates an example of the d_m. The colors represent the distance between the ground truth and the proposed method, where blue represents high agreement (low distance values) and red represents low agreement (high distance values). It can be observed that there is high agreement and accurate delineation at the apex and the endocardial walls.

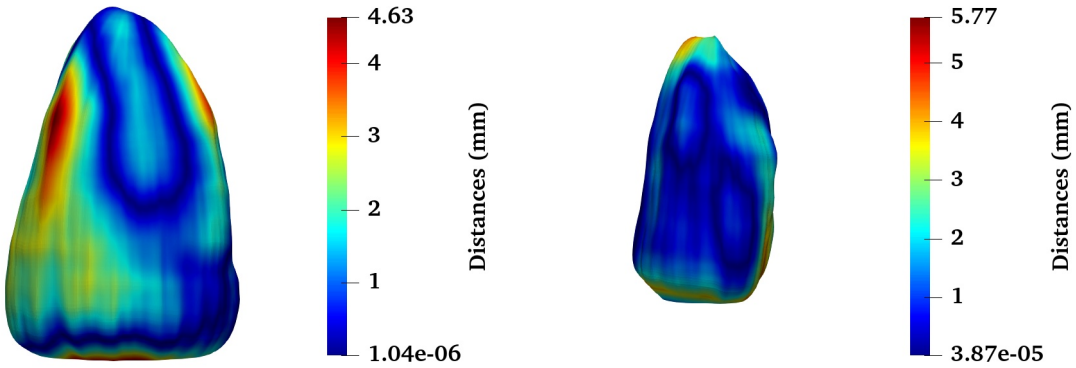

(a) d_m mesh at end diastole b) d_m mesh at end systole

Figure 3.8: Example mean absolute distance d_m meshes for a single patient at (a) end diastole and (b) end systole. Red represents the larger distance from the ground truth, and blue represents a small distance in mm.

3.3.4 Quantitative clinical metrics results

The online evaluation platform [80] for the CETUS challenge provided the computation of various clinical metrics. These included the EDV, ESV, and EF. Information was also provided concerning the (1) modified correlation coefficient, equal to 1 minus the correlation coefficient (2) the bias, equal to the mean of the differences between the reference and proposed method values. The clinical metrics for ED, ES, and the EF are given by the Tables 3.3, 3.4 and 3.5. Results from the proposed algorithm are in bold, and italicized values are the inter-observer values among the cardiologists

responsible for creating the ground truth contours. Standard deviation values are provided for each of the metrics and are given in parentheses; these values were calculated outside of the provided platform. Values that are underlined are the metrics that indicate the best performance and are provided separately for the semi-automated and fully automated algorithms. Evaluating the proposed approach across the 30 patients dataset yielded 0.83 mL for the bias of the EDV, 8.07 mL for the ESV, and -3.96% for EF.

To ease the visualization of the difference between the proposed and reference methods, Bland-Altman plots are employed. Figures 3.9 display Bland-Altman plots for the differences between the EDV, ESV, and EF values. The reference line at 0 is displayed in black, and the bias line is indicated in red. The lines showing the limits of agreement are given in blue, and are calculated using the bias $\pm$ 1.96 multiplied by the standard deviation.

3.4 Conclusion

A novel semi-automated algorithm for 3D segmentation of the LV has been developed for use in echocardiography volumes. There are many advantages to the proposed method. There is no dependency on a training dataset, which eases applying the method on patients with abnormalities. There are also no geometrical priors used to encode the shape of the chamber, and no assumptions concerning the intensity distributions of the volumes. There is minimal user interaction involved, in which the user selects an axis and delineates two manual contours. There are also multiple advantages in employing the moving mesh correspondence method [76]. The diffeomorphic method ensures that topology is preserved, resulting in realistic cardiac deformations. Limits on the amount of deformation can be specified by the user, ensuring that grid lines of the same family do not cross and that the deformations are reasonable.

Several limitations exist with the method developed. The quality of the images

Table 3.3: Clinical metrics: Agreements between EDV values computed using automated methods and ground truth segmentation by experts. The inter-observer variability values indicate the reproducibility of EDV calculated using manual segmentation.

	End Diastole		
Method	EDV corr*	EDV bias (mL)	EDV std (mL)
Inter-observer	*0.015*	*-3.0*	*11.1*
Our method	**0.059**	**0.83**	**21.6**
Semi-automated			
Bernier *et al.* [33]	0.021	2.7	13.9
Domingos *et al.* [38]	0.083	8.7	25.0
Oktay *et al.* [51]	0.055	-6.0	20.8
Wang *et al.* [44]	0.073	2.0	23.8
Fully automated			
Barbosa *et al.* [47]	0.035	-5.0	17.7
Keraudren *et al.* [36]	0.079	15.9	24.6
Milletari *et al.* [35]	0.047	5.1	19.0
Smistad *et al.* [45]	0.049	-10.1	19.4
van Stralen *et al.* [41]	0.034	-15.4	16.0

Table 3.4: Clinical metrics: Agreements between ESV values computed using automated methods and ground truth segmentation by experts. The inter-observer variability values indicate the reproducibility of ESV calculated using manual segmentation.

	End Systole		
Method	ESV corr*	ESV bias (mL)	ESV std (mL)
Inter-observer	*0.0007*	*-1.9*	*6.5*
Our method	**0.047**	**8.07**	**17.3**
Semi-automated			
Bernier *et al.* [33]	<u>0.032</u>	2.2	<u>13.7</u>
Domingos *et al.* [38]	0.044	-5.2	15.9
Oktay *et al.* [51]	0.076	<u>-0.4</u>	20.6
Wang *et al.* [44]	0.044	-3.9	16.1
Fully automated			
Barbosa *et al.* [47]	<u>0.033</u>	-6.8	<u>13.9</u>
Keraudren *et al.* [36]	0.048	<u>-6.2</u>	16.6
Milletari *et al.* [35]	0.040	-16.8	15.2
Smistad *et al.* [45]	0.036	-11.3	14.6
van Stralen *et al.* [41]	0.036	-13.2	14.4

Table 3.5: Clinical metrics: Agreements between ejection fraction values computed using automated methods and ground truth segmentation in terms of correlation and Bland-Altman analysis. The inter-observer variability values indicate the reproducibility of ejection fraction calculated using manual segmentation.

	Ejection Fraction		
Method	EF corr*	EF bias (%)	EF std (%)
Inter-observer	*0.048*	*-0.1*	*3.3*
Our method	**0.169**	**-3.96**	**6.85**
Semi-automated			
Bernier *et al.* [33]	0.189	0.1	7.8
Domingos *et al.* [38]	0.181	8.3	7.2
Oktay *et al.* [51]	0.220	-1.5	6.9
Wang *et al.* [44]	0.119	3.5	5.2
Fully automated			
Barbosa *et al.* [47]	0.111	2.9	5.2
Keraudren *et al.* [36]	0.281	12.1	10.6
Milletari *et al.* [35]	0.255	15.2	7.6
Smistad *et al.* [45]	0.121	3.7	5.2
van Stralen *et al.* [41]	0.389	3.7	8.8

can adversely affect the point correspondence mapping [76] that is used to generate the set of dense contours automatically. If necessary, preprocessing can be applied to the input volumes for denoising. A second limitation is the amount of manual interaction, which is acceptable for a single volume if compared to clinical methods such as Simpson's biplane and the modified method of discs. Applying this method to analyze a 3D volume over time for each frame would not be efficient because of the amount of manual interaction.

In order to make an accurate and informed diagnosis of the patient, it is important to have a segmentation of the left ventricle for each frame of the cardiac cycle. This leads to the development of a 3D temporal segmentation approach, as an extension of the spatial segmentation algorithm, where each frame is delineated in a semi-automated manner. This algorithm will be discussed in the following chapter.

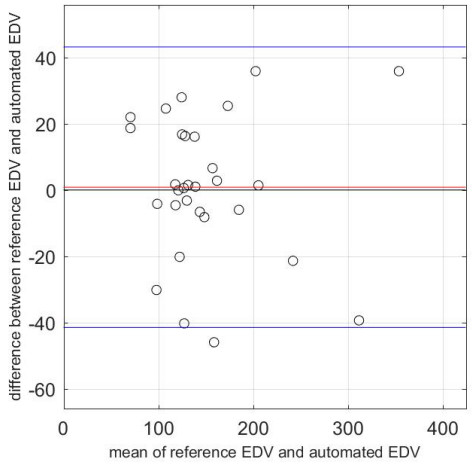

(a) EDV

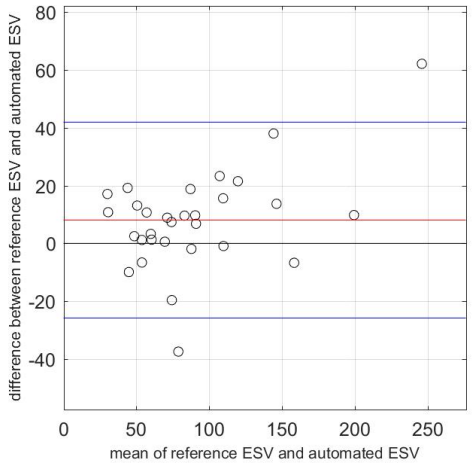

(b) ESV

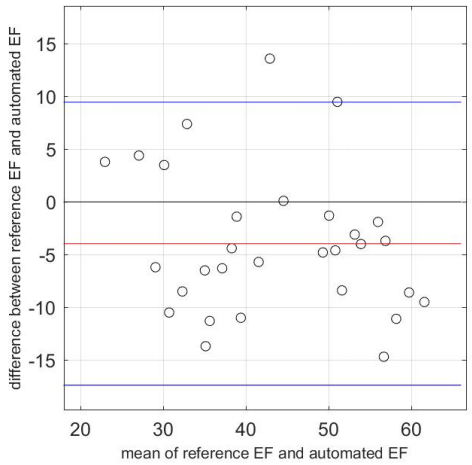

(c) EF

Figure 3.9: Bland-Altman plots comparing the proposed method to the reference segmentations for (A) End-diastolic volume (B) End-systolic volume (C) Ejection fraction

Chapter 4

3D Temporal Segmentation in US Sequences

4.1 Overview

The last chapter proposed a method for 3D spatial segmentation of the LV for the ED and ES volumes. However, clinicians often require metrics across the entire cardiac cycle to better understand the function of the heart. The ability to assess the volume and other metrics such as the strain and perform regional assessment is crucial for the clinical analysis of a patient. Therefore, the 3D spatial segmentation method was expanded to perform 3D+time segmentation across the cardiac cycle as seen in Figure 4.1. The previous 3D spatial segmentation method was used for the ED and ES volumes. A subset of these contours are obtained from the two volumes and are propagated temporally, resulting in a 3D segmentation of each frame across the cardiac cycle. The method was evaluated on 18 patients from the Mazankowski Alberta Heart Institute and compared to delineations provided by an expert cardiologist. The approach was compared to four other registration algorithms, where a set of distance, overlap, and clinical metrics was computed. Four additional experiments were performed to assess the robustness of the 3D spatial segmentation.

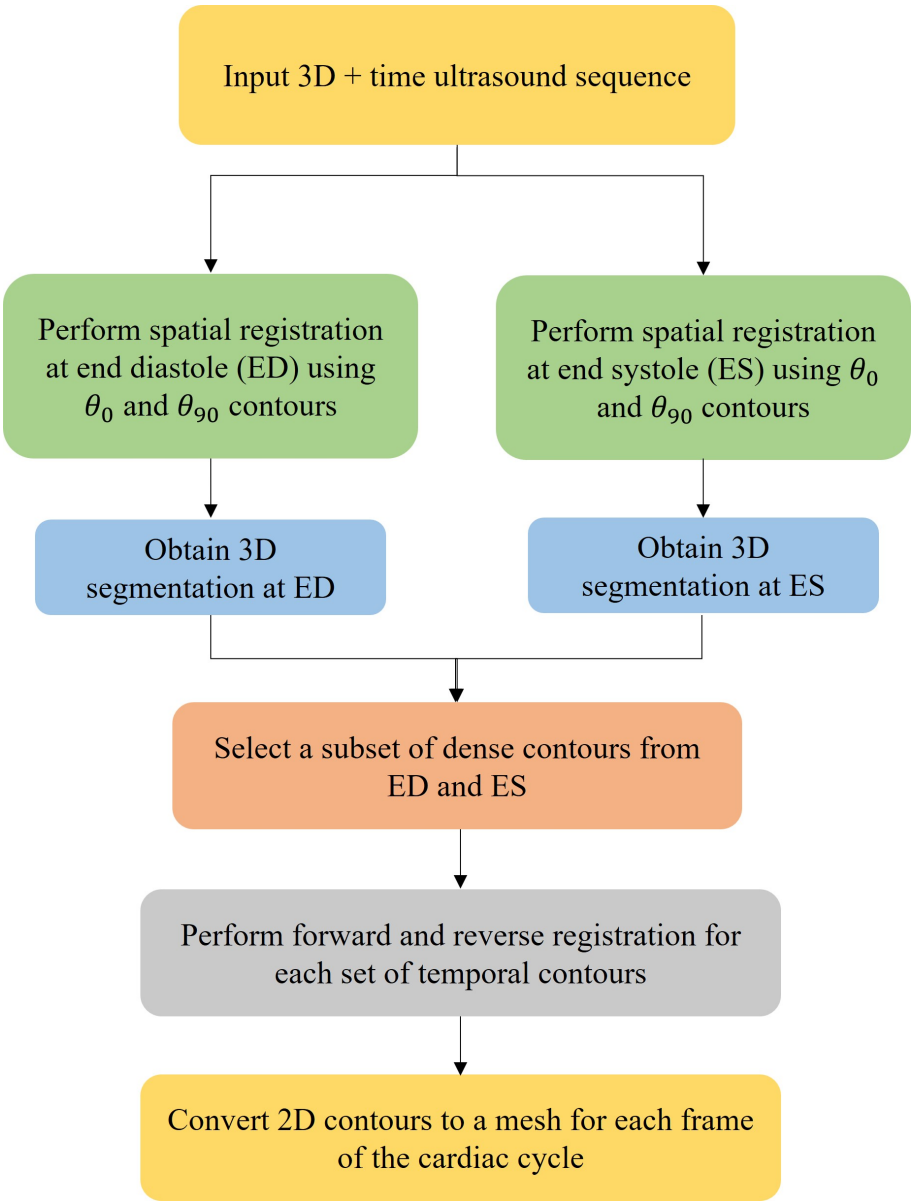

Figure 4.1: Flowchart of the 3D+time segmentation process.

4.2 Dataset

Ultrasound temporal sequences were obtained from the Mazankowski Alberta Heart Institute (Edmonton, Alberta, Canada) from $N = 18$ adult patients that were scanned to assess the function of the LV. The human research ethics committee at the University of Alberta approved the study. US scanning was performed on the patients using a Philips iE33 machine (Philips Healthcare, Best, The Netherlands) using an X5-1 transducer. To achieve a frame rate of higher than 20 volumes per second, a 3D sector angle of 70×80 degrees was used. The number of frames ranged from 17 to 39, with an average of 23.83 for a cardiac cycle. Adding the frames over the 18 patients yielded a total of 421. The dimensions of the volume were in the ranges of $160 \times 144 \times 208$ to $256 \times 176 \times 208$ voxels. The resolution of the voxels ranged from $0.608 \times 0.787 \times 0.533$ mm to $0.994 \times 1.339 \times 0.874$ mm.

An expert cardiologist provided the ground truth segmentation using the TomTec Arena software (TomTec Imaging Systems, Unterschleissheim, Germany). The clinical software uses a semi-automated approach to delineate the LV, where a speckle-tracking method is employed. The ground truth consists of a mesh at each frame of the cardiac cycle.

4.3 Algorithm

4.3.1 Temporal implementation of 3D segmentation

The first step for the temporal segmentation algorithm is to perform 3D spatial segmentation for the ED and ES frames of the cardiac cycle. The method that was previously described is used to perform the segmentation. As the method relies on manual contours to be delineated, an approach was developed to extract these θ_0 and θ_{90} contours from the ground truth created by the cardiologist. The point in the mesh with the smallest value in the z-axis was set to be the apex. The point in the center of the mesh base was extracted and set to be the second point for the axis. The axis

is then defined as the vector between the apex and the point at the center of the base. Based on this axis, the appropriate contours were extracted from the reference meshes.

Spatial registration was then performed for the ED and ES frames based on the automatically extracted contours. A subset of the contours from the ED and ES meshes are then extracted using a set angular spacing value. To obtain a segmentation for each frame of the cardiac cycle, the moving mesh method [76] is applied to each of these subsets of contours temporally. Using this method results in an anatomically plausible mesh for each frame of the cardiac cycle, consisting of contours with an angular spacing of θ_d degrees. Registration is performed in both the forward and reverse directions and weighting applied to enforce smoothing and improve temporal consistency of the contours.

4.4 Results for 3D spatial segmentation

4.4.1 Quantitative distance metrics for ED and ES

The 3D spatial segmentation was evaluated against the ground truth reference meshes using three distance and overlap metrics, the mean absolute distance d_m in mm, the Hausdorff distance d_H in mm, and the Dice score $Dice$. Results were averaged over the 18 subjects for the ED and ES frames and standard deviation values are provided in parentheses in Table 4.1. It can be observed that the metrics are more accurate for the ED frame, indicating the intrinsic problems in delineating the endocardium at ES.

4.4.2 Quantitative clinical metrics for ED and ES

Clinical measures were also calculated to compare the proposed method to the ground truth segmentation. These metrics included the EDV, ESV and EF for all subjects. Table 4.2 provides the mean difference and standard deviation for each of the mea-

Table 4.1: Quantitative evaluation results for end diastole and end systole: The mean absolute distance d_m in mm, Hausdorff distance d_H in mm, and the Dice score *Dice* for evaluation of the proposed method and the ground truth segmentation for all subjects. Standard deviation values are provided in parentheses.

End Diastole			End Systole		
d_m (mm)	d_H (mm)	*Dice*	d_m (mm)	d_H (mm)	*Dice*
0.90 (0.14)	4.24 (1.69)	0.95 (0.01)	0.97 (0.21)	4.50 (1.34)	0.91 (0.02)

sures. It can be seen that there is a slight underestimation of the volume at ED and ES, resulting in a small overestimation of the EF.

Table 4.2: Clinical metrics for end diastole, end systole and ejection fraction: The mean difference between the proposed method and ground truth segmentations. Standard deviation values are provided in parentheses.

EDV (mL)	ESV (mL)	EF (%)
4.85 (3.27)	2.11 (1.54)	-0.27 (1.22)

Bland-Altman plots [84] can be used to visually display the agreement between two sets of metrics and observe if bias exists between the measurements. Figure 4.2 displays the Bland-Altman plots for the EDV, ESV, and the EF, where each point represents a subject. A dotted black line denotes the reference line, and the bias is shown as a dotted red line. The bias represents the mean difference between the proposed measure subtracted from the reference. The limits of agreement are displayed as dotted blue lines, which are ± 1.96 * standard deviations away from the bias.

4.5 Additional experiments

Four additional experiments were performed to test the robustness of the 3D spatial segmentation algorithm, as it relies on user input. The four experiments are as follows (1) Determine the effect of varying the angular spacing on the segmentation

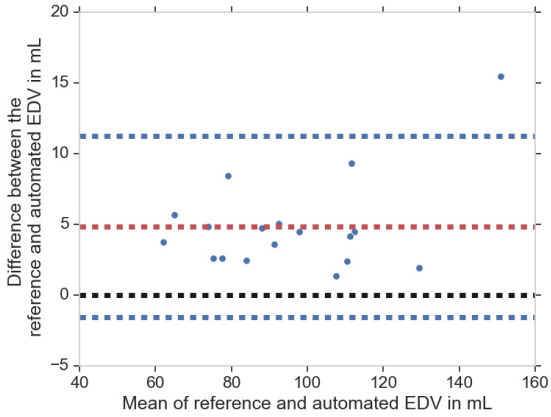

(a) EDV

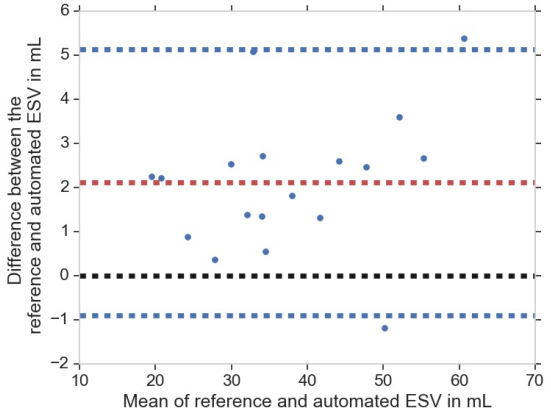

(a) ESV

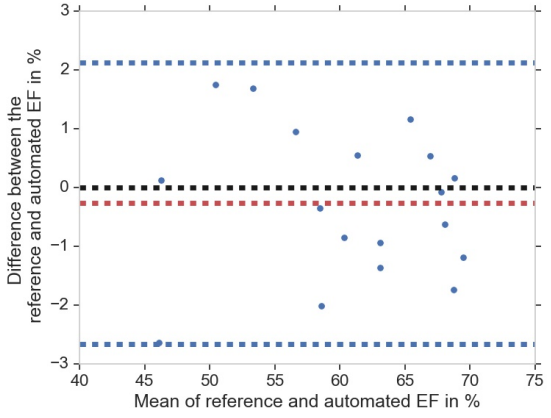

(a) EF

Figure 4.2: Bland-Altman plots for the (a) EDV (b) ESV and (c) EF. The zero reference line is displayed in black, while the bias line is shown in red. The two blue lines indicate the limits of agreement at two standard deviations away from the mean.

(2) Observe the effect of the initial axis choice on the segmentation (3) Determine the effect of the initial contours on the segmentation (4) Compare the proposed approach to a geometrical model.

4.5.1 Varying angular spacing for 3D spatial segmentation

One crucial parameter that the user sets is the angular spacing θ_d, which sets the total number of angular slices to be used for the 3D spatial segmentation for a single frame. An angular spacing of 1 degree results in 180 angular slices used for the registration process. Increasing this parameter decreases the number of angular slices, thereby creating a coarser mesh for the LV. This in turn reduces the time that is needed for the registration process.

An experiment was performed where for the ED and ES frames, the angular spacing parameter θ_d was set to values of 1, 5, 10, and 15 degrees. Table 4.3 displays the results for ED and Table displays the results for ES. Figure 4.3 displays the box plots for the d_m, d_H and $Dice$ for ED and ES at angular values of 1, 5, 10 and 15. It can be observed qualitatively that the values do not vary significantly for all three evaluation metrics for ED and ES.

The Kruskal-Wallis H test was then performed to determine if there is a statistical difference between the metrics for each of the angular spacing values. Table 4.4 gives results for the combinations of the six parameters (d_m, d_H and $Dice$ scores for each of the ED and ES volumes). The significance value was set to 0.01, and the table indicates that none of the p values obtained are smaller than 0.01. This indicates that there is no statistically significant difference between the distance and overlap metrics for any of the angular spacing values.

Table 4.3: Varying angular spacing: Comparing the end diastolic and end systolic segmentations from the proposed method to the ground truth for angular spacing values of 1, 5, 10, and 15 degrees. The following three distance and overlap metrics are used: mean absolute distance (d_m), Hausdorff distance (d_H) and the Dice score ($Dice$).

	End Diastole			End Systole		
Angular spacing	d_m (mm)	d_H (mm)	$Dice$	d_m (mm)	d_H (mm)	$Dice$
1	0.892	4.399	0.946	0.953	4.447	0.916
5	0.880	4.434	0.947	0.959	4.446	0.916
10	0.874	4.521	0.948	0.956	4.492	0.917
15	0.887	4.504	0.948	0.962	4.562	0.917

Table 4.4: Kruskal-Wallis H significance tests were formed for the end diastolic and end systolic volumes for the following three distance and overlap metrics: mean absolute distance (d_m, Hausdorff distance (d_H) and the Dice score ($Dice$).

	End-diastole		End-systole	
	Test statistic	p value	Test statistic	p value
d_m	0.305	0.959	0.014	0.999
d_H	0.029	0.999	0.019	0.999
$Dice$	0.678	0.878	0.014	0.999

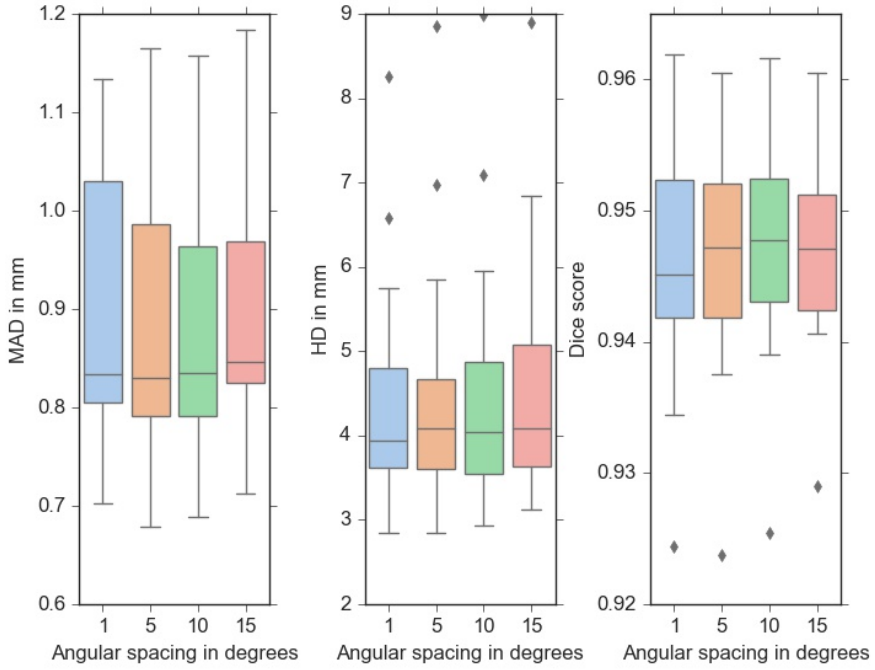

(a) End diastole

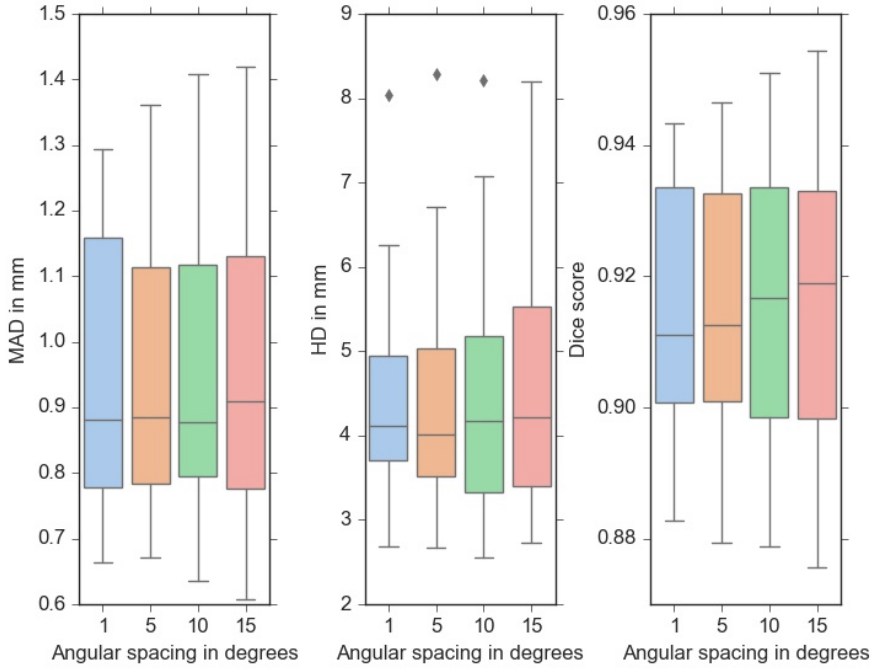

(b) End systole

Figure 4.3: Boxplots displaying the results of varying the angular spacing for 3D spatial segmentation at (a) end diastole and (b) end systole for 1, 5, 10 and 15 degrees, for the following distance and overlap metrics: d_m, d_H and $Dice$.

4.5.2 Effect of initial axis for 3D segmentation

Defining the initial axis of the LV is reliant on user interaction for the 3D spatial segmentation algorithm. The process of defining the initial axis depends heavily on the experience of the clinician, who has to take in the presence of noise or abnormalities in the patient. Therefore a robustness test was performed to determine the effect of delineating the axis. The axis was rotated about the x, y, and z axes positively and negatively by $\pi/32$ radians for both the ED and ES phases. The six meshes that resulted from this rotation for each patient were compared against the reference meshes using the following metrics: d_m, d_H, $Dice$ and volume in mL. Results are displayed in Table 4.5. Figure 4.4 displays box plots for each of the metrics for the six rotation values. It can be seen that the values are close to each other across the rotation angles.

The Kruskal-Wallis H test was also performed to determine if significant differences existed between any of the measures compared to the ground truth. Table 4.6 reports the results of the Kruskal-Wallis test for the four metrics, for the original segmentation as well as the additional six tests. With a significance value of 0.01, it can be observed that all of the measures had p values above this set alpha level. Therefore it can be concluded that for these sets of tests the segmentation of the LV is robust to the delineation of the axis.

4.5.3 Effect of initial contours

Two manual contours are required to be delineated by the user for the 3D spatial segmentation. To test the robustness of the delineation, the contours were dilated and eroded on a 2D slice by slice basis. The vectors between the center of the contour and each point were calculated and were dilated or eroded by 1 mm in the vector direction. Table 4.7 displays the results at ED and ES for the erosion and dilation

Table 4.5: Effect of initial axis: Comparing the end diastolic and end systolic segmentations from the proposed method to the ground truth for x-, x+, y-, y+, z-, and z+ rotations. The following three distance and overlap metrics are used: mean absolute distance (d_m), Hausdorff distance (d_H) and the Dice score ($Dice$), along with the volume in mL.

	End Diastole				End Systole			
Rotation	d_m (mm)	d_H (mm)	$Dice$	Volume (mL)	d_m (mm)	d_H (mm)	$Dice$	Volume (mL)
x-	0.870	4.486	0.948	94.750	0.952	4.670	0.916	37.248
x+	1.019	4.455	0.940	91.023	1.126	4.716	0.902	35.612
y-	0.924	4.347	0.945	93.945	1.029	4.552	0.912	36.443
y+	1.219	5.419	0.923	89.456	1.144	5.065	0.893	36.121
z-	0.899	4.453	0.947	93.307	0.970	4.584	0.915	36.482
z+	0.880	4.468	0.948	93.655	0.953	4.588	0.917	36.663

Table 4.6: Kruskal-Wallis H significance tests were performed for the axis delineation test using the following four metrics: mean absolute distance (d_m), Hausdorff distance (d_H) and the Dice score ($Dice$), and the volume in mL.

	End diastole		End systole	
	Test statistic	p value	Test statistic	p value
d_m	9.155	0.165	7.501	0.277
d_H	1.623	0.951	0.287	0.999
$Dice$	4.988	0.545	5.262	0.511
$volume$	1.206	0.977	0.186	0.999

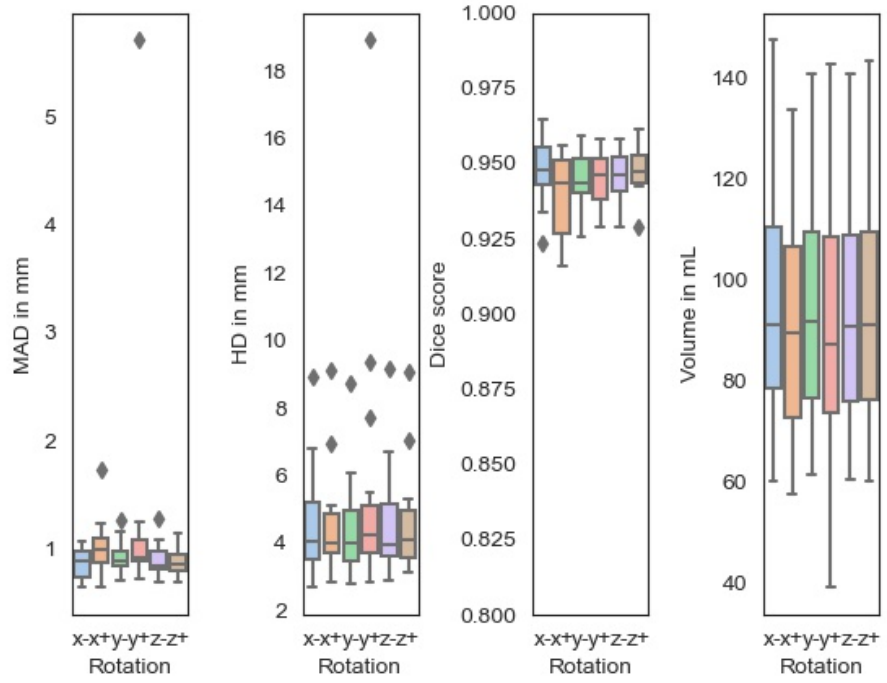

(a) End diastole

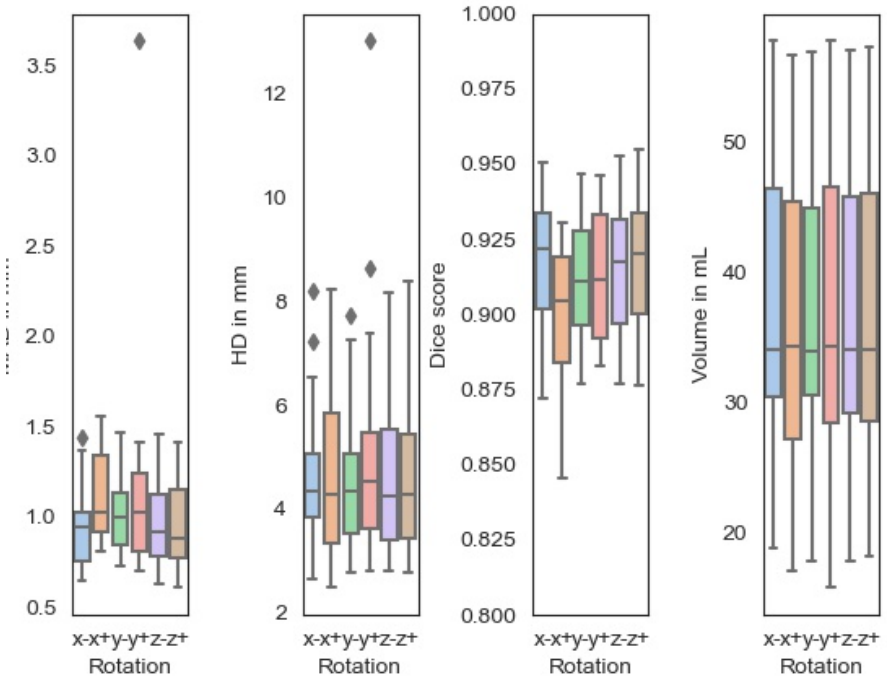

(b) End systole

Figure 4.4: Boxplots displaying the rotations in x-, x+, y-, y+, z-, and z+ directions for the following metrics: mean absolute distance (d_m, Hausdorff distance (d_H) and the Dice score ($Dice$), along with the volume in mL for (a) End diastole and (b) End systole

of the contours. Figure 4.5 displays the boxplots. Kruskal-Wallis H tests were also performed to determine the significance of the results according to the d_m, d_H, *Dice*, and *volume* metrics. It can be observed from Table 4.8 that there is a significant difference for the d_m and *Dice* metrics, but not for the d_H and the *volume* metrics.

Table 4.7: Effect of initial contour: Comparing the end diastolic and end systolic segmentations from the proposed method to the ground truth for dilation and erosion of the initial contour. The following three distance and overlap metrics are used: mean absolute distance (d_m), Hausdorff distance (d_H) and the Dice score (*Dice*) along with the volume in mL.

	End Diastole				End Systole			
	d_m (mm)	d_H (mm)	*Dice*	Volume (mL)	d_m (mm)	d_H (mm)	*Dice*	Volume (mL)
Dilate	0.888	4.616	0.945	101.631	0.945	4.603	0.916	40.566
Erode	1.252	5.006	0.925	86.202	1.277	5.089	0.890	33.187

Table 4.8: Kruskal-Wallis H significance tests were performed for the initial contours tests. Four metrics were used for the comparison, the mean absolute distance (d_m), Hausdorff distance (d_H) and the Dice score (*Dice*), as well as the computation of the volume in mL.

	End diastole		End systole	
	Test statistic	p value	Test statistic	p value
d_m	27.734	p<0.001	16.803	p<0.001
d_H	5.679	0.058	1.467	0.48
Dice	27.179	p<0.001	13.276	p<0.001
volume	3.762	0.152	3.362	0.186

Figure 4.6 displays an example of the dilated and eroded contours for a patient. The original contours are displayed in green, while the dilated contours are shown in red, and the eroded contours in yellow. Examples are shown for the four cases of ED at θ_{00} and θ_{90} degrees, and for ES at θ_0 and θ_{90}.

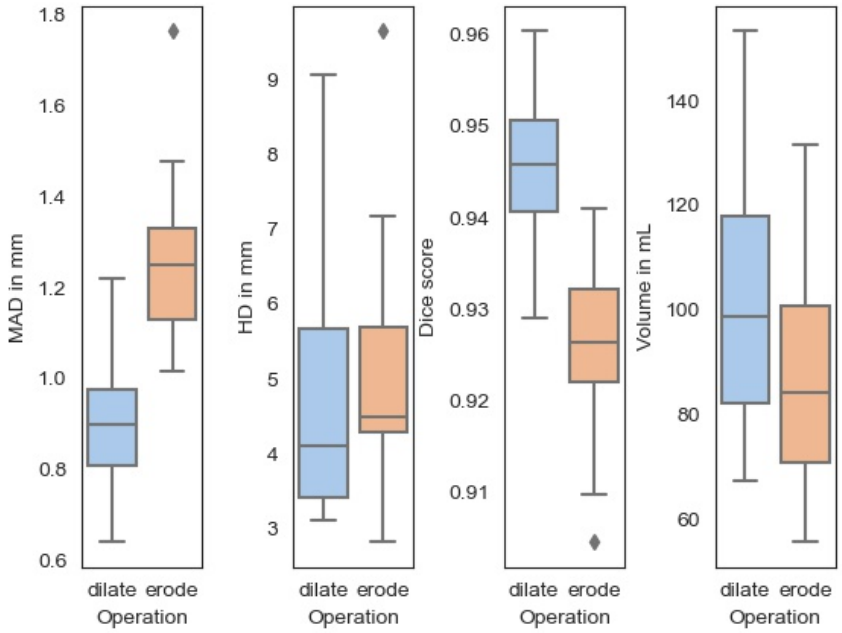

(a) End diastole

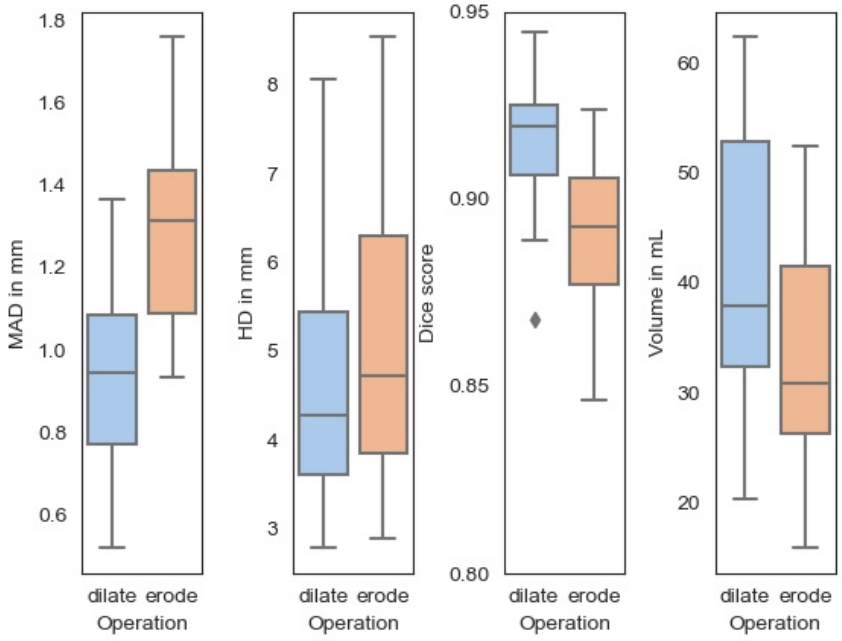

(b) End systole

Figure 4.5: Boxplots displaying the operations dilate and erode for the following metrics: mean absolute distance (d_m, Hausdorff distance (d_H) and the Dice score ($Dice$), along with the volume in mL for (a) End diastole and (b) End systole

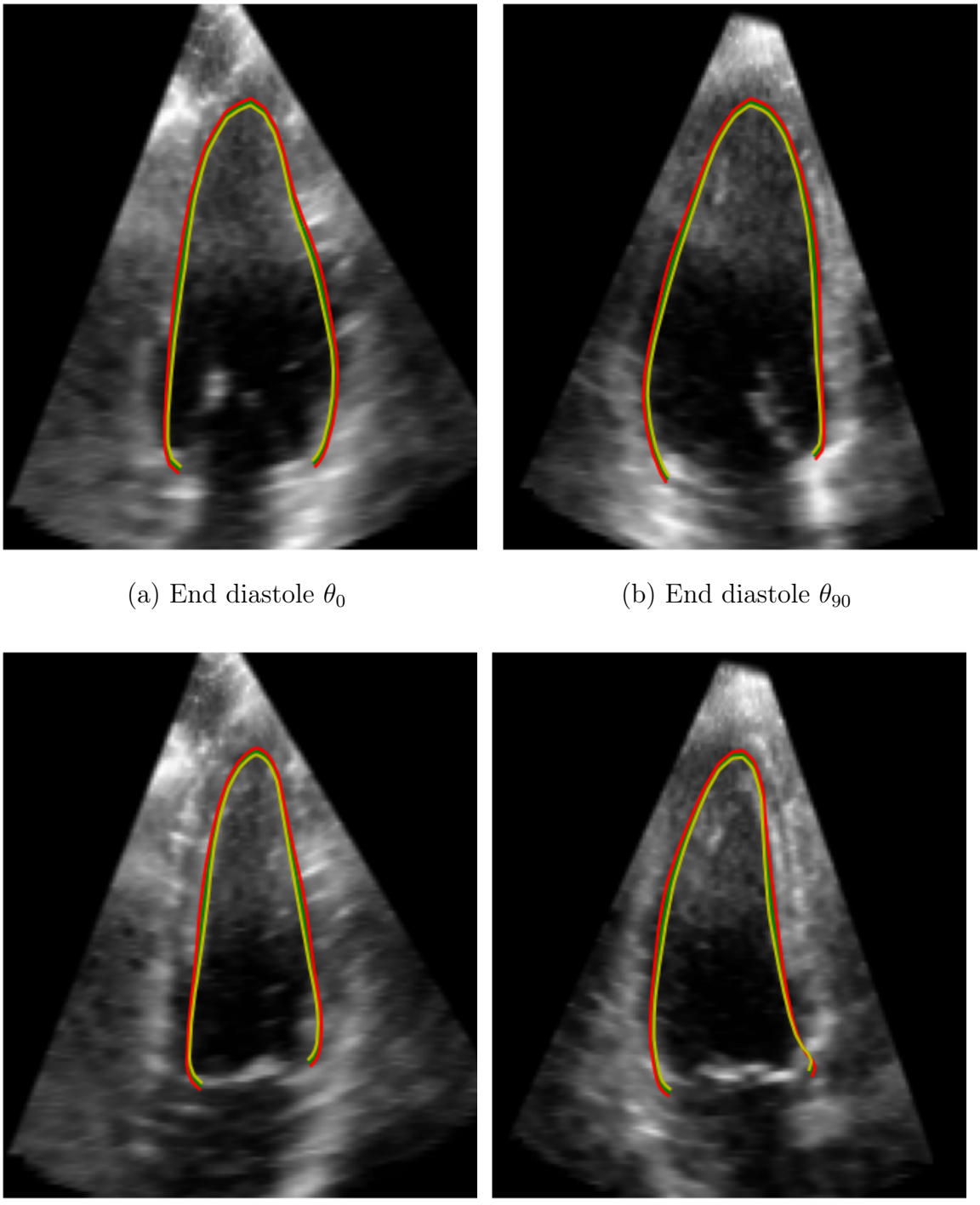

(a) End diastole θ_0

(b) End diastole θ_{90}

(c) End systole θ_0

(d) End systole θ_{90}

Figure 4.6: Figures displaying the an example of the original contour in green, dilated contour in red and eroded contour in yellow for four cases: (a) End diastole θ_0 (b) End diastole θ_{90} (c) End systole θ_0 (d) End systole θ_{90}

4.5.4 Comparison to a geometrical model

There exist several segmentation methods that require an ellipsoid as a geometrical prior for the shape of the LV. For example, authors in [47, 49, 60] use either a truncated ellipsoid model to represent the LV, or a full ellipsoid that is scaled and initialized manually within the cavity of the chamber. An experiment was designed to determine if an ellipsoidal model could produce results close to the ground truth. The following steps were taken to create the ellipsoidal model:

1. Set the z-axis direction of the ellipsoid to be the axis used for the 3D spatial segmentation centered at the base point of the mesh

2. Set the x and y axes directions to the normals used for the θ_0 and θ_{90} contours and set the sizes to be the distance between the opposing sides of the θ_0 and θ_{90} contours

3. Use VTK to cut the ellipsoid at the maximum z value of the θ_0 and θ_{90}

4. Use VTK to convert the cut ellipsoid to a mesh

Table 4.9 displays the results at ED and ES comparing the ground truth to the fitting of an ellipsoid. The four metrics used are the d_m, d_H, $Dice$ score and the volume in mL. Figure 4.7 displays the boxplots for these four measures. Kruskal-Wallis H significance tests were performed for the ED and ES meshes as shown in Table 4.10. The table shows that for all measures except for the volume there is a significant difference between the ellipsoid model and the ground truth.

Figure 4.8 displays an example of the truncated ellipsoid that has been fit to the two 0 degree and 90 degree contours.

Table 4.9: Effect of fitting an ellipsoid: Comparing the end diastolic and end systolic segmentations from the proposed method to the ground truth for angular spacing values of 1, 5, 10, and 15 degrees. The following three distance and overlap metrics are used: mean absolute distance (d_m), Hausdorff distance (d_H) and the Dice score ($Dice$).

End Diastole				End Systole			
d_m (mm)	d_H (mm)	$Dice$	volume in mL	d_m (mm)	d_H (mm)	$Dice$	volume in mL
2.019	7.148	0.862	96.406	2.244	8.586	0.788	48.227

Table 4.10: To determine if there were significant differences between the ellipsoid model and the ground truth, Kruskal-Wallis H significance tests were performed for the following metrics: mean absolute distance (d_m, Hausdorff distance (d_H) and the Dice score ($Dice$), as well as the computation of the *volume*

	End diastole		End systole	
	Test statistic	p value	Test statistic	p value
d_m	26.27	p<0.001	25.947	p<0.001
d_H	18.515	p<0.001	21.926	p<0.001
$Dice$	26.27	p<0.001	26.27	p<0.001
volume	0.256	0.613	5.334	0.021

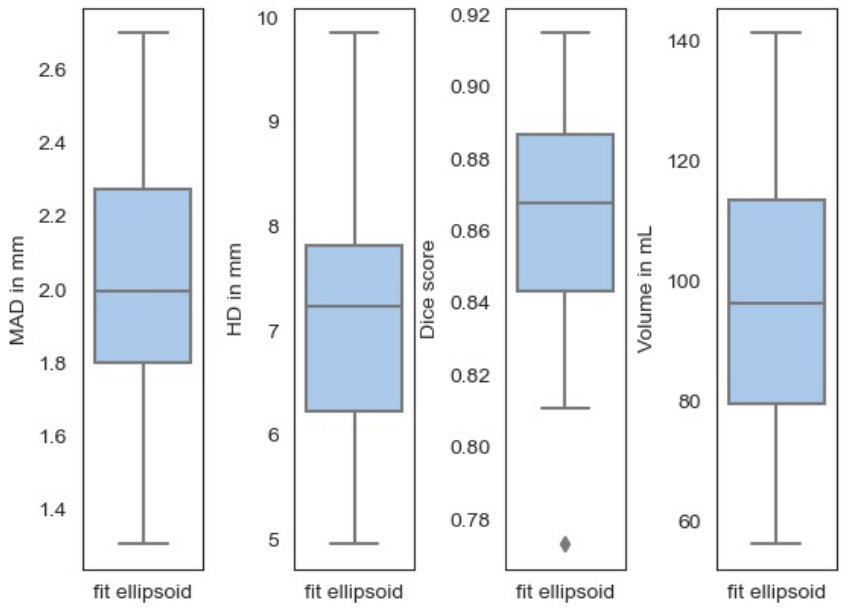

(a) End diastole

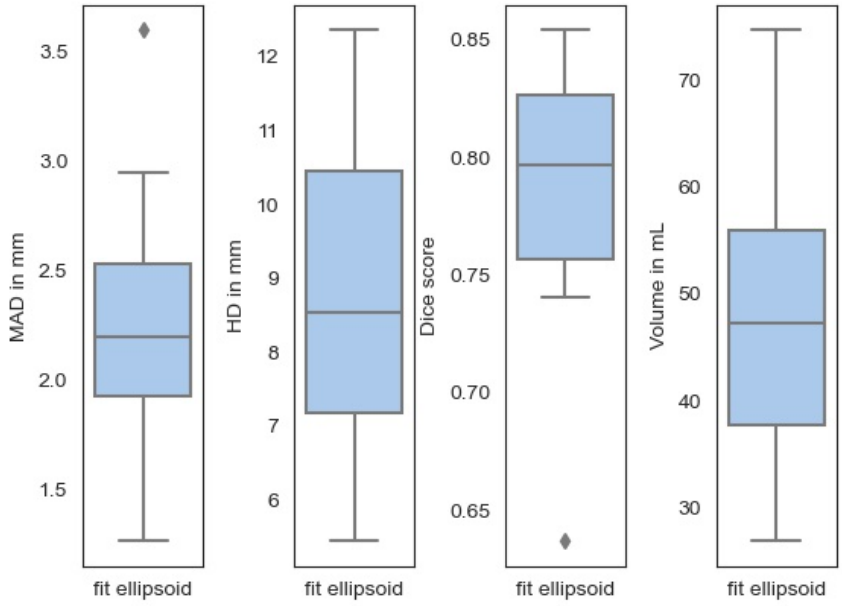

(b) End systole

Figure 4.7: Boxplots displaying the fit ellipsoid results for the following metrics: mean absolute distance (d_m, Hausdorff distance (d_H) and the Dice score ($Dice$), along with the volume in mL for (a) End diastole and (b) End systole

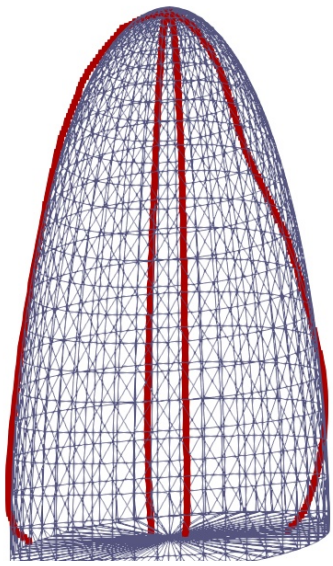

Figure 4.8: Example of fitting a truncated ellipsoid to the 0 degree and 90 degree contours.

4.6 Results for 3D+t temporal segmentation

4.6.1 Quantitative performance evaluation against other registration methods

The proposed algorithm for 3D+time segmentation was compared to four publicly available registration algorithms, two variants of the Demons algorithm from Insight Toolkit (ITK) [85], optical flow from the scikit-image package [86–89], and the optical flow implementation from the OpenCV package [90, 91]. The ITK package includes multiple implementations of the Demons algorithm, including the classical algorithm and an alternative that includes fast symmetric forces. The Demons algorithms are a set of methods that are based on optical flow [92, 93]. The main assumption is that the intensity of the two images being compared is constant in optical flow. The velocity can be considered to be the displacement between these two frames. When solving for the displacement for each voxel, the flow might be unstable when the gradient is small. Therefore the demons implementation allows the vector field to be more stable and applies smoothing to the deformation field. To increase the similarity between

the two images before registration, histogram matching was applied for both Demons registration implementations. Fifty iterations were used for the classical approach, and 200 iterations were used for the fast symmetric forces method. A Gaussian kernel with a value of 5.0 was used as the standard deviation of both implements to smooth the displacement field.

The optical flow registration algorithm from scikit-image [86–89] uses a total variation approach using the L1 norm. Unlike the traditional optical flow, this allows for the preservation of discontinuities. An image pyramid approach is used in a coarse to fine manner to account for large disparities between the images to be registered. The optical method from the OpenCV implementation uses a method based on polynomial expansion to compute the optical flow [90, 91]. Windows or neighborhoods surrounding each pixel are computed by using a quadratic polynomial. Using the polynomial expansion transform allows for the optical flow displacements to be estimated by observing how the polynomial transforms under translation.

Results of the proposed 3D+t segmentation method are displayed in Table 4.11 for the following distance metrics: the mean absolute distance d_m in mm, Hausdorff distance d_H in mm, the Dice score $Dice$, and the correlation coefficient of the volumes compared to the ground truth. It can be observed that compared to the four other registration methods, the proposed method displays high performance, with a mean d_m of 1.01 mm, mean d_H of 4.41 mm, and a mean Dice score of 0.93.

4.6.2 Visual inspection

One method to visually assess the accuracy of the proposed segmentation method is to compare the ground truth mesh to the reference mesh. Figure 4.9 displays four of these meshes, where the d_m is used. The four meshes displayed are examples of the (a) ED frame, (b) ES frame, (c) a frame in the systolic phase, and (d) a frame in the diastolic phase. The ground truth mesh is displayed in gray, while the mesh from

Table 4.11: The proposed 3D+t segmentation method was compared to four publicly available registration methods in terms of the following distance, overlap and clinical metrics: the mean absolute distance d_m in mm, Hausdorff distance d_H in mm, the Dice score *Dice*, and the correlation coefficient of the volumes in mL compared to the ground truth. The average time required for the registration between a pair of frames is also provided. The metrics reported are averaged over all subjects over the full cardiac cycle. The standard deviation values are provided in parentheses.

	d_m (mm)	d_H (mm)	*Dice*	Corrcoef	time (seconds)
Proposed method	1.01 (0.21)	4.41 (1.43)	0.93 (0.02)	0.993	0.124
ITK Demons	1.45 (0.49)	6.23 (1.48)	0.89 (0.04)	0.969	0.452
ITK Demons fsf	1.58 (0.53)	5.95 (1.70)	0.89 (0.03)	0.972	1.921
OpenCV optical flow	1.68 (0.52)	6.22 (1.48)	0.87 (0.04)	0.975	0.021
Scikit image optical flow	1.60 (0.52)	6.22 (1.48)	0.88 (0.03)	0.972	0.403

the proposed method is displayed using a heat map, where closer to blue indicates a smaller distance between the ground truth and the proposed method, and closer to red indicates a larger difference. For ease of comparison, the color bars are set to the same range. It can be seen that there is a large degree of overlap in the meshes, except perhaps towards the base where the difference is larger. This may be due to the difficulty of performing registration closer to the mitral valves.

Volume curves can also be examined to observe the differences between the ground truth obtained from TomTec Arena and the proposed method. Figure 4.10 shows two example of volume curves, where the green line represents the ground truth and the red line represents the volume from the proposed method. It can be seen that the proposed method yields volume curves that are in high agreement with the ground truth.

4.7 Conclusion

An algorithm for semi-automated segmentation of the LV in temporal US sequences has been proposed. There are several advantages of the proposed method, namely

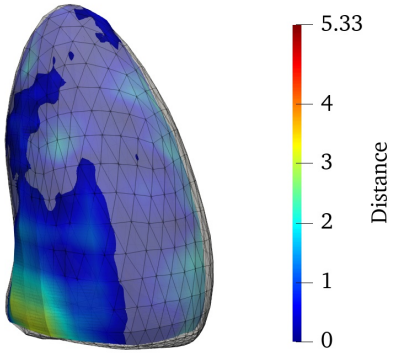

(a) End diastolic mesh

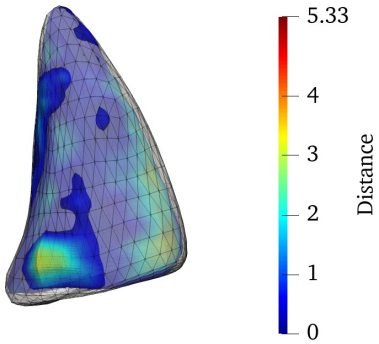

(b) End systolic mesh

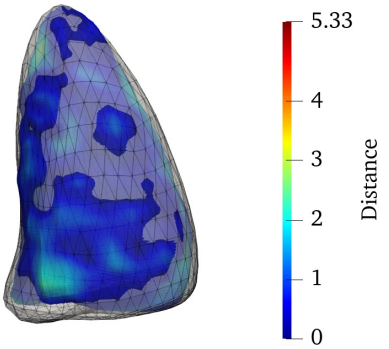

(c) Mesh in systolic phase

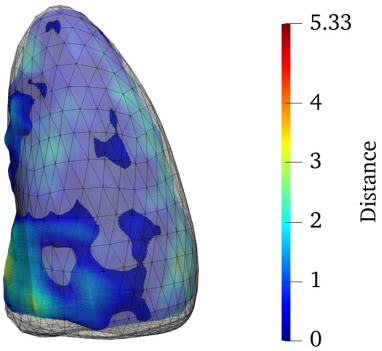

(d) Mesh in diastolic phase

Figure 4.9: Comparison of the ground truth mesh in gray and the proposed method by use of the d_m metric for four cases: (a) end diastole (b) end systole (c) in the systolic phase (d) in the diastolic phase. The color bars indicate the distance from the ground truth in mm, where blue indicates a small difference and red indicates a larger difference.

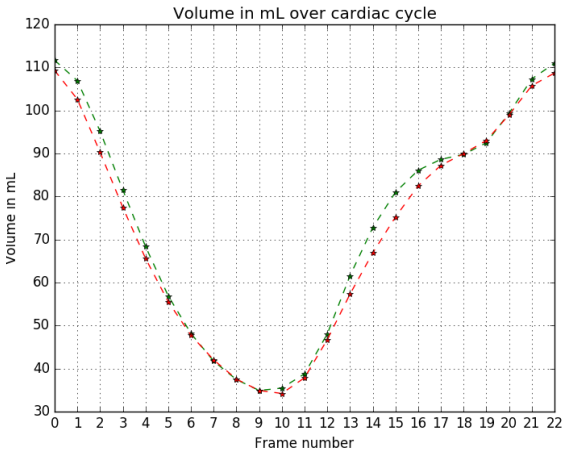

(a) Volume curve example

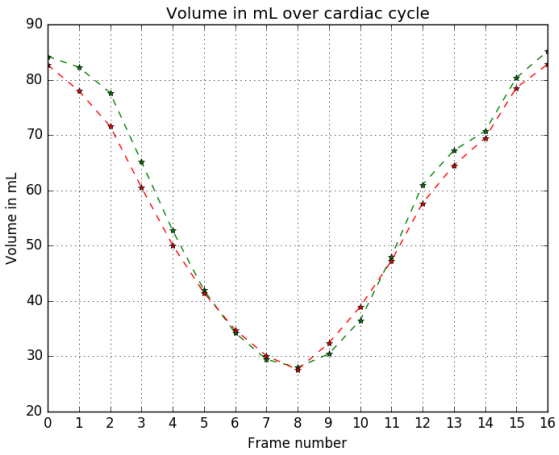

(b) Volume curve example

Figure 4.10: Volume curve representation of two example patients. The green line represents the ground truth obtained from the clinical software TomTec Arena and the red line represents the volumes obtained from the proposed method. The volume is provided in mL. Results demonstrate high agreement with the ground truth.

the use of the diffeomorphic registration approach [76] for performing the spatial and temporal registration. The use of the diffeomorphic algorithm ensures that true cardiac motion can be represented. Another advantage of the proposed method is that a geometrical prior was not assumed for the shape of the LV, allowing for the ability to capture motion from a wide variety of patients.

Several limitations exist with the proposed method, concerning the data, the semi-automated nature of the algorithm, and the experiments conducted. The quality of the US volumes may have an adverse effect on the diffeomorphic registration method [76]. Preprocessing of the data, such as speckle noise removal may improve the accuracy of the registration. The proposed algorithm was evaluated on a relatively small sample size of 18 patients, and all patients were scanned using the same US machine with a frame rate greater than 17 frames per cardiac cycle. These may restrict the use of the proposed algorithm to a larger patient population.

Limitations also exist because of the semi-automated nature of the algorithm. First, the additional experiments testing robustness to the manual interaction, showed that the proposed algorithm was not robust for the initial contour selection (using the

mean absolute distance and Dice score). Future work would include an automated method of selecting the contours. Secondly, the proposed method relies on the ground truth to extract the four contours required for the ED and ES volumes. This bias reduces the error when compared to the ground truth. Another potential drawback of the algorithm is that the manual interaction is similar to other clinical programs such as TomTec Arena. In the TomTec Arena software, the user is required to align the LV and edit the 2, 3, and 4 chamber views for the ED and ES contours. This is similar but slightly higher than the amount of user interaction for the proposed method.

There are several limitations concerning the experiments performed for testing the robustness of the 3D spatial registration algorithm. We were unable to compare our method to Simpson's biplane method, which also requires two orthogonal contours. In Simpson's biplane method, a series of discs are automatically created from the apex to the base, where an ellipsoid is fit to each of the discs. The sum of the volume of each of these discs is then computed. The actual algorithm from Philips QLab Cardiac Analysis (Philips, Amsterdam, Netherlands) was unable to be compared to, as the software is proprietary. Unfortunately, the software is unable to save out a mesh representation of the LV across the cardiac cycle, which is a vital part of the comparison of the proposed approach. One other limitation to consider is that the 3D spatial registration may not capture significant changes in the structure and shape. Using a small angular spacing value ensures that this rarely occurs.

A modified version of the 3D+time segmentation algorithm was developed for the LV. A subset of the angular contours was propagated over time for temporal registration in the proposed approach, relying on the ED and ES spatial segmentation. In the slightly modified version, only the four θ_0 and θ_{90} contours from the ED and ES frames are propagated temporally, followed by individual 3D spatial segmentation for each frame. Results using the modified method were: d_m of 1.01 (0.22), d_H of 4.59 (1.37) and a *Dice* score of 0.93 (0.02). These results were very close to the results

from the proposed method.

The proposed algorithm uses 2D spatial and temporal registration in order to capture the motion of the left ventricle over the cardiac cycle. The 2D contours that arise from the registration are transformed to 3D, yielding a pseudo-3D registration method. Instead, it may be beneficial to directly capture the 3D motion of the chamber over time. This would also reduce the need for using only a subset of the spatial contours that are propagated temporally. Instead, one could propagate an entire 3D mesh over the full cardiac cycle. This algorithm for 3D-to-3D registration will be discussed in the following chapter.

Chapter 5

3D-to-3D Diffeomorphic Registration Algorithm

5.1 Overview

The previous methods described are not able to consider the point-to-point correspondence in the through-plane direction as they rely on 2D image registration. Therefore, we propose a novel 3D-to-3D registration algorithm to assess the point-to-point correspondence within the 3D spatial domain. We apply the proposed algorithm to perform segmentation of the LV over a temporal sequence of 3D volumes. The proposed registration method is diffeomorphic and computes a voxel-to-voxel correspondence, where the deformation field is parameterized by a radial component and three curl components. The advantage of using this representation of the deformation field is that it is appropriate for capturing cardiac deformation. The algorithm allows the user to enforce diffeomorphic constraints to control the amount of allowable deformation.

Although the method is intended for the segmentation of the LV from US sequences, an evaluation using MRI sequences is included to demonstrate its robustness. The registration algorithm was tested on two datasets, 521 temporal frames from 20 patients from the Automated Cardiac Diagnosis Challenge (ACDC) MRI dataset and 213 frames from 10 patients scanned using US from the Mazankowski Alberta Heart Institute. The method was compared against six registration methods, from the Dipy package Symmetric Normalization algorithm, from ITK two versions of the demons

algorithm (classical and fast symmetric forces), two versions of optical flow from RealTiTracker, and the Elastix software package. The algorithm was able to achieve a Dice score of 98.15 (0.90)% for the MRI dataset and 93.02 (2.32)% for the US dataset. An experiment was also performed in order to test the effect of the diffeomorphic constraints. The high performance of the algorithm is demonstrated on the ability to perform well on multiple imaging modalities and patients with various abnormalities.

5.2 Algorithm

5.2.1 Theoretical overview

Figure 5.1 displays an overview of the 3D-to-3D registration process.

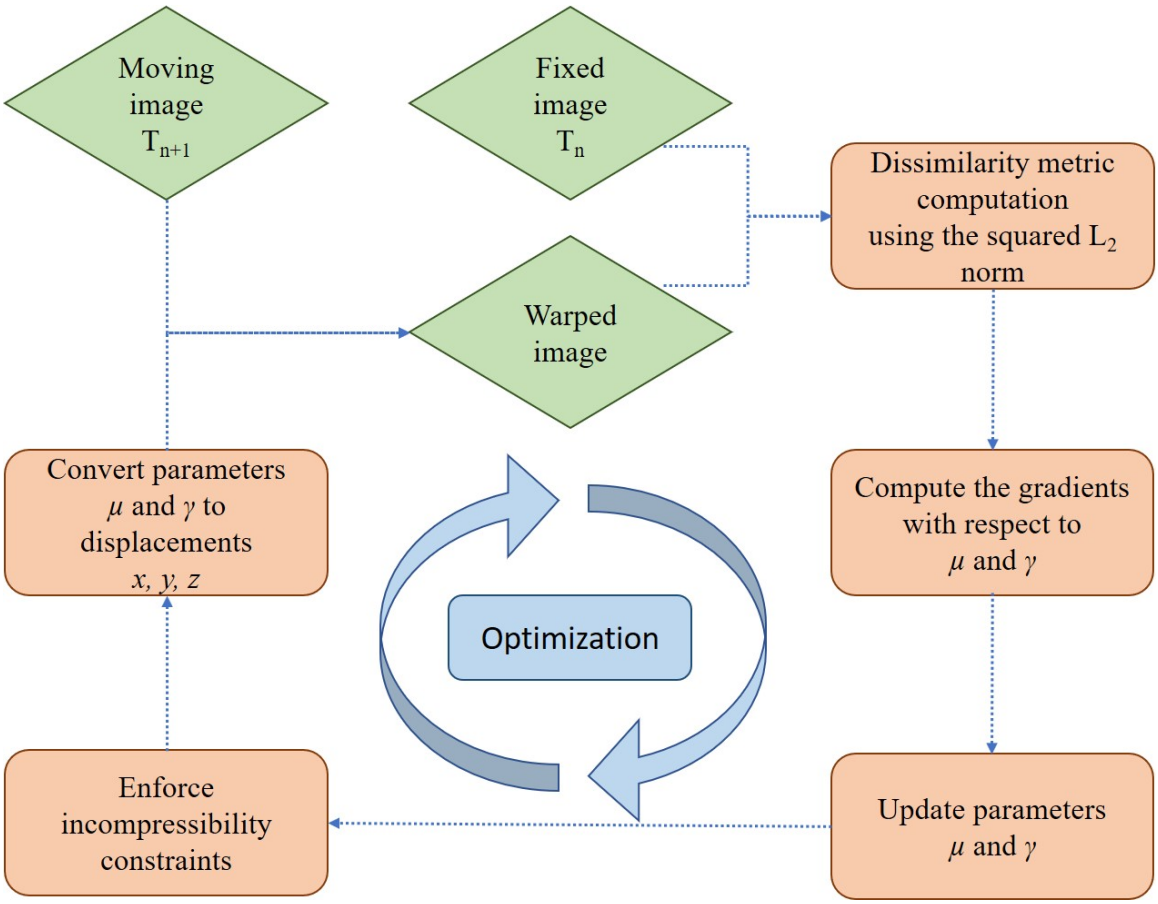

Figure 5.1: Flowchart for the proposed 3D-to-3D diffeomorphic registration algorithm

The proposed diffeomorphic registration algorithm consists of three major com-

ponents, 1) 3D moving mesh grid generation [94], 2) the similarity metric, and 3) optimization procedure. The proposed method computes the voxel-to-voxel correspondences for a temporal series of volumes, starting with nth image T_n to the T_{n+1} image defined over $\Omega \subset \mathbb{R}^3$. The goal of the registration problem is to perform optimization over a similarity measure [95], where for the proposed method the measure is defined as the squared L_2 norm:

$$\hat{\phi} = \arg\min_{\phi} E_s(T_n, T_{n+1}, \phi(\xi)), \tag{5.1}$$

where $\phi : \Omega \rightarrow \Omega$ represents the transformation function and $\xi \in \Omega$ represents the voxel locations. As a unique solution does not exist for this problem and therefore requires more constraints, as the goal is to find a permissable deformation field. The deformation field is defined using a monitor function μ and the curl of end velocity field γ. We define a continuous monitor function $\mu(\xi)$:

$$\int \mu = |\Omega|. \tag{5.2}$$

The goal of the registration process is to solve for a transformation $\phi : \Omega \rightarrow \Omega$ and $\partial\Omega \rightarrow \partial\Omega$ so that:

$$J_\phi = \mu(\xi). \tag{5.3}$$

where J_ϕ is the Jacobian determinant of the transformation ϕ.

The following steps are then taken in order to compute the transformation ϕ:

A vector field $\rho(\xi)$ is computed:

$$div\ \rho(\xi) = \mu(\xi) - 1. \tag{5.4}$$

A velocity vector field is then generated from $\rho(\xi)$, where t is [0,1] and is artificially introduced time:

$$\nu(t) = \frac{\rho(\xi)}{t + (1-t)\mu(\xi)}. \tag{5.5}$$

To solve for the transformation ϕ, the following ordinary differential equation is solved, where t is [0,1] and $\psi(\xi,\text{t}=0) = \xi$:

$$\frac{\psi(\xi,t)}{dt} = \nu_t(\psi(\xi,t)). \tag{5.6}$$

Setting ϕ equal to ψ evaluated when t=1 results in $\phi(\xi) = \psi(\xi, t = 1)$

The problem formulated above may have multiple solutions. Therefore, a constraint is added to the curl of the vector field $\rho(\xi)$. Using a Dirichlet boundary condition, an intermediate vector field $\rho(\xi)$ can be solved for from the div-curl system. This formulation ensures a unique solution.

$$\begin{cases} \nabla \cdot \rho(\xi) = \mu(\xi) - 1 \\ \nabla \times \rho(\xi) = \gamma(\xi). \end{cases} \tag{5.7}$$

The registration problem can be parameterized in the following manner as a constrained optimization problem, where user inputs τ_{ub} is the upper bound of the Jacobian determinant of the transformation, and τ_{lb} is the lower bound:

$$\begin{cases} \int \mu(\xi) d\xi = |\Omega| \\ \tau_{ub} > \mu(\xi) > \tau_{lb}. \end{cases} \tag{5.8}$$

A diffeomorphism is ensured by the fact that τ_{lb} is set to be above zero. The formulation is optimized using a step-then-correct algorithm.

Algorithm 1 Step-then-correct optimization

Given two 3D volumes, comprised of the fixed volume T_n and the moving volume T_{n+1}, the following steps are computed in order to calculate the deformation field ϕ:

Step 1: Compute the gradients of μ and γ, which are given by $\nabla\mu(T_n,T_{n+1},\phi)$ and $\nabla\gamma(T_n,T_{n+1},\phi)$

while $\delta > \delta_{th}$ *and* $i < max\_iter$ **do**

Step 2: Update gradients:

$$\mu_{i+1} = \mu_i + \delta \ \frac{\nabla\mu E_s}{max|\nabla\mu E_s|}$$

$$\gamma_{i+1} = \gamma_i + \delta \ \frac{\nabla\gamma E_s}{max|\nabla\gamma E_s|}$$

Step 3: Impose constraints from (5.8) for each pixel location $\xi \in \Omega$:

$\mu_{i+1} \leftarrow \max(\mu_{i+1}(\xi),\, \tau_{lb})$

$\mu_{i+1} \leftarrow \min(\mu_{i+1}(\xi),\, \tau_{ub})$

$$\mu_{i+1}(\xi) \leftarrow \ \frac{|\Omega|}{\sum_{\xi\subset\Omega}\mu_{i+1}(\xi)}$$

$\gamma_{i+1} \leftarrow \max(\gamma_{i+1}(\xi),\, \tau_{lb})$

$\gamma_{i+1} \leftarrow \min(\gamma_{i+1}(\xi),\, \tau_{ub})$

$$\gamma_{i+1}(\xi) \leftarrow \ \frac{|\Omega|}{\sum_{\xi\subset\Omega}\gamma_{i+1}(\xi)}$$

Step 4: Compute a vector field $\rho(\xi)$ that satisfies (5.7) and compute the deformation field ϕ.

Step 5: Compute the cost E_s.

if *current* $E_s <$ *previous* E_s **then**

$i \leftarrow i + 1$

Start from Step 1 of recomputing the gradients

else

Decrease step size δ

Start from Step 2 of updating the gradients

end

end

5.2.2 Numerical implementation

Divergence-curl system

The deformation field can be represented by traditional grid displacements, or by an indirect method using the divergence and curl representation of Helmholtz's theorem [96]. The divergence-curl (div-curl) system is used to transform the divergence and

curl representation of the deformation field into a set of Poisson equations that are solved using the Fast Fourier Transform (FFT) method. The div-curl system for the 3D case is given in Equation (5.9). The divergence operator can be interpreted as the change in density of the media at each point [97]. The divergence of the deformation field represents the radial motion while the curl operator represents the rotation of the media around every point [98]. The 3D operator directly extends from the 2D curl, where each rotational component about each of the three axes. Therefore the curl operator represents the rotational motion of the deformation field. The set of four equations in Equation (5.9) form a set of equations, where the deformation field is given by ϕ. The radial component is given by f^1 and the three rotational components are given by f^2, f^3 and f^4.

$$\begin{cases} div\phi = \dfrac{\partial \phi_x}{\partial x} + \dfrac{\partial \phi_y}{\partial y} + \dfrac{\partial \phi_z}{\partial z} = f^1 \\ curl_x\phi = \dfrac{\partial \phi_z}{\partial y} - \dfrac{\partial \phi_y}{\partial z} = f^2 \\ curl_y\phi = \dfrac{\partial \phi_x}{\partial z} - \dfrac{\partial \phi_z}{\partial x} = f^3 \\ curl_z\phi = \dfrac{\partial \phi_y}{\partial x} - \dfrac{\partial \phi_x}{\partial y} = f^4. \end{cases} \tag{5.9}$$

In order to solve for the (5.9), a set of Poisson equations can be formed, where then numerical solvers can be applied to solve the set of equations. To form the equations, first the derivative of each of the f^1, f^2, f^3, and f^4 terms is computed with respect to x, y, and z. These equations are given in (5.10), (5.11), (5.12) and (5.13), where $f^i_k = \dfrac{df^i}{dk}$, with i=1,2,...,4 and k=x,y,z:

$$\begin{cases} f^1_x = \dfrac{\partial f^1}{\partial x} & = \dfrac{\partial}{\partial x}(\dfrac{\partial \phi_x}{\partial x} + \dfrac{\partial \phi_y}{\partial y} + \dfrac{\partial \phi_z}{\partial z}) = \dfrac{\partial^2 \phi_x}{\partial x^2} + \dfrac{\partial^2 \phi_y}{\partial x \partial y} + \dfrac{\partial^2 \phi_z}{\partial x \partial z}, \\ f^1_y = \dfrac{\partial f^1}{\partial y} & = \dfrac{\partial}{\partial y}(\dfrac{\partial \phi_x}{\partial x} + \dfrac{\partial \phi_y}{\partial y} + \dfrac{\partial \phi_z}{\partial z}) = \dfrac{\partial^2 \phi_x}{\partial x \partial y} + \dfrac{\partial^2 \phi_y}{\partial y^2} + \dfrac{\partial^2 \phi_z}{\partial y \partial z} \\ f^1_z = \dfrac{\partial f^1}{\partial z}, & = \dfrac{\partial}{\partial z}(\dfrac{\partial \phi_x}{\partial x} + \dfrac{\partial \phi_y}{\partial y} + \dfrac{\partial \phi_z}{\partial z}) = \dfrac{\partial^2 \phi_x}{\partial x \partial z} + \dfrac{\partial^2 \phi_y}{\partial y \partial z} + \dfrac{\partial^2 \phi_z}{\partial z^2}. \end{cases} \tag{5.10}$$

$$\begin{cases} f_x^2 = \dfrac{\partial f^2}{\partial x} & = \dfrac{\partial}{\partial x}(\dfrac{\partial \phi_z}{\partial y} - \dfrac{\partial \phi_y}{\partial z}) = \dfrac{\partial^2 \phi_z}{\partial x \partial y} - \dfrac{\partial^2 \phi_y}{\partial x \partial z}, \\ f_y^2 = \dfrac{\partial f^2}{\partial y} & = \dfrac{\partial}{\partial y}(\dfrac{\partial \phi_z}{\partial y} - \dfrac{\partial \phi_y}{\partial z}) = \dfrac{\partial^2 \phi_z}{\partial y^2} - \dfrac{\partial^2 \phi_y}{\partial y \partial z}, \\ f_z^2 = \dfrac{\partial f^2}{\partial z} & = \dfrac{\partial}{\partial z}(\dfrac{\partial \phi_z}{\partial y} - \dfrac{\partial \phi_y}{\partial z}) = \dfrac{\partial^2 \phi_z}{\partial y \partial z} - \dfrac{\partial^2 \phi_y}{\partial z^2}. \end{cases} \tag{5.11}$$

$$\begin{cases} f_x^3 = \dfrac{\partial f^3}{\partial x} & = \dfrac{\partial}{\partial x}(\dfrac{\partial \phi_x}{\partial z} - \dfrac{\partial \phi_z}{\partial x}) = \dfrac{\partial^2 \phi_x}{\partial x \partial z} - \dfrac{\partial^2 \phi_z}{\partial x^2}, \\ f_y^3 = \dfrac{\partial f^3}{\partial y} & = \dfrac{\partial}{\partial y}(\dfrac{\partial \phi_x}{\partial z} - \dfrac{\partial \phi_z}{\partial x}) = \dfrac{\partial^2 \phi_x}{\partial y \partial z} - \dfrac{\partial^2 \phi_z}{\partial x \partial y}, \\ f_z^3 = \dfrac{\partial f^3}{\partial z} & = \dfrac{\partial}{\partial z}(\dfrac{\partial \phi_x}{\partial z} - \dfrac{\partial \phi_z}{\partial x}) = \dfrac{\partial^2 \phi_x}{\partial z^2} - \dfrac{\partial^2 \phi_z}{\partial x \partial z}. \end{cases} \tag{5.12}$$

$$\begin{cases} f_x^4 = \dfrac{\partial f^4}{\partial x} & = \dfrac{\partial}{\partial x}(\dfrac{\partial \phi_y}{\partial x} - \dfrac{\partial \phi_x}{\partial y}) = \dfrac{\partial^2 \phi_y}{\partial x^2} - \dfrac{\partial^2 \phi_x}{\partial x \partial y}, \\ f_y^4 = \dfrac{\partial f^4}{\partial y} & = \dfrac{\partial}{\partial y}(\dfrac{\partial \phi_y}{\partial x} - \dfrac{\partial \phi_x}{\partial y}) = \dfrac{\partial^2 \phi_y}{\partial x \partial y} - \dfrac{\partial^2 \phi_x}{\partial y^2}, \\ f_z^4 = \dfrac{\partial f^4}{\partial z} & = \dfrac{\partial}{\partial z}(\dfrac{\partial \phi_y}{\partial x} - \dfrac{\partial \phi_x}{\partial y}) = \dfrac{\partial^2 \phi_y}{\partial x \partial z} - \dfrac{\partial^2 \phi_x}{\partial y \partial z}. \end{cases} \tag{5.13}$$

In order to form the set of Poisson equations given by $\Delta\phi_x$, $\Delta\phi_y$ and $\Delta\phi_y$, the above relevant terms from (5.10), (5.11), (5.12), (5.13) are combined. Equation (5.14) gives the $\Delta\phi_x$ value after combining the terms from (5.10), (5.11), (5.12), (5.13), which can be applied to (5.15) and (5.16).

$$\begin{cases} \Delta\phi_x & = \dfrac{\partial^2 \phi_x}{\partial x^2} + \dfrac{\partial^2 \phi_x}{\partial y^2} + \dfrac{\partial^2 \phi_x}{\partial z^2} \\ & = (f_x^1 - \dfrac{\partial^2 \phi_y}{\partial x \partial y} - \dfrac{\partial^2 \phi_z}{\partial x \partial z}) + (\dfrac{\partial^2 \phi_y}{\partial x \partial y} - f_y^4) + (f_z^3 + \dfrac{\partial^2 \phi_z}{\partial x \partial z}) \\ & = f_x^1 + f_z^3 - f_y^4. \end{cases} \tag{5.14}$$

$$\begin{cases} \Delta\phi_y & = \dfrac{\partial^2 \phi_y}{\partial x^2} + \dfrac{\partial^2 \phi_y}{\partial y^2} + \dfrac{\partial^2 \phi_y}{\partial z^2} \\ & = (f_x^4 + \dfrac{\partial^2 \phi_x}{\partial x \partial y}) + (f_y^1 - \dfrac{\partial^2 \phi_x}{\partial x \partial y} - \dfrac{\partial^2 \phi_z}{\partial y \partial z}) + (\dfrac{\partial^2 \phi_z}{\partial y \partial z} - f_z^2) \\ & = f_y^1 + f_x^4 - f_z^2. \end{cases} \tag{5.15}$$

$$\begin{cases} \Delta\phi_z & = \dfrac{\partial^2\phi_z}{\partial x^2} + \dfrac{\partial^2\phi_z}{\partial y^2} + \dfrac{\partial^2\phi_z}{\partial z^2} \\ & = (\dfrac{\partial^2\phi_x}{\partial x\partial z} - f_x^3) + (f_y^2 + \dfrac{\partial^2\phi_y}{\partial y\partial z}) + (f_z^1 - \dfrac{\partial^2\phi_x}{\partial x\partial z} - \dfrac{\partial^2\phi_y}{\partial y\partial z}) \\ & = f_z^1 + f_y^2 - f_x^3. \end{cases} \tag{5.16}$$

The final set of Poisson equations are displayed in (5.17).

$$\begin{cases} \Delta\phi_x & = f_x^1 + f_z^3 - f_y^4 = F^1, \\ \Delta\phi_y & = f_y^1 + f_x^4 - f_z^2 = F^2, \\ \Delta\phi_z & = f_z^1 + f_y^2 - f_x^3 = F^3. \end{cases} \tag{5.17}$$

Several algorithms can be used to solve the set of Poisson equations [99]. The direct method of solving the Poisson equations involves first using the Dirichlet boundary condition, with boundary values set to zero. The Poisson equation can then be represented using a discretized version based on the second-order central difference equation. Writing this in matrix forms yields multiplication by the Laplacian operator. The matrix can be inverted to solve the Poisson equations and obtain exact values, but the size of the Laplacian matrix increases as the image size increases. Therefore instead of using a direct method to solve the Poisson equations, the method based on the FFT was chosen for this implementation.

Registration process

The registration process is performed sequentially over the temporal frames. Therefore, it may accumulate errors over time. A methodology was developed to reduce these tracking errors. Registration is performed in the forward and reverse directions and a weighting function is used to combine the sets of deformation fields. $DM^f_{n,n+1}$ encodes the forward displacement fields and $DM^b_{n,n+1}$ encodes the reverse displacement fields. Both sets of displacement fields are between the n and $n+1$th frames, where N represents the total number of frames in the sequence.

$$\begin{cases} w = (n-1)/(N-1) \\ DM_{n,n+1} = (1-w) \cdot DM^{f}_{n,n+1} + w \cdot DM^{b}_{n,n+1}. \end{cases} \tag{5.18}$$

Computation of the deformed meshes

As stated previously, the ED and ES ground truth meshes are used as input to the proposed algorithm to compute the mesh for each frame of the cardiac cycle. Figure 5.2 displays code snippets necessary to compute the contours for each frame of the cardiac cycle. The function `compute_auto_contours` takes as input the forward displacement fields DM_f and the reverse displacement fields DM_b, as well as the number of frames num_frames, a list of the indices of the ED and ES contours i_mc as well as a list of the input contours mc_list. The function `compute_auto_contours` calls `get_point_correspondence` which computes a weighted average of the contours based on the displacement fields using (5.18).

5.3 Results

The proposed method for 3D-to-3D registration was evaluated on two datasets: (1) MR scans from 20 patients from the Automated Cardiac Diagnosis Competition (ACDC) dataset [100], and (2) US scans from 10 patients scanned at the Mazankowski Alberta Heart Institute. The displacement fields were calculated for each frame in a pairwise manner over the entire cardiac cycle. The deformation fields were applied to the ED and ES reference mesh segmentations, in order to generate a segmentation of the LV for each frame of the cardiac cycle. A bounding box was defined to reduce the amount of time needed for the registration process and was set to be a margin of 10 voxels in the x, y, and z-direction. The following parameters were used for the diffeomorphic registration algorithm: (1) Maximum number of iterations was set to 20, (2) Values for the transformation Jacobian determinant τ_{lb} and τ_{ub} were set to 0.25 and 6.0 respectively to allow for large deformations in the cardiac tissue, (3) The

```
def compute_auto_contours(DM_f, DM_b, num_frames, i_mc, mc_list):

    endo_contour_list = [None] * num_frames

    for i in range(len(i_mc)):
        contour, index1, index2 = get_point_correspondence(DM_f, \
                                                           DM_b, \
                                                           i_mc[i],
                                                           i_mc[(i + 1) % len(i_mc)],
                                                           mc_list[i], \
                                                           mc_list[(i + 1) % len(i_mc)],
                                                           num_frames)

        for k in range(index1 + 1, index2 + 1):
            endo_contour_list[k % num_frames] = contour[k - index1 - 1]

    return endo_contour_list


def get_point_correspondence(DM_f, DM_b, index1, index2, pts1, pts2, num_frames):

    index2 += nframes if index2 <= index1 else 0

    contour_f, contour_b, contour = [], [], {}

    pts1_temp = pts1
    img1_temp = img1

    for k in np.arange(index1, index2 - 1):
        mesh_transformed_forward = transform_mesh(pts1_temp, DM_f)
        contour_f.append(mesh_transformed_forward)
        pts1_temp = mesh_transformed_forward

    pts2_temp = pts2

    for k in np.arange(index2, index1 + 1, -1):
        mesh_transformed_reverse = transform_mesh(pts2_temp, DM_b)
        contour_b.insert(0, mesh_transformed_reverse)
        pts2_temp = mesh_transformed_reverse

    for k in np.arange(index1, index2 - 1):
        w = 1.0 * (k - index1 + 1) / (1.0 * (index2 - index1))
        contour[k - index1] = ((1.0 - w) * contour_f[k - index1]) + (w * contour_b[k - index1])

    contour[index2 - index1 - 1] = pts2

    return contour
```

Figure 5.2: Code snippets to perform the computation of the contours using the forward and reverse displacement fields as well as the ED and ES input contours.

step size h for the Runge-Kutta method was set to 0.05 (20 steps), (4) The initial value of the step size δ was set to 0.5 for the step-then-correct optimization method, (5) the factor to reduce δ was set to 0.66, and (6) The minimum δ threshold δ_{th} was set to 0.0001.

The proposed registration method was implemented using Python 3.6.2 with PyTorch version 1.7.1 using an NVIDIA Tesla P100 GPU. The Visualization Toolkit (VTK) version 8.1.2 was employed to create the mesh representation of the LV. The Paraview software program version 5.7.0 was used to display differences between the ground truth mesh and the set of meshes from the registration methods.

5.3.1 Registration software packages

The proposed algorithm was compared to six other registration methods: Symmetric Normalization (SyN) algorithm from the Dipy package [101], two versions of the Demons algorithm from the ITK software package [85], two variants of RealTiTracker [102, 103], and the Elastix software package [19, 104]. Note that the registration packages were implemented using Python 3.6.2 on an NVIDIA Tesla C2075 graphics card and MATLAB version 2020b (Mathworks, Natick, Massachusetts, USA).

The Symmetric Normalization (SyN) algorithm is implemented in the Dipy software package [101]. The algorithm ensures a diffeomorphic transformation, which is defined by the fact that the function and the inverse are both smooth. The SyN algorithm extends a previous algorithm [105], in which a Lagrangian diffeomorphic registration method was employed. Invertibility constraints are used within the optimization process, which ensures that symmetry between the two volumes is guaranteed. The sum of squared differences (SSD) is employed as the similarity metric for the registration process. A multi-resolution method is employed using a Gaussian pyramid with three levels. Each level uses 10, 10, and 5 iterations respectively.

Two versions of the Demons algorithm were used from ITK, the classical Demons algorithm and a version that employs the use of fast symmetric forces [85]. To ensure

that the volumes being registered are similar, histogram matching is first applied. For the classical Demons algorithm, 50 iterations were used, and for the fast symmetric forces algorithm, 200 iterations were used. A Gaussian kernel of a standard deviation of 1.0 is used for both versions of the Demons algorithm to smooth the displacement field.

The RealTiTracker software contains a set of registration algorithms that are based on optical flow methods [106]. There are two main terms in the optical flow formulation: one that makes sure that the motion between two frames is small while the second term ensures that there is a small intensity difference between the two frames. There are two forms for the second term, the conservation of intensity. In this term, there are two methods in which the spatial and temporal derivatives can be used, either the L_1 norm for the L_2L_1 functional or the L_2 norm for the L_2L_2 functional. The weighting term alpha determines how sensitive to the gray level intensity the motion should be. For the L_2L_1 functional this value is set to 0.4 and for the L_2L_2 functional this value is set to 0.1. These values were adapted from the example codes provided in the RealTiTracker MATLAB package.

Elastix [19, 104] is a software package that consists of various transformation models, cost functions, and optimization methods. The B-spline transformation was used for registration in a multi-resolution framework with five levels. Mattes mutual information [107] was used for the similarity metric and adaptive stochastic gradient descent was used for the optimizer.

5.3.2 Datasets used

Automated Cardiac Diagnosis Challenge (ACDC) dataset

Two datasets were employed for the evaluation of the proposed 3D-to-3D registration algorithm. The first dataset is the publicly available Automated Cardiac Diagnosis Challenge (ACDC) dataset. The dataset contains a set of 100 patients from the University Hospital of Dijon, France, scanned using cine MR imaging [100]. Patients

were scanned using a 1.5T scanner (Siemens Arena, Siemens Medical Solutions, Germany) and a 3T scanner (Siemens Trio Tim, Siemens Medical Solutions, Germany). Short axis slices were obtained using a breath-hold acquisition with a slice thickness between 5 to 8 mm. A subset of 20 patients from the 100 was chosen in order to evaluate the proposed registration algorithm. The number of frames of the subset of 20 patients ranged from 13 to 35 frames for the entire cardiac cycle. The total number of frames was 521 over the 20 patients. The volumes of the patient datasets used were in the ranges of $184 \times 216 \times 8$ to $256 \times 256 \times 11$ voxels. The corresponding resolution ranged from $1.367 \times 1.367 \times 10.0$ mm to $1.875 \times 1.875 \times 10.0$ mm.

The ground truth was delineated for the ED and ES frames by one clinical expert. The patient population comprised of normal subjects, those who suffered a previous myocardial infarction, patients with various myopathies, and those with an abnormal right ventricle. The ground truth is only provided for the ED and ES frames for the ACDC dataset, but evaluation of the proposed method over the entire cardiac cycle is necessary. An automated method was used to reduce the time needed for an expert to annotate each short-axis slice for each patient and frame. The method of [76] was used to obtain the ground truth contours for each short-axis slice temporal sequence. The set of temporal contours were created using the already provided delineations for the ED and ES frames. An expert radiologist reviewed and edited the final ground truth contours when necessary.

Mazankowski Alberta Heart Institute dataset

Ten patients were scanned at the Mazankowski Alberta Heart Institute (Edmonton, Alberta, Canada) to assess LV function. They were approved to be scanned by the human research ethics committee at the University of Alberta. An expert sonographer scanned the set of patients using an X5-1 transducer on a Philips iD33 ultrasound machine (Philips Healthcare, Best, Netherlands). A 3D sector angle of 70×80 degrees was used to achieve a volume rate greater than 20 volumes per second. The number

of frames in the dataset from the set of patients ranged from 16 to 26 for a total of 213 frames. The size of the volumes ranged from $224 \times 176 \times 208$ to $256 \times 176 \times 208$ voxels. The resolutions respectively were $0.617 \times 0.787 \times 0.533$ mm to $0.810 \times 1.005 \times 0.681$ mm.

An expert cardiologist provided the ground truth segmentation using the TomTec Arena software (TomTec Imaging Systems, Unterschleissheim, Germany). The software uses a semi-automated 3D speckle tracking approach in order to delineate the LV over the cardiac cycle. The ground truth segmentation meshes and the volume of the LV were provided through the software.

5.3.3 Metrics

Mean absolute distance

The mean absolute distance (d_m) is computed by taking each point in the proposed approach mesh S, and locating the closest the point in the ground truth reference mesh R. The mean of these minimum distance values is then computed [81], where the result is given in mm:

$$d_m(S, R) = \frac{1}{N_s} \sum_{s \in S} \min_{r \in R}(dist(s, r)). \tag{5.19}$$

Hausdorff distance

The Hausdorff distance (d_H) is calculated by finding a measure of the maximum distance between the proposed mesh S and the ground truth reference mesh R [82]. The result is reported in mm. The d_H is calculated by the following equation, where the distance used between the points is Euclidean:

$$\mathrm{HD}(S, R) = \max \left\{ \sup_{s \in S} \inf_{r \in R} \mathrm{d}(s, r), \sup_{r \in R} \inf_{s \in S} \mathrm{d}(s, r). \right\} \tag{5.20}$$

Dice score

The Dice score is a measure of the amount of overlap between the volume from the proposed approach V and the reference volume V_{ref}. A value of 1 indicates complete overlap between the two volumes and a value of 0 indicates no overlap.

$$\text{Dice} = \frac{2(V \cap V_{ref})}{(V + V_{ref})}. \tag{5.21}$$

Determinant of the Jacobian

The Jacobian of a displacement field provides information about the local transformation at each point. The determinant of the Jacobian indicates whether topology is preserved for the local transformation. A value less than 0 indicates that topology is not preserved and that mesh folding has occurred. This in turn signifies that the deformation field is implausible as it should represent anatomically possible motion.

5.3.4 MRI results

Quantitative evaluation

Distance metrics and determinant of Jacobian analysis The proposed algorithm was evaluated along with six other registration methods using the mean absolute distance d_m, Hausdorff distance d_H, the Dice score $Dice$, and the percentage of voxels of the Jacobian determinant that are less than zero $J_{<0}\%$. Observing the d_m and the d_H metrics, it can be seen that the proposed method performs better than the other methods. The Elastix registration method has a slightly higher performance than the proposed method in terms of the $Dice$ score, with a value of 98.21% compared to the proposed method of 98.10%. Observing the $J_{<0}\%$ value, it can be seen that the proposed algorithm results in no voxels below zero, which indicates that mesh folding does not occur. The Elastix registration algorithm has a $J_{<0}\%$ value of 0.184, indicating some mesh folding occurred. To determine if the set of distance measures for each of the registration methods are sufficiently different

from each other, Kruskal-Wallis H significance tests were performed. The statistical tests were performed for each of the d_m, d_H and *Dice* metrics for each frame. With a set alpha significance value of 0.05, it can be observed that the p values calculated are less than 0.0001, which demonstrates that there are significant differences among the set of registration methods. The average time to perform registration was also recorded for each of the methods, where the proposed method yielded a value of 0.59 seconds. Note that the proposed algorithm was written in Python 3.6.2 with PyTorch version 1.7.1 using an NVIDIA Tesla P100 GPU, while the other registration methods were run using Python 3.6.2 on an NVIDIA Tesla C2075 graphics card and MATLAB 2020b (Mathworks, Natick, Massachusetts, USA). Table 5.1 displays the distance metrics and other measures for the ACDC dataset.

Volume analysis One part of diagnosing a patient is the analysis of the volume of the LV over the cardiac cycle. A Bland-Altman (BA) plot can be used to analyze the difference in the volumes between the ground truth segmentation and the volumes generated from the proposed method, or other registration methods. The plot produces a bias metric, which is the mean of the differences between the two sets of volumes. The 95% limits of agreement (LOA) are also calculated, set to the bias $\pm 1.96\times$the standard deviation of the differences. Figure 5.3 displays the BA plot for a comparison between the ground truth volumes and the volumes resulting from the proposed methodology. The bias is indicated by a red line, and the LOA by two yellow lines. The reference line is indicated in black. It can be seen that there is a slight bias in estimating the volumes, where there is an underestimation of the volumes compared to the ground truth. In general, there is a good amount of clustering around the reference line.

The bias and LOA are also calculated for the other registration methods versus the

Table 5.1: Quantitative evaluation results for the MRI dataset: The proposed algorithm was compared to the ground truth and six other registration algorithms, symmetric normalization from the Dipy package, two versions of the Demons algorithm (classical and fast symmetric forces) from ITK, RealTiTracker (L_2L_1 and L_2L_2) and Elastix. The following metrics are reported for each method: mean absolute distance d_m in mm, Hausdorff distance d_H in mm, Dice score $Dice$, and the percentage of voxels of the Jacobian determinant that are less than zero $J_{<0}\%$. Results are evaluated over 20 subjects using MRI temporal sequences from the ACDC dataset. Smaller values of d_m, d_H and larger values of $Dice$ indicate more accurate segmentation results. As the determinant of Jacobian value less than zero indicates mesh folding, a number greater than zero for $J_{<0}\%$ indicates mesh folding occurred. In order to determine if a significant difference exists for the d_m, d_H and the $Dice$ metrics among the set of registration methods, Kruskal-Wallis H significance tests were performed. The average time to perform for a single 3D-3D frame is provided in seconds. The standard deviation values for all of the metrics are given in parentheses. Values that are highlighted in bold indicate the metric that gave the highest performance compared to the other algorithms.

	d_m (mm)	d_H (mm)	$Dice$ (%)	$J_{<0}$ (%)	$Time$ (seconds)
Proposed method	**0.48** (0.23)	**4.43** (1.87)	98.10 (0.90)	0 (0)	0.59 (0.13)
Dipy SyN	1.01 (0.56)	5.03 (1.98)	95.98 (2.19)	0 (0)	1.23 (0.25)
Demons	0.73 (0.31)	5.43 (2.03)	97.26 (1.26)	6.87×10^{-4} (2.55×10^{-3})	2.22 (0.57)
Demons fast symmetric forces	0.65 (0.32)	4.66 (1.87)	97.50 (1.22)	0 (0)	5.95 (2.56)
RealTiTracker (L_2L_1)	0.77 (0.37)	4.70 (1.91)	97.29 (1.36)	3.16×10^{-5} (5.60×10^{-4})	1.24 (0.36)
RealTiTracker (L_2L_2)	0.67 (0.35)	4.62 (1.90)	97.60 (1.27)	8.83×10^{-3} (5.41×10^{-2})	0.88 (0.31)
Elastix	0.50 (0.22)	4.66 (1.80)	**98.21** (0.82)	0.184 (0.803)	8.12 (1.28)
Kruskal-Wallis H test	p<0.0001	p<0.0001	p<0.0001		

ground truth segmentations as displayed in Table 5.2. It can be observed that the Demons and Elastix registration methods result in slightly lower bias values compared to the proposed method. The positive number for all of the bias values indicates that the registration methods slightly underestimate the ground truth volume.

Volume curves are another method used to aid in the diagnosis of the patient, which provide the volume of the LV in mL for each frame of the cardiac cycle. Figure 5.4 displays an example of a set of volume curves from one patient, where the ground truth is displayed in red-filled circles and the proposed method in neon green squares. The six other registration methods are displayed on the volume curve in dotted lines. It can be seen that especially in the diastolic portion of the cardiac cycle, the pro-

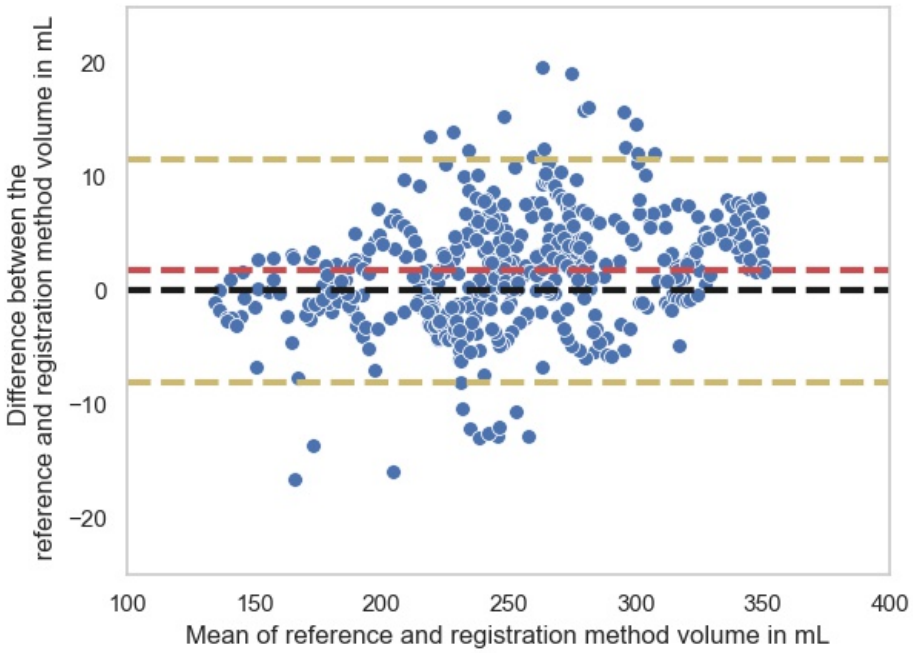

Figure 5.3: The Bland-Altman plot for the ground truth volumes versus the volumes resulting from the proposed method. The bias is indicated by a red line, and the limits of agreement by two yellow lines. The reference line is indicated in black.

Table 5.2: Bland Altman bias and limits of agreement (LOA) values for each of the registration methods compared to the ground truth volumes.

Registration method	$bias$	LOA_1	LOA_2
Proposed method	1.77	−8.06	11.60
Demons	0.35	−13.87	14.57
Demons fsf	2.09	−11.94	16.11
Dipy SyN	2.77	−24.88	30.42
RealTiTracker L2L2	6.95	−6.41	20.30
RealTiTracker L2L1	8.57	−4.95	22.09
Elastix	0.92	−10.29	12.12

posed method closely follows the ground truth compared to the other methods which perform poorly.

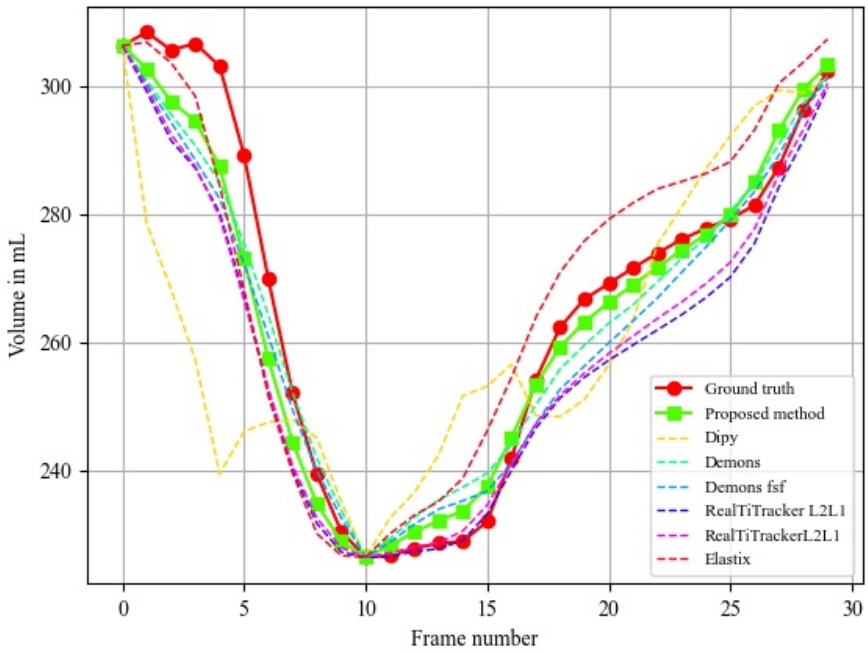

Figure 5.4: Example volume curves from one patient from the ACDC MRI dataset. The ground truth is displayed in red filled circles, and the proposed method is displayed in neon green squares. The other registration methods are shown in dotted lines without markers.

Visual inspection

Distance mesh visualization Visually assessing the mean absolute distance between a registration method and the ground truth is a convenient way to compare across different registration methods. Figure 5.5 displays the difference between the ground truth mesh and the proposed method compared to the six other registration methods for a frame in the systolic phase, and Figure 5.6 displays the mesh difference for a frame in the diastolic phase. Areas in red indicate a large difference between the ground truth and the registration method (in mm). Areas highlighted in blue indicate a small difference. In the figure, for ease of visualization, the ground truth

meshes are displayed in gray. The first row displays examples of the meshes for a frame in systole, while the second row displays meshes for a frame in diastole. It can be observed for the proposed method that the mesh closely follows the ground truth.

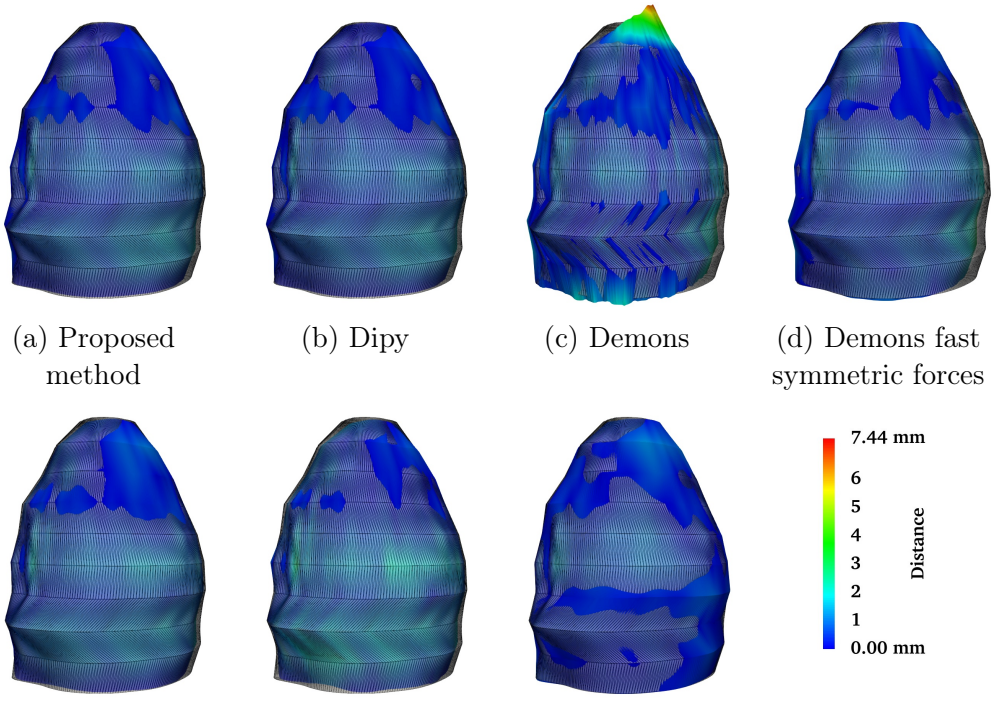

(a) Proposed method (b) Dipy (c) Demons (d) Demons fast symmetric forces

(e) RealTiTracker - L_2L_2 (f) RealTiTracker - L_2L_1 (g) Elastix (h) Colorbar

Figure 5.5: Difference in the mesh between the ground truth and the proposed method in the ACDC dataset for a frame in the systolic phase: (a) Proposed method (b) Dipy (c) Demons (d) Demons fast symmetric forces (e) RealTiTracker - L_2L_2 (f) RealTiTracker - L_2L_1 (g) Elastix (h) Colorbar

Contour trajectory plot A trajectory plot can be used to visually assess the complete set of contour points. Each point in the mesh is plotted over time and line segments of the same color connect the points. To improve visualization for the user, different colors are used to plot the series of points. Figure 5.7 displays the trajectory plots from one example patient from the ACDC dataset. The ground truth trajectory plot is displayed on the left, and the plot from the proposed method on the right. Visually speaking, it can be observed that the trajectory plots from the proposed method are in close agreement with the ground truth.

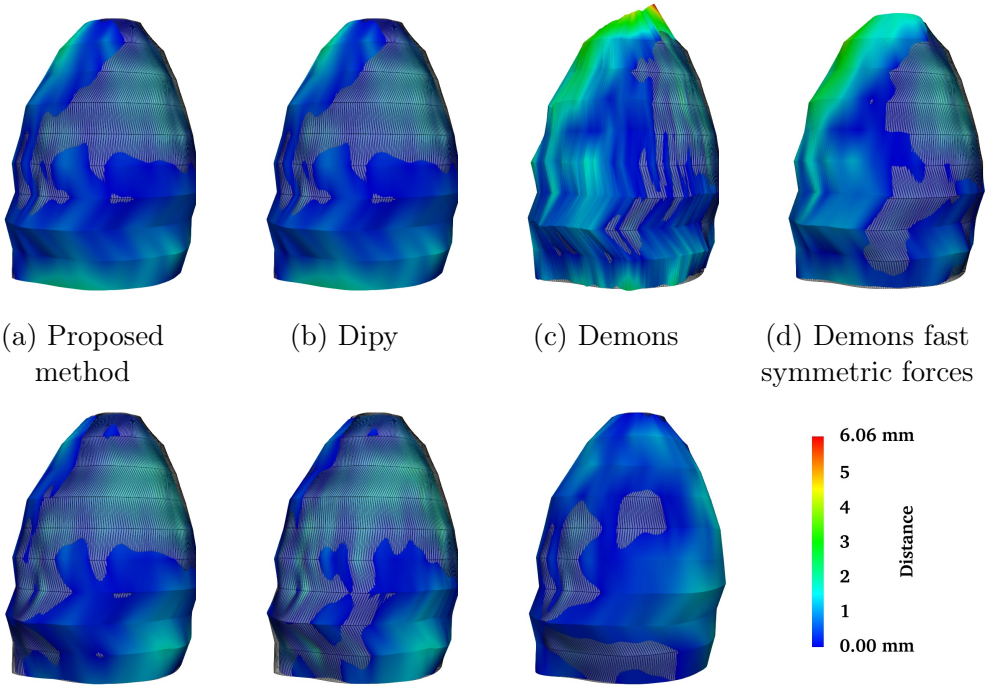

(a) Proposed method (b) Dipy (c) Demons (d) Demons fast symmetric forces

(e) RealTiTracker - L_2L_2 (f) RealTiTracker - L_2L_1 (g) Elastix (h) Colorbar

Figure 5.6: Difference in the mesh between the ground truth and the proposed method in the ACDC dataset for a frame in the diastolic phase: (a) Proposed method (b) Dipy (c) Demons (d) Demons fast symmetric forces (e) RealTiTracker - L_2L_2 (f) RealTiTracker - L_2L_1 (g) Elastix (h) Colorbar

(a) Ground truth (b) Proposed approach

Figure 5.7: Example trajectory plots from a patient from the ACDC MRI dataset, where the figure on the left displays the (a) ground truth and the figure on the right displays the (b) proposed method.

5.3.5 Ultrasound results

Quantitative evaluation

Distance metrics and determinant of Jacobian The proposed registration algorithm was evaluated against the ground truth and compared to the other registration algorithms using the metrics d_m, d_H, $Dice$, and $J_{<0}\%$ as shown in Table 5.3. It can be seen that the proposed algorithm has a lower d_m and higher $Dice$ score compared to the other registration methods, but a slightly higher d_H value compared to Elastix. The average time to perform the registration for a single 3D to 3D frame is 2.69 seconds. Note that the proposed algorithm was written in Python 3.6.2 with PyTorch version 1.7.1 using an NVIDIA Tesla P100 GPU, while the other registration methods were run using Python 3.6.2 on an NVIDIA Tesla C2075 graphics card. Observing the value of $J_{<0}\%$ equal to zero indicates there is no mesh folding for only the proposed method and Elastix.

Volume analysis A Bland-Altman analysis was also performed for the US dataset from the Mazankowski as seen in Figure 5.8. The red line indicates the bias, while the two yellow lines indicate the limits of agreement. The black line is the 0 reference line, indicating that the volumes from the two methods match. The bias is slightly higher than the reference line, indicating a small underestimation of the volume of the ventricle compared to the ground truth. The volumes for all patients are plotted and seem well clustered around the reference line except for a few outliers.

The bias and limits of agreement are also given for the other registration methods in Table 5.4. The proposed method yields the smallest bias value, indicating that the volume prediction is closer to the ground truth compared to the other registration approaches.

Table 5.3: Quantitative evaluation results for the US dataset: The proposed algorithm was compared to the ground truth and six other registration algorithms, symmetric normalization from the Dipy package, two versions of the Demons algorithm (classical and fast symmetric forces) from ITK, RealTiTracker (L_2L_1 and L_2L_2) and Elastix. The following metrics are reported for each method: mean absolute distance d_m in mm, Hausdorff distance d_H in mm, Dice score $Dice$, and the percentage of voxels of the Jacobian determinant that are less than zero $J_{<0}\%$. Results are evaluated over 10 subjects using US temporal sequences from the Mazankowski Alberta Heart Institute. Smaller values of d_m, d_H and larger values of $Dice$ indicate more accurate segmentation results. As a determinant of Jacobian value less than zero indicates mesh folding, a number greater than zero for $J_{<0}\%$ indicates mesh folding occurred. In order to determine if a significant difference exists for the d_m, d_H and the $Dice$ metrics among the set of registration methods, Kruskal-Wallis H significance tests were performed. The average time to perform for a single 3D-3D frame is provided in seconds. The standard deviation values for all of the metrics are given in parentheses. Values that are highlighted in bold indicate the metric that gave the highest performance compared to the other algorithms.

	d_m (mm)	d_H (mm)	$Dice$ (%)	$J_{<0}$ (%)	$Time$ (seconds)
Proposed method	**1.07** (0.32)	5.26 (1.74)	**92.90** (2.42)	0 (0)	2.69 (0.64)
Dipy SyN	2.42 (0.89)	7.84 (2.32)	82.30 (7.28)	2.85×10^{-6} (4.16×10^{-5})	28.04 (7.08)
Demons	1.13 (0.30)	5.92 (1.54)	91.29 (2.93)	0.276 (0.168)	7.55 (1.62)
Demons fast symmetric forces	1.14 (0.39)	4.59 (1.75)	91.31 (3.63)	4.32×10^{-3} (1.16×10^{-2})	15.24 (17.51)
RealTiTracker (L_2L_1)	1.16 (0.36)	5.58 (2.06)	92.41 (2.43)	3.51×10^{-3} (9.53×10^{-3})	2.54 (0.37)
RealTiTracker (L_2L_2)	1.16 (0.36)	5.97 (2.13)	92.34 (2.44)	0.028 (0.043)	2.41 (0.33)
Elastix	1.26 (0.51)	**4.58** (1.46)	92.40 (2.44)	0 (0)	14.30 (2.08)
Kruskal-Wallis H test	p<0.0001	p<0.0001	p<0.0001		

Table 5.4: Bland Altman bias and limits of agreement (LOA) values for each of the registration methods compared to the ground truth volumes.

Registration method	$bias$	LOA_1	LOA_2
Proposed method	0.73	−6.23	7.69
Demons	1.01	−8.29	10.32
Demons fsf	1.09	−10.09	12.28
Dipy SyN	2.62	−20.40	25.63
RealTiTracker L2L2	1.80	−4.74	8.34
RealTiTracker L2L1	2.04	−4.65	8.72
Elastix	−1.56	−12.39	9.27

Examining the volume over the entire cycle can be used to observe the overall systolic and diastolic function of the patient. Figure 5.9 displays an example of a set of volume

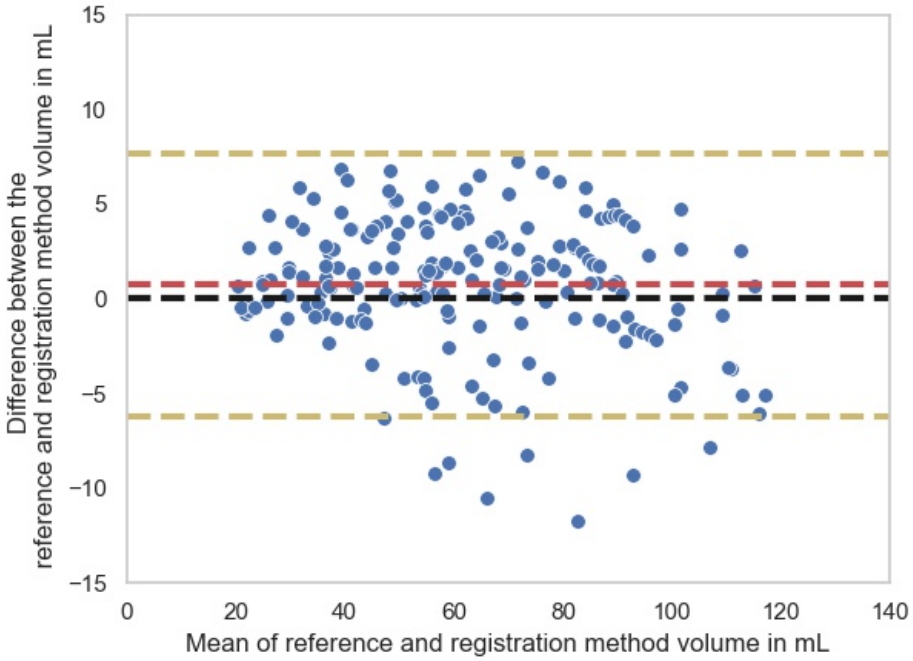

Figure 5.8: The Bland-Altman plot for the ground truth volumes versus the volumes resulting from the proposed method. The bias is indicated by a red line, and the limits of agreement by two yellow lines. The reference line is indicated in black.

curves from one patient. The ground truth is displayed in red-filled circles and the proposed algorithm in neon green squares. The improvement in using the proposed method is readily apparent especially in the diastolic phase, where a number of the other registration methods perform poorly.

Visual inspection

Distance mesh visualization The mean absolute distance can be visualized in terms of a distance mesh. Figure 5.10 displays the difference between the ground truth mesh and the proposed method and other algorithms for a frame in the systolic phase, and Figure 5.11 displays the difference for a frame in the diastolic phase. Red indicates that the distance between the ground truth and the registration algorithm is large (in mm) while blue indicates that the distance is minimal. The ground truth mesh in the figure is displayed in gray. The first row displays the differences for a

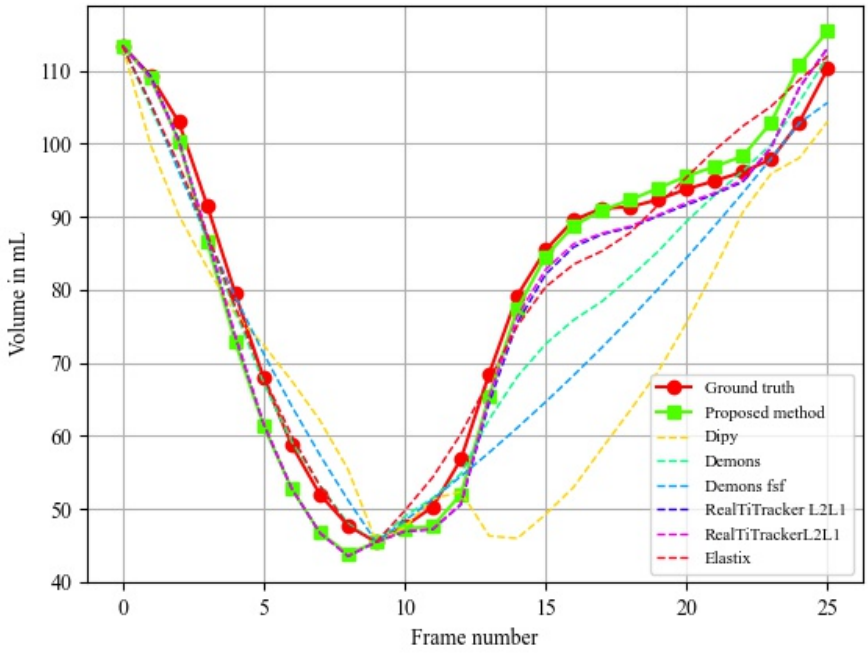

Figure 5.9: Example volume curves from one patient from the Mazankowski ultrasound dataset. The ground truth is displayed in red filled circles, and the proposed method is displayed in neon green squares. The other registration methods are shown in dotted lines without markers.

frame within the systolic phase, while the second row displays the differences from a frame within the diastolic phase. It can be observed that the mesh from the proposed method closely follows the ground truth.

Contour trajectory plot Another way to visually assess the entire set of contour points is to use a trajectory plot. All points in the mesh are plotted over time, and line segments of the same color connect the points. The use of different colors is included to improve visualization for the user. Figure 5.12 displays the trajectory plots from one patient from the Mazankowski Alberta Heart Institute dataset. The ground truth trajectory plot is displayed on the left, and the plot from the proposed method on the right. Visually speaking, it can be observed that the trajectory plots from the proposed method are in close agreement with the ground truth.

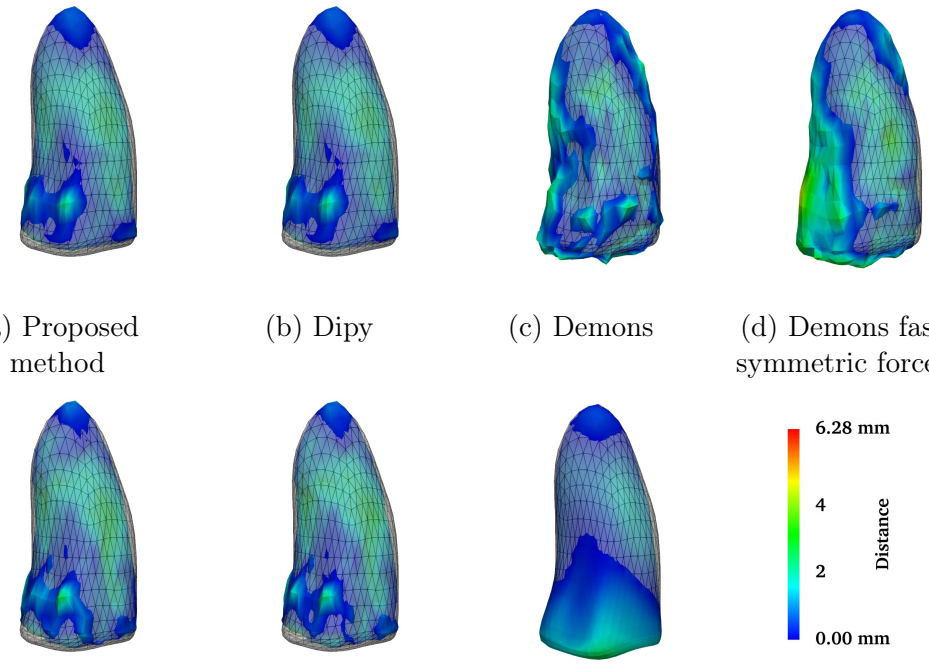

(a) Proposed method (b) Dipy (c) Demons (d) Demons fast symmetric forces

(e) RealTiTracker - L_2L_2 (f) RealTiTracker - L_2L_1 (g) Elastix (h) Colorbar

Figure 5.10: Difference in the mesh between the ground truth and the proposed method in the Maz dataset for a frame in the systolic phase: (a) Proposed method (b) Dipy (c) Demons (d) Demons fast symmetric forces (e) RealTiTracker - L_2L_2 (f) RealTiTracker - L_2L_1 (g) Elastix (h) Colorbar

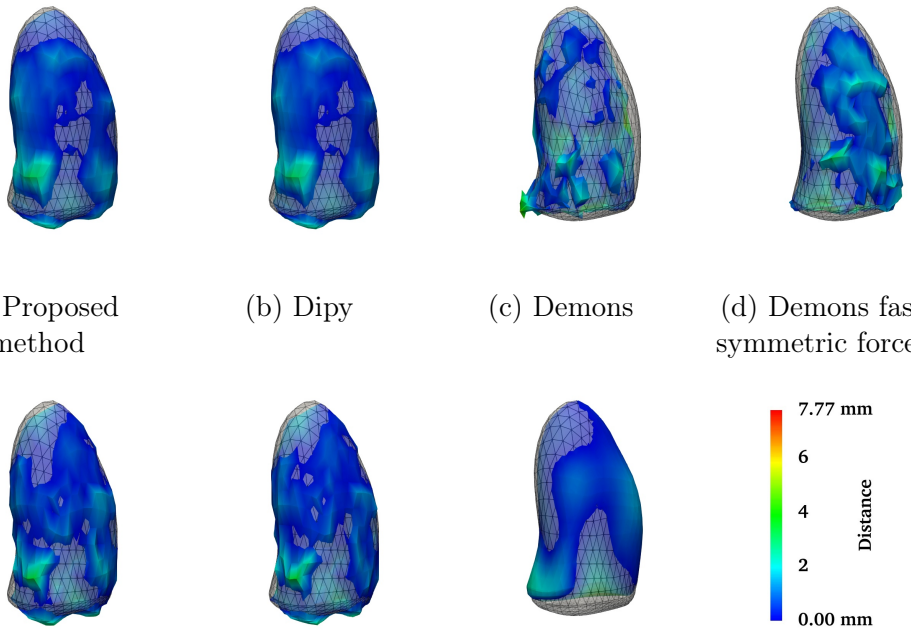

(a) Proposed method (b) Dipy (c) Demons (d) Demons fast symmetric forces

(e) RealTiTracker - L_2L_2 (f) RealTiTracker - L_2L_1 (g) Elastix (h) Colorbar

Figure 5.11: Difference in the mesh between the ground truth and the proposed method in the Maz dataset for a frame in the diastolic phase: (a) Proposed method (b) Dipy (c) Demons (d) Demons fast symmetric forces (e) RealTiTracker - L_2L_2 (f) RealTiTracker - L_2L_1 (g) Elastix (h) Colorbar

(a) Ground truth (b) Proposed approach

Figure 5.12: Example trajectory plots from a patient from the Mazankowski US dataset, where the figure on the left displays the (a) ground truth and the figure on the right displays the (b) proposed method.

5.4 Additional experiments

5.4.1 Diffeomorphic constraints experiment

An experiment was performed in order to evaluate the use of the diffeomorphic constraints on the ACDC MRI and Mazankowski US datasets. The proposed registration method was run with and without the use of the diffeomorphic constraints. Table 5.5 displays the distance metrics as well as the percentage of voxels that have the determinant of Jacobian less than zero, given by $J_{<0}\%$. It can be seen that for the proposed method, the distance metrics yield minor differences, except for d_H where the difference is large for the US dataset. Using the diffeomorphic constraints yields no mesh folding (indicated by the value of zero), while not including the constraints results in a small percentage of mesh folding. This further validates the usefulness of the diffeomorphic constraints to the registration algorithm.

Table 5.5: Diffeomorphic constraint experiment results: The diffeomorphic constraints were removed in order to understand the effect on the determinant of the Jacobian metric. The percentage of voxels with a determinant of the Jacobian less than zero is given by $J_{<0}\%$, indicating mesh folding. The mean absolute difference d_m in mm, Hausdorff distance d_H in mm, Dice score $Dice$ are also provided for comparison.

Dataset	Constraint	d_m (mm)	d_H (mm)	$Dice$ (%)	$J_{<0}$ (%)
MRI	include	0.48 (0.23)	4.43 (1.87)	98.10 (0.90)	0 (0)
MRI	exclude	0.49 (0.23)	4.61 (2.13)	98.09 (0.91)	6.23×10^{-3} (2.76×10^{-2})
US	include	1.07 (0.32)	5.26 (1.74)	92.90 (2.42)	0 (0)
US	exclude	1.07 (0.32)	7.48 (5.86)	92.80 (2.45)	7.82×10^{-3} (2.01×10^{-2})

Figure 5.13 displays the determinant of the Jacobian with and without the diffeomorphic constraints for the two datasets. The first row displays figures from the MRI dataset, while the second row displays figures from the US dataset. The first column indicates the warped image, the middle column displays the determinant of Jacobian with the diffeomorphic constraints, and the last column displays the deter-

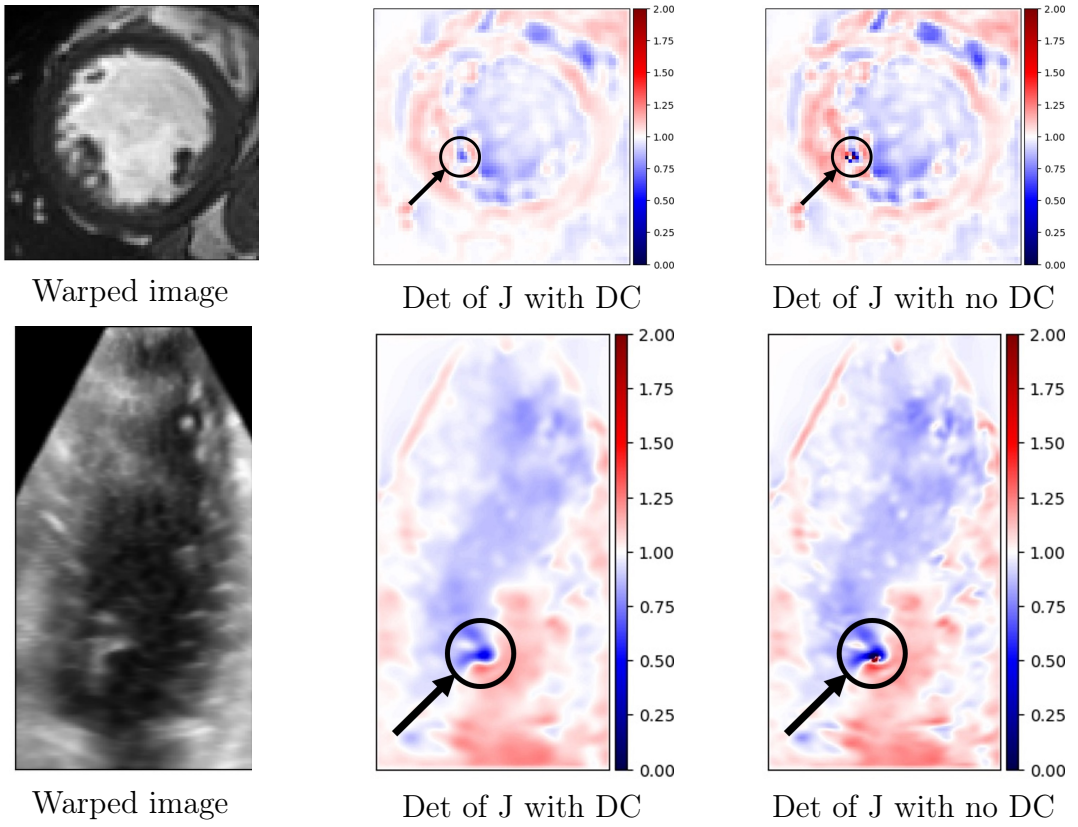

Figure 5.13: Examples from a patient from the MRI dataset (first row) and a patient from the US data (second row). The first column shows the warped image, the second column displays the determinant of the Jacobian map from using the diffeomorphic constraints, and the third column displays the determinant of the Jacobian map without using the constraints. The regions of interest inside the circle are indicated by an arrow, where mesh folding has occurred for the case where no diffeomorphic constraints are applied.

minant of the Jacobian with no diffeomorphic constraints. Black pixels indicate that the determinant of the Jacobian is less than or equal to zero, displaying mesh folding. Comparing the areas inside the circle (indicated by an arrow), it can be seen that there are slight discontinuities in the images with no diffeomorphic constraints.

5.5 Conclusion

A 3D-to-3D diffeomorphic registration algorithm for the application of segmentation of the LV has been developed. The proposed algorithm was evaluated on a subset of the publicly available ACDC Challenge dataset [100] as well as a set of US sequences obtained from the Mazankowski Alberta Heart Institute. The proposed algorithm was compared to six other registration methods, Symmetric Normalization diffeomorphic registration from the Dipy package [101], two versions of the Demons algorithm (classical and fast symmetric forces) from ITK [85], two variants of RealTiTracker [102, 103], and the Elastix software package [19, 104].

The proposed algorithm is diffeomorphic, allowing it to capture the true deformation of the cardiac tissue. Observing the percentage of voxels with a Jacobian determinant less than zero, all of the other registration methods yielded mesh folding for either the MRI dataset, US dataset, or both. The presence of mesh folding may result in the inability of these methods to capture the true anatomical motion.

There are several advantages of using the proposed algorithm. A manually created training set is not required, which may be difficult depending on patient abnormalities. A geometric assumption is also not made concerning the shape of the LV, which is important in the algorithm's ability to capture the anatomical differences. The algorithm has been evaluated on both MRI and US temporal sequences, as well as a wide variety of patients, making it robust to the imaging modality and patient diagnosis. The diffeomorphic algorithm is also unique because the deformation field is represented using the radial and rotational components, appropriate for cardiac analysis.

One limitation of the proposed method is the effect of the image quality on the performance of the algorithm. Large abnormalities, artifacts, and other sources of noise may affect the voxel-to-voxel correspondence mapping. Preprocessing could be performed to remove some of the noise in the future. A second limitation concerns the

methods used for obtaining the ground truth for both the ACDC and Mazankowski datasets. For the ACDC dataset, the method of [76] was used to create the ground truth for the frames in the cardiac cycle based on the ED and ES ground truth contours. The process involved using the 2D registration method for each axial slice across the temporal sequence. For the US dataset from the Mazankowski Alberta Heart Institute, the cardiologist employed the use of TomTec Arena to generate the ground truth. In the future, it would be useful to have the cardiologist manually annotate each frame in the cardiac cycle without the use of external software. It would also be useful in the future to have more than one expert annotate the ground truth in order to perform intra-observer and inter-observer studies.

A diffeomorphic registration algorithm for 3D volumes has been proposed, with the application of semi-automated segmentation of the LV. The method has been applied and validated on MR and ultrasound temporal sequences of the heart. The proposed method was compared to a set of registration software packages, in terms of the Dice score the proposed method yielded a value of 98.10 (0.90)% and 92.90 (2.42)% for the MRI and US datasets respectively.

Chapter 6

Conclusions & Future Work

In this chapter, an overview of the work accomplished is provided. Limitations of each of the achievements are outlined and discussed, and plans for improvements and future work are detailed.

6.1 Overview

Cardiac-related diseases affect millions of people in Canada each year and are the second leading cause of death in the country (2017) [0]. Early diagnosis and detection of various cardiac diseases in a non-invasive manner would be beneficial to clinicians. MRI is often considered the gold standard when it concerns the imaging of the heart. Unfortunately, MRI suffers from several drawbacks including the high cost and the fact that it is not portable. Echocardiography or ultrasound imaging has therefore been used by clinicians to address the above issues.

Along with selecting the proper imaging modality for the patient, the analysis methods used for diagnosis are of utmost importance. The left ventricle is often analyzed in cardiac issues as it provides useful clinical indices for describing cardiac function. For instance, the ejection fraction percentage, calculated from the volume of the left ventricle when it is the largest and the smallest, indicates the heart's efficiency at pumping blood.

It is crucial for the method to rely on minimal user interaction, as it is time-

consuming for clinicians to delineate anatomical structures of interest. It is also important for the delineation method to be reproducible and not rely on geometrical assumptions for shapes of the chambers.

In the proposed work, methods have been developed to address the shortcomings listed above. In particular, approaches for semi-automated delineation have been developed that have minimal user interaction, do not rely on geometrical priors, and do not require the use of training data.

6.1.1 Accomplishments

3D spatial segmentation in US volumes

In Chapter 3 a method for semi-automated delineation of the left ventricle, with minimal user interaction, has been developed. The user selects an axis between the apex and the base, where angular slices are then generated. The user then delineates the endocardium on two orthogonal slices, and a diffeomorphic registration algorithm is then used to automatically propagate this contour for all slices. A mesh is formed from these contours for both end-diastole and end-systole. The CETUS dataset [80] was used to evaluate our algorithm against a set of ground truth meshes provided by expert cardiologists. The method was compared to nine other semi-automated and fully automated algorithms and performed on par with the other methods in terms of standard distance and clinical metrics.

3D temporal segmentation in US sequences

In Chapter 4, an algorithm for semi-automated delineation of the left ventricle over the cardiac cycle was developed. The work is extended from Chapter 3, where the method is first used to obtain a segmentation at end-diastole and end-systole. Temporal segmentation is then performed by propagating a coarse set of contours from end-diastole and end-systole for the entire cardiac cycle. The method was validated on a set of 18 subjects from the Mazankowski Alberta Heart Institute, where the ground

truth was annotated by an expert cardiologist using the TomTec Arena software. Compared to four other registration methods, the proposed method achieved high performance in distance and clinical metrics.

3D-to-3D diffeomorphic registration algorithm

In Chapter 5, a 3D-to-3D diffeomorphic registration algorithm is proposed. Instead of using traditional grid displacements to model the deformation field, the field is represented by the divergence and curl operators. These representations of the radial and rotational components make it appropriate to model the deformation of the dynamic heart. The method is validated on two sets of data, a set of 20 subjects from the ACDC MRI dataset, and a set of 10 subjects scanned using ultrasound from the Mazankowski Alberta Heart Institute. The method is also compared to six other registration algorithms, where the method achieved the highest performance in terms of the mean absolute distance and the Hausdorff distance for the ACDC dataset, and the mean absolute distance and Dice score for the ultrasound dataset. An experiment was also performed to test the effect of the diffeomorphic constraints for the Jacobian determinant.

6.2 Limitations and future work

This section lists some of the limitations of the proposed work, and ways to remedy them and improve on the algorithms developed.

6.2.1 Manual interaction

One of the significant drawbacks of the proposed work is the amount of manual interaction necessary. For the 3D spatial segmentation for a single time point, the method requires the user to select two points to form an axis and to draw two contours on orthogonal slices. For the temporal extension of the algorithm, the user must draw an additional two contours for the end-systolic phase. In the future, machine learning

methods or deep learning approaches could be applied to choose the appropriate axis automatically and to delineate the contours necessary for the algorithm.

The 3D-to-3D registration algorithm relies on the delineation of the end-diastolic mesh and the end-systolic mesh to obtain the meshes for the other frames in the cardiac cycle. The use of both of the meshes improves the algorithm's performance, as with using only the end-diastolic mesh as input, it may be challenging to capture the motion at end-systole. Unfortunately, the requirement of meshes at both frames of the cardiac cycle is a large amount of manual input. For this, other machine learning or deep learning methods would be appropriate to use.

6.2.2 Clinical measures

One of the primary motivations of the proposed work was to compute metrics that would be helpful to clinicians for diagnosing a patient. The presented methods were thoroughly compared to the ground truth using distance metrics, which included the mean absolute distance, Hausdorff distance, and the Dice score. The end-diastolic volume, end-systolic volume, ejection fraction, and volume of each frame over the cardiac cycle were computed for the clinical measures. For several methods, Bland-Altman plots were also generated in order to determine the bias in the volumetric measurements compared to the ground truth.

Several global indices would be beneficial to calculate for clinicians. In particular, measurements including the global longitudinal strain and global circumferential strain are helpful, as they can aid in assessing the systolic function of the heart [0]. Other measures like the twist and torsion would help inform the clinician about issues such as diagnosing dilated cardiomyopathy [0]. In this condition, the twist mechanics of the LV are affected because the chamber is larger, increasing the sphericity of the chamber. The twist can also be affected because of cardiac interventions [0].

One of the significant advantages of performing 3D temporal segmentation of the left ventricle is the ability to obtain global functional measures and perform regional

motion analysis. Analysis of specific segments of the left ventricle in terms of strain is crucial in detecting abnormalities. Therefore it would have been beneficial to calculate longitudinal, circumferential, and radial strain measures, along with displacement and volume measurements for each region.

6.2.3 Creation of the ground truth

One point to be discussed is the generation of the ground truth for each of the three contributions. In Chapter 3, the CETUS dataset is used as the ground truth comparison for the end-diastolic and end-systolic frames. Three expert cardiologists developed a set of rules in order to achieve a high consistency, including rules for the wall of the LV, the mitral valve plane, and the inclusion of trabeculations and papillary muscles [79, 80]. Segmentations were then performed separately by each of the cardiologists, and the final reference mesh was agreed upon by the three cardiologists. Tables 3.1 and 3.2 display the inter-observer values among the three expert cardiologists, therefore creating a maximum accuracy possible for the proposed method and the other nine methods.

In Chapters 4 and 5, a single expert cardiologist used the TomTec Arena software to delineate the LV. The software relies on the user to align the LV along an axis, from which an estimate of the endocardial borders of the LV are provided at end-diastole and end-systole. The software then uses a speckle tracking approach to obtain the contours for all frames of the cardiac cycle. This approach may be biased as our proposed algorithm relies on clinical software for the ground truth. In the future, it would be better to obtain manual segmentations directly from the expert cardiologist without the use of additional tracking software.

The studies in Chapters 4 and 5 could be improved, as only a single expert cardiologist provided the ground truth. It would be useful to perform inter-observer and intra-observer studies by having both multiple observers over multiple time points to obtain the segmentation. Performing this type of analysis would allow us to establish

a baseline of the agreement between different raters. Algorithms such as STAPLE [0] could be used for the computation of an estimate of the true segmentation.

6.2.4 Comparison to other registration methods

Chapters 4 and 5 compared the proposed method to four and six other registration approaches, respectively. Parameters were chosen based on default values from example codes and published papers. Issues with the parameters are apparent in the volume curves for the ultrasound dataset, where the methods based on Dipy and the Demons approaches are significantly off, and vary greatly from the ground truth. In the future, it would be better to perform thorough experimentation and analysis of the parameters for each registration method.

6.2.5 Improvements to the 3D-to-3D registration algorithm

There several improvements and additions to the 3D-to-3D diffeomorphic registration algorithm that can be implemented. One area would be for the similarity metric, where apart from the current similarity metric (sum of squared differences), others such as mutual information or normalized cross-correlation could be implemented. In multi-modality registration, having the option to use different similarity metrics would be beneficial to the user.

One method that could be used to improve the performance of the registration algorithm is to apply a multi-resolution approach. The benefit of an image pyramid approach is that registration is applied to first obtain a coarse alignment, where the deformation fields are successively improved at each level of the image pyramid.

Noise in ultrasound images is a large factor that plays into the analysis of the data. The diffeomorphic registration algorithm may be affected by the image's noise; therefore, performing preprocessing and speckle reduction could prove helpful.

The proposed registration algorithm was applied in a sequence of images, where pairwise registration was performed sequentially across the frames. This method

of image registration is prone to error accumulation, and therefore both forward and reverse registration was completed, and a weighting applied. Other sequence registration methods can be explored that would reduce the error accumulation.

The proposed method for 3D-to-3D registration provides clinicians with a large amount of possible extensions. The algorithm could be applied to other chambers of the heart, where the dynamics are harder to model than that of the left ventricle. It would also be beneficial to validate the algorithm on a larger, more varied set of patients. This would include patients obtained from different ultrasound scanners and different hospitals. It would also be interesting to test this algorithm on patients that have significant abnormalities in the left ventricle, such as those with a previous heart attack, cardiomyopathy, and various congenital diseases.

Bibliography

[1] Rice University. (2021). "Anatomy and physiology open stax," [Online]. Available: https://openstax.org/books/anatomy-and-physiology/pages/19-1-heart-anatomy (visited on 2021).

[2] Texas Heart Institute. (2021). "Heart anatomy," [Online]. Available: https://www.texasheart.org/heart-health/heart-information-center/topics/heart-anatomy/ (visited on 2021).

[3] S Steinbaum. (2021). "Heart disease and electrocardiograms," [Online]. Available: https://www.webmd.com/heart-disease/electrocardiogram-ekgs (visited on 2021).

[4] OpenStax CNX. (2021). "Physiology of the heart," [Online]. Available: https://courses.lumenlearning.com/boundless-ap/chapter/physiology-of-the-heart/ (visited on 2021).

[5] S. Bierig and A Jones, "Accuracy and cost comparison of ultrasound versus alternative imaging modalities, including ct, mr, pet, and angiography," *Journal of Diagnostic Medical Sonography*, vol. 25, no. 3, pp. 138–44, 2009.

[6] V Mor-Avi, C Jenkins, H. Kühl, H. Nesser, T Marwick, A Franke, C Ebner, B. Freed, R Steringer-Mascherbauer, H Pollard, and L Weinert, "Real-time 3-dimensional echocardiographic quantification of left ventricular volumes: Multicenter study for validation with magnetic resonance imaging and investigation of sources of error," *JACC: Cardiovascular Imaging*, vol. 1, no. 4, pp. 413–423, 2008.

[7] 123sonography. (2021). "2.3.2 apical window," [Online]. Available: https://www.123sonography.com/ebook/apical-window (visited on 2021).

[8] R. Lang, V Mor-Avi, L Sugeng, P. Nieman, and D. Sahn, "Three-dimensional echocardiography: The benefits of the additional dimension," *Journal of the American College of Cardiology*, vol. 48, no. 10, pp. 2053–69, 2006.

[9] R. Lang, L. Badano, W Tsang, D. Adams, E Agricola, T Buck, F. Faletra, A Franke, J Hung, L. de Isla, and O Kamp, "EAE/ASE recommendations for image acquisition and display using three-dimensional echocardiography," *European Heart Journal-Cardiovascular Imaging*, vol. 13, no. 1, pp. 1–46, 2012.

[10] K. Leung and J. Bosch, "Automated border detection in three-dimensional echocardiography: Principles and promises," *European journal of echocardiography*, vol. 11, no. 2, pp. 97–108, 2010.

[11] T. Nelson, D. Pretorius, A Hull, M Riccabona, M. Sklansky, and G James, "Sources and impact of artifacts on clinical three-dimensional ultrasound imaging," *Ultrasound Obstet Gynecol*, vol. 16, no. 4, pp. 374–83, 2000.

[12] O. Michailovich and A Tannenbaum, "Despeckling of medical ultrasound images," *IEEE transactions on ultrasonics, ferroelectrics, and frequency control*, vol. 53, no. 1, pp. 64–78, 2006.

[13] T Lamb, K Punithakumar, A Hareendranathan, M Choy, B Pierre, N Michelle, and H Becher, "Multi-view 3D fusion echocardiography: Enhancing clinical feasibility with a novel respiratory tracking technique," *Canadian Journal of Cardiology*, vol. 34, no. 10, S197, 2018.

[14] ECG and Echo Learning. (2021). "Clinical echocardiography," [Online]. Available: https://ecgwaves.com/topic/stroke-volume-vti-velocity-time-integral-cardiac-output/ (visited on 2021).

[15] (2017). "TomTec Arena - 4D LV-Analysis," [Online]. Available: https://www.tomtec.de/products/application-finder/4d-lv-analysis/.

[16] Philips. (2021). "Cardiac 3d chamber quantifications driven by advanced automation," [Online]. Available: https://www.usa.philips.com/healthcare/resources/feature-detail/ultrasound-heartmodel (visited on 2021).

[17] D Muraru, A Niero, H Rodriguez-Zanella, D Cherata, and L Badano, "Three-dimensional speckle-tracking echocardiography: Benefits and limitations of integrating myocardial mechanics with three-dimensional imaging," *Cardiovascular diagnosis and therapy*, vol. 8, no. 1, pp. 101–118, 2018.

[18] K. Brock, S Mutic, T. McNutt, H Li, and M. Kessler, "Use of image registration and fusion algorithms and techniques in radiotherapy: Report of the AAPM radiation therapy committee task group no. 132," *Medical physics*, vol. 44, no. 7, e43–76, 2017.

[19] A Klein, S. Ghosh, B Avants, B. Yeo, B Fischl, B Ardekani, J. Gee, J. Mann, and R. Parsey, "Evaluation of volume-based and surface-based brain image registration methods," *Neuroimage*, vol. 51, no. 1, pp. 214–20, 2010.

[20] A Sotiras, C Davatzikos, and N Paragios, "Deformable medical image registration: A survey," *IEEE transactions on medical imaging*, vol. 32, no. 7, pp. 1153–90, 2013.

[21] A Khalil, S. Ng, Y. Liew, and K. Lai, "An overview on image registration techniques for cardiac diagnosis and treatment," *Cardiology research and practice*, pp. 1–15, 2018.

[22] A Elen, H. Choi, D Loeckx, H Gao, P Claus, P Suetens, F Maes, and J D'hooge, "Three-dimensional cardiac strain estimation using spatio–temporal elastic registration of ultrasound images: A feasibility study," *IEEE transactions on medical imaging*, vol. 27, no. 11, pp. 1580–91, 2008.

[23] A Lu, N Parajuli, M Zontak, J Stendahl, K Ta, Z Liu, N Boutagy, G. Jeng, I Alkhalil, L. Staib, and M O'Donnell, "Learning-based regularization for cardiac strain analysis with ability for domain adaptation," *arXiv preprint*, pp. 1–14, 2018.

[24] A Myronenko, X Song, and D. Sahn, "Maximum likelihood motion estimation in 3D echocardiography through non-rigid registration in spherical coordinates," *In International Conference on Functional Imaging and Modeling of the Heart*, pp. 427–436, 2009.

[25] B Heyde, D Barbosa, P Claus, F Maes, and J D'hooge, "Three-dimensional cardiac motion estimation based on non-rigid image registration using a novel transformation model adapted to the heart," *In International Workshop on Statistical Atlases and Computational Models of the Heart*, pp. 142–150, 2012.

[26] B Heyde, M Alessandrini, J Hermans, D Barbosa, P Claus, and J D'hooge, "Anatomical image registration using volume conservation to assess cardiac deformation from 3D ultrasound recordings," *IEEE transactions on medical imaging*, vol. 35, no. 2, pp. 501–11, 2015.

[27] M De Craene, G Piella, O Camara, N Duchateau, E Silva, A Doltra, J D'hooge, J Brugada, M Sitges, and A. Frangi, "Temporal diffeomorphic free-form deformation: Application to motion and strain estimation from 3D echocardiography," *Medical image analysis*, vol. 16, no. 2, pp. 427–50, 2012.

[28] G Piella, A. Porras, M De Craene, N Duchateau, and A. Frangi, "Temporal diffeomorphic free form deformation to quantify changes induced by left and right bundle branch block and pacing," *In International Workshop on Statistical Atlases and Computational Models of the Heart*, pp. 134–141, 2012.

[29] B Cohen, "New maximum likelihood motion estimation schemes for noisy ultrasound images," *Pattern Recognition*, vol. 35, no. 2, pp. 455–63, 2002.

[30] W Shi, M Jantsch, P Aljabar, L Pizarro, W Bai, H Wang, D O'Regan, X Zhuang, and D Rueckert, "Temporal sparse free-form deformations," *Medical image analysis*, vol. 17, no. 7, pp. 779–89, 2013.

[31] Z Zhang, M Ashraf, D. Sahn, and X Song, "Temporally diffeomorphic cardiac motion estimation from three-dimensional echocardiography by minimization of intensity consistency error," *Medical physics*, vol. 41, no. 5, p. 052 902, 2014.

[32] A Lu, M Zontak, N Parajuli, J. Stendahl, N Boutagy, M Eberle, M O'Donnell, A. Sinusas, and J. Duncan, "Dictionary learning-based spatiotemporal regularization for 3D dense speckle tracking," *In Medical Imaging 2017: Ultrasonic Imaging and Tomography*, vol. 10139, p. 1 013 904, 2017.

[33] M Bernier, P. Jodoin, and A Lalande, "Automatized evaluation of the left ventricular ejection fraction from echocardiographic images using graph cut," *Proceedings MICCAI Challenge on Echocardiographic Three-Dimensional Ultrasound Segmentation (CETUS), MIDAS Journal*, pp. 25–32, 2014.

[34] R Juang, E. McVeigh, B Hoffmann, D Yuh, and P Burlina, "Automatic segmentation of the left-ventricular cavity and atrium in 3D ultrasound using graph cuts and the radial symmetry transform," *In 2011 IEEE International Symposium on Biomedical Imaging: From Nano to Macros*, pp. 606–609, 2011.

[35] F Milletari, M Yigitsoy, N Navab, and S Ahmadi, "Left ventricle segmentation in cardiac ultrasound using hough-forests with implicit shape and appearance priors," *Proceedings MICCAI Challenge on Echocardiographic Three-Dimensional Ultrasound Segmentation (CETUS), MIDAS Journal*, pp. 49–56, 2014.

[36] K Keraudren, O Oktay, W Shi, J. Hajnal, and D Rueckert, "Endocardial 3D ultrasound segmentation using autocontext random forests," *Proceedings MICCAI Challenge on Echocardiographic Three-Dimensional Ultrasound Segmentation (CETUS), MIDAS Journal*, pp. 41–48, 2014.

[37] Z Tu, "Auto-context and its application to high-level vision tasks," *In 2008 IEEE Conference on Computer Vision and Pattern Recognition*, pp. 1–8, 2008.

[38] J Domingos, R Stebbing, and J Noble, "Endocardial segmentation using structured random forests in 3D echocardiography," *Proceedings MICCAI Challenge on Echocardiographic Three-Dimensional Ultrasound Segmentation (CETUS), MIDAS Journal*, pp. 33–40, 2014.

[39] K. Leung, M van Stralen, M. Voormolen, N de Jong, A. van der Steen, J. Reiber, and J. Bosch, "Improving 3D active appearance model segmentation of the left ventricle with jacobian tuning," *In Medical Imaging 2008: Image Processing*, vol. 6914, 69143B, 2008.

[40] T. Cootes and C. Taylor, "An algorithm for tuning an active appearance model to new data," *In BMVC*, pp. 919–928, 2006.

[41] M Van Stralen, A Haak, K. Leung, G Van Burken, and J Bosch, "Segmentation of multi-center 3D left ventricular echocardiograms by active appearance models," *Proceedings MICCAI Challenge on Echocardiographic Three-Dimensional Ultrasound Segmentation (CETUS), MIDAS Journal*, pp. 73–80, 2014.

[42] R. Stebbing and J. Noble, "Delineating anatomical boundaries using the boundary fragment model," *Medical image analysis*, vol. 17, no. 8, pp. 1123–1136, 2013.

[43] C Santiago, J. Marques, and J. Nascimento, "A robust deformable model for 3D segmentation of the left ventricle from ultrasound data," *In Mathematical methodologies in pattern recognition and machine learning 2013*, pp. 163–178, 2013.

[44] C Wang and Ö Smedby, "Model-based left ventricle segmentation in 3D ultrasound using phase image," *Proceedings MICCAI Challenge on Echocardiographic Three-Dimensional Ultrasound Segmentation (CETUS), MIDAS Journal*, 2014.

[45] E Smistad and F Lindseth, "Real-time tracking of the left ventricle in 3D ultrasound using Kalman filter and mean value coordinates," *Proceedings MICCAI Challenge on Echocardiographic Three-Dimensional Ultrasound Segmentation (CETUS), MIDAS Journal*, pp. 65–72, 2014.

[46] F Khellaf, S Leclerc, J. Voorneveld, R. Bandaru, J. Bosch, and O Bernard, "Left ventricle segmentation in 3D ultrasound by combining structured random forests with active shape models," *In Medical Imaging 2018: Image Processing*, vol. 10574, 105740J, 2018.

[47] D Barbosa, D Friboulet, J D'hooge, and O Bernard, "Fast tracking of the left ventricle using global anatomical affine optical flow and local recursive block matching," *Proceedings MICCAI Challenge on Echocardiographic Three-Dimensional Ultrasound Segmentation (CETUS), MIDAS Journal*, pp. 17–24, 2014.

[48] D Barbosa, T Dietenbeck, B Heyde, H Houle, D Friboulet, J D'hooge, and O Bernard, "Fast and fully automatic 3-d echocardiographic segmentation using b-spline explicit active surfaces: Feasibility study and validation in a clinical setting," *Ultrasound in medicine biology*, vol. 39, no. 1, pp. 89–101, 2013.

[49] D Barbosa, T Dietenbeck, J Schaerer, J D'hooge, D Friboulet, and O Bernard, "B-spline explicit active surfaces: An efficient framework for real-time 3D region-based segmentation," *IEEE Transactions on Image Processing*, vol. 21, no. 1, pp. 241–251, 2012.

[50] X Zhuang, C Yao, Y Ma, D Hawkes, G Penney, and S Ourselin, "Registration-based propagation for whole heart segmentation from compounded 3D echocardiography," *Biomedical Imaging: From Nano to Macro, 2010 IEEE International Symposium*, pp. 1093–1096, 2010.

[51] O Oktay, W Shi, K Keraudren, J Caballero, D Rueckert, and J. Hajnal, "Learning shape representations for multi-atlas endocardium segmentation in 3D echo images," *Proceedings MICCAI Challenge on Echocardiographic Three-Dimensional Ultrasound Segmentation (CETUS), MIDAS Journal*, pp. 57–64, 2014.

[52] O Oktay, A Gomez, K Keraudren, A Schuh, W Bai, W Shi, G Penney, and D Rueckert, "Probabilistic edge map (PEM) for 3D ultrasound image registration and multi-atlas left ventricle segmentation," *In International Conference on Functional Imaging and Modeling of the Heart*, pp. 223–230, 2015.

[53] X Zhuang, K Rhode, S Arridge, R Razavi, D Hill, D Hawkes, and S Ourselin, "An atlas-based segmentation propagation framework using locally affine registration-application to automatic whole heart segmentation," *Medical Image Computing and Computer-Assisted Intervention-MICCAI 2008*, pp. 425–433, 2008.

[54] O Oktay, E Ferrante, K Kamnitsas, M Heinrich, W Bai, J Caballero, S. Cook, A De Marvao, T Dawes, D. O'Regan, and B Kainz, "Anatomically constrained neural networks (ACNNs): Application to cardiac image enhancement and segmentation," *IEEE transactions on medical imaging*, vol. 37, no. 2, pp. 384–95, 2017.

[55] S Dong, G Luo, G Sun, K Wang, and H Zhang, "A left ventricular segmentation method on 3D echocardiography using deep learning and snake," *In 2016 Computing in Cardiology Conference (CinC)*, pp. 473–476, 2016.

[56] S Dong, G Luo, K Wang, S Cao, Q Li, and H Zhang, "A combined fully convolutional networks and deformable model for automatic left ventricle segmentation based on 3D echocardiography," *BioMed research international*, pp. 1–16, 2018.

[57] S Dong, G Luo, K Wang, S Cao, A Mercado, O Shmuilovich, H Zhang, and S Li, "VoxelAtlasGAN: 3D left ventricle segmentation on echocardiography with atlas guided generation and voxel-to-voxel discrimination," *In International Conference on Medical Image Computing and Computer-Assisted Intervention*, pp. 622–629, 2018.

[58] S Dong, G Luo, C Tam, W Wang, K Wang, S Cao, B Chen, H Zhang, and S Li, "Deep atlas network for efficient 3D left ventricle segmentation on echocardiography," *Medical image analysis*, vol. 61, no. 1, p. 101 638, 2020.

[59] F Orderud, "A framework for real-time left ventricular tracking in 3D+ t, echocardiography, using nonlinear deformable contours and Kalman filter based tracking," *Computers in Cardiology, IEEE*, pp. 125–128, 2006.

[60] F Orderud and S. Rabben, "Real-time 3D segmentation of the left ventricle using deformable subdivision surfaces," *Computer Vision and Pattern Recognition, 2008, IEEE Conference*, pp. 1–8, 2008.

[61] D Doo and M Sabin, "Behaviour of recursive division surfaces near extraordinary points," *Computer-Aided Design*, vol. 10, no. 6, pp. 356–60, 1978.

[62] F Orderud, J Hansgård, and S. Rabben, "Real-time tracking of the left ventricle in 3D echocardiography using a state estimation approach," *n International Conference on Medical Image Computing and Computer-Assisted Intervention*, pp. 858–865, 2007.

[63] K. Leung, M. Danilouchkine, M van Stralen, N de Jong, A. van der Steen, and J. Bosch, "Left ventricular border tracking using cardiac motion models and optical flow," *Ultrasound in medicine and biology*, vol. 37, no. 4, pp. 605–16, 2011.

[64] S Queirós, J. Vilaça, P Morais, J. Fonseca, J D'hooge, and D Barbosa, "Fast left ventricle tracking using localized anatomical affine optical flow," *International journal for numerical methods in biomedical engineering*, vol. 33, no. 11, e2871, 2017.

[65] D Barbosa, B Heyde, T Dietenbeck, D Friboulet, J D'hooge, and O Bernard, "Fast left ventricle tracking in 3D echocardiographic data using anatomical affine optical flow," *In International Conference on Functional Imaging and Modeling of the Heart*, pp. 191–199, 2013.

[66] E Dikici and F Orderud, "Graph-cut based edge detection for Kalman filter based left ventricle tracking in 3d+ t echocardiography," *Computing in Cardiology, IEEE*, pp. 205–208, 2010.

[67] J Hansegård, F Orderud, and S. Rabben, "Real-time active shape models for segmentation of 3D cardiac ultrasound," *In International Conference on Computer Analysis of Images and Patterns*, pp. 157–164, 2007.

[68] D Barbosa, J Pedrosa, B Heyde, T Dietenbeck, D Friboulet, O Bernard, and J D'hooge, "heartBEATS: A hybrid energy approach for real-time B-spline explicit active tracking of surfaces," *Computerized Medical Imaging and Graphics*, pp. 26–33, 2017.

[69] M van Stralen, A Haak, K. Leung, G van Burken, C Bos, and J. Bosch, "Full-cycle left ventricular segmentation and tracking in 3D echocardiography using active appearance models," *IEEE International Ultrasonics Symposium (IUS)*, pp. 1–4, 2015.

[70] X Huang, B. Lin, C. Compas, A. Sinusas, L. Staib, and J. Duncan, "Segmentation of left ventricles from echocardiographic sequences via sparse appearance representation," *IEEE Workshop on Mathematical Methods in Biomedical Image Analysis*, pp. 305–312, 2012.

[71] X Huang, D. Dione, C. Compas, X Papademetris, B. Lin, A. Sinusas, and J. Duncan, "A dynamical appearance model based on multiscale sparse representation: Segmentation of the left ventricle from 4D echocardiography," *In International Conference on Medical Image Computing and Computer-Assisted Intervention*, pp. 58–65, 2012.

[72] X Huang, D. Dione, C. Compas, X Papademetris, B. Lin, A Bregasi, A. Sinusas, L. Staib, and J. Duncan, "Contour tracking in echocardiographic sequences via sparse representation and dictionary learning," *Medical image analysis*, pp. 253–71, 2014.

[73] K Ta, S. Ahn, J. Stendahl, A. Sinusas, and J. Duncan, "A semi-supervised joint network for simultaneous left ventricular motion tracking and segmentation in 4D echocardiography," *In International Conference on Medical Image Computing and Computer-Assisted Intervention*, pp. 468–477, 2020.

[74] G Balakrishnan, A Zhao, M. Sabuncu, J Guttag, and A. Dalca, "An unsupervised learning model for deformable medical image registration," *In Proceedings of the IEEE conference on computer vision and pattern recognition*, pp. 9252–9260, 2018.

[75] Çiçek, A Abdulkadir, S. Lienkamp, T Brox, and O Ronneberger, "3D U-Net: Learning dense volumetric segmentation from sparse annotation," *In International conference on medical image computing and computer-assisted intervention*, pp. 424–432, 2016.

[76] K Punithakumar, P Boulanger, and M Noga, "A GPU-accelerated deformable image registration algorithm with applications to right ventricular segmentation," *IEEE Access*, vol. 5, pp. 20 374–20 382, 2017.

[77] B Delaunay, "Sur la sphere vide," *Nauk SSSR, Otdelenie Matematicheskii i Estestvennyka Nauk*, vol. 7, pp. 793–800, 1934.

[78] H Edelsbrunner, D Kirkpatrick, and R Seidel, "On the shape of a set of points in the plane," *IEEE Transactions on information theory*, vol. 29, no. 4, pp. 551–559, 1983.

[79] A Papachristidis, M Geleijnse, E Galli, B Heyde, M Alessandrini, D Barbosa, E Donal, M Monaghan, O Bernard, J D'hooge, and J Bosch, "Clinical expert delineation of 3D left ventricular echocardiograms for the CETUS segmentation challenge," 2014.

[80] O Bernard, J. Bosch, B Heyde, M Alessandrini, D Barbosa, S Camarasu-Pop, F Cervenansky, S Valette, O Mirea, M Bernier, and P. Jodoin, "Standardized evaluation system for left ventricular segmentation algorithms in 3D echocardiography," *IEEE Transactions on medical imaging*, vol. 35, no. 4, pp. 967–977, 2016.

[81] S Gottschalk, M. Lin, and D Manocha, "Obbtree: A hierarchical structure for rapid interference detection," *Proceedings of the 23rd annual conference on Computer graphics and interactive techniques. ACM*, pp. 171–180, 1996.

[82] D. Huttenlocher, G. Klanderman, and W. Rucklidge, "Comparing images using the Hausdorff distance," *IEEE Transactions on pattern analysis and machine intelligence*, vol. 15, no. 9, pp. 850–863, 1993.

[83] L. Dice, "Measures of the amount of ecologic association between species," *Ecology*, vol. 26, no. 3, pp. 297–302, 1945.

[84] D. Altman and J. Bland, "Measurement in medicine: The analysis of method comparison studies," *Journal of the Royal Statistical Society: Series D (The Statistician)*, vol. 32, no. 3, pp. 307–17, 1983.

[85] T. Yoo, M. Ackerman, W. Lorensen, W Schroeder, V Chalana, S Aylward, D Metaxas, and R Whitaker, "Engineering and algorithm design for an image processing api: A technical report on ITK - the insight toolkit," *Studies in health technology and informatics*, pp. 586–92, 2002.

[86] C Zach, T Pock, and H Bischof, "A duality based approach for realtime TV-L1 optical flow," *Joint pattern recognition symposium*, pp. 214–223, 2007.

[87] A Wedel, T Pock, C Zach, H Bischof, and D Cremers, "An improved algorithm for TV-L1 optical flow," *In Statistical and geometrical approaches to visual motion analysis*, pp. 23–45, 2009.

[88] J. Pérez, E Meinhardt-Llopis, and G Facciolo, "TV-L1 optical flow estimation," *Image Processing On Line*, pp. 137–50, 2013.

[89] S Van der Walt, J. Schönberger, J Nunez-Iglesias, F Boulogne, J. Warner, N Yager, E Gouillart, and T Yu, "Scikit-image: Image processing in python," *PeerJ*, vol. 2, e453, 2014.

[90] G Bradski and A Kaehler, *Learning OpenCV: Computer vision with the OpenCV library*. O'Reilly Media, Inc., 2008.

[91] G Farnebäck, "Two-frame motion estimation based on polynomial expansion," *Scandinavian conference on Image analysis*, pp. 363–370, 2003.

[92] J. Thirion, "Image matching as a diffusion process: An analogy with Maxwell's demons," *Medical image analysis*, vol. 2, no. 3, pp. 243–60, 1998.

[93] J Shackleford, N Kandasamy, and G Sharp, *High Performance Deformable Image Registration Algorithms for Many core Processors*. Elsevier, 2014.

[94] J. Liu, "New developments of the deformation method," Ph.D. dissertation, The University of Texas at Arlington, 2006.

[95] A. Goshtasby, *Image registration: Principles, tools and methods*. Springer Science Business Media, 2012.

[96] D. Cheng, *Field and wave electromagnetics*. Pearson Education India, 1989.

[97] Khan Academy. (2021). "Divergence," [Online]. Available: https://www.khanacademy.org/math/multivariable-calculus/multivariable-derivatives/divergence-and-curl-articles/a/divergence (visited on 2021).

[98] Khan Academy. (2021). "Curl, fluid rotation in three dimensions," [Online]. Available: hhttps://www.khanacademy.org/math/multivariable-calculus/multivariable-derivatives/divergence-and-curl-articles/a/curl (visited on 2021).

[99] J. Demmel. (2021). "Solving the discrete poisson equation using jacobi, sor, conjugate gradients, and the fft," [Online]. Available: https://people.eecs.berkeley.edu/~demmel/cs267/lecture24/lecture24.html (visited on 1996).

[100] O Bernard, A Lalande, C Zotti, F Cervenansky, X Yang, P. Heng, I Cetin, K Lekadir, O Camara, M. Ballester, and G Sanroma, "Deep learning techniques for automatic MRI cardiac multi-structures segmentation and diagnosis: Is the problem solved?" *IEEE transactions on medical imaging*, vol. 37, no. 11, pp. 2514–25, 2018.

[101] B. Avants, C. Epstein, M Grossman, and J. Gee, "Symmetric diffeomorphic image registration with cross-correlation: Evaluating automated labeling of elderly and neurodegenerative brain," *Medical image analysis*, vol. 12, no. 1, pp. 26–41, 2008.

[102] C Zachiu, B. de Senneville, C Moonen, and M Ries, "A framework for the correction of slow physiological drifts during MR-guided HIFU therapies: Proof of concept," *Medical physics*, vol. 42, no. 7, pp. 4137–48, 2015.

[103] C Zachiu, N Papadakis, M Ries, C Moonen, and B. de Senneville, "An improved optical flow tracking technique for real-time MR-guided beam therapies in moving organs," *Physics in Medicine and Biology*, vol. 60, no. 23, pp. 9003–29, 2015.

[104] D. Shamonin, E. Bron, B. Lelieveldt, M Smits, S Klein, and M Staring, "Fast parallel image registration on CPU and GPU for diagnostic classification of Alzheimer's disease," *Frontiers in neuroinformatics*, vol. 7, no. 50, pp. 1–15, 2014.

[105] B. Avants, P. Schoenemann, and J. Gee, "Landmark and intensity-driven lagrangian frame diffeomorphic image registration: Application to structurally and functionally based inter-species comparison," *Medical image analysis*, vol. 10, pp. 397–412, 2006.

[106] B. Horn and B. Schunck, "Determining optical flow," *In Techniques and Applications of Image Understanding*, vol. 281, pp. 319–331, 1981.

[107] D Mattes, D. Haynor, H Vesselle, T. Lewellyn, and W Eubank, "Nonrigid multimodality image registration," *Medical Imaging 2001: Image Processing - International Society for Optics and Photonics*, vol. 4322, pp. 1609–1620, 2001.

[0] Government of Canada. (2017). "Heart disease in canada," [Online]. Available: https://www.canada.ca/en/public-health/services/publications/diseases-conditions/heart-disease-canada.html (visited on 2021).

[0] S Karlsen, T Dahlslett, B Grenne, B Sjøli, O Smiseth, T Edvardsen, and H Brunvand, "Global longitudinal strain is a more reproducible measure of left ventricular function than ejection fraction regardless of echocardiographic training," *Cardiovascular ultrasound*, vol. 17, no. 1, pp. 1–2, 2019.

[0] A. Omar, S Vallabhajosyula, and P. Sengupta, "Left ventricular twist and torsion: Research observations and clinical applications," *Circulation: Cardiovascular Imaging*, vol. 8, no. 6, e003029, 2015.

[0] S. Warfield, K. Zou, and W. Wells, "Simultaneous truth and performance level estimation (staple): An algorithm for the validation of image segmentation," *IEEE transactions on medical imaging*, vol. 23, no. 7, pp. 903–21, 2004.